Naphtho[1,2-c:5,6-c']bis([1,2,3]thiadiazole) Enables an Efficient Halogen-Free Polymer Donor and Realizes Organic Solar Cells with Efficiency over 19%

Tao Jia,[a,b,†] Yongmin Luo,[c,†] Yulong Hai,[c,†] Tao Lin,[a] Xudong Qin,[d] Ruijie Ma,[e,*] Kezhou Fan,[f] Aleksandr A. Sergeev,[f] Top Archie Dela Peña,[c,g] Yao Li,[c] Mingjie Li,[g] Kam Sing Wong,[f] Gang Li,[e] Jiaying Wu,[c,*] Shengjian Liu,[b,*] and Fei Huang[d]

[a]School of Optoelectronic Engineering, Guangdong Polytechnic Normal University, Guangzhou, 510665, China

[b]School of Chemistry, Guangzhou Key Laboratory of Materials for Energy Conversion and Storage, Key Laboratory of Electronic Chemicals for Integrated Circuit Packaging, South China Normal University (SCNU), Guangzhou 510006, China

[c]Advanced Materials Thrust, Function Hub, The Hong Kong University of Science and Technology, Nansha 511400, Guangzhou, China

[d]Institute of Polymer Optoelectronic Materials and Devices, State Key Laboratory of Luminescent Materials and Devices, South China University of Technology, Guangzhou 510640, China

[e]Department of Electrical and Electronic Engineering, Research Institute for Smart Energy (RISE), Photonic Research Institute (PRI), The Hong Kong Polytechnic University, Hong Kong, China

[f]Department of Physics, School of Science, Hong Kong University of Science and Technology, Clear Water Bay, Kowloon, Hong Kong 999077, P.R. China

[g]Department of Applied Physics, Faculty of Science, The Hong Kong Polytechnic University, Kowloon, Hong Kong 999077, P.R. China

[†]These authors contributed equally.

*Corresponding author

E-mail: ruijie.ma@polyu.edu.hk (R. Ma); jiayingwu@ust.hk (J. Wu); shengjian.liu@m.scnu.edu.cn (S. Liu)

Content

1. General Experimental Details

1.1 Materials

2,6-Dibromonaphthalene (**compound 1**), naphtho[1,2-c:5,6-c']bis([1,2,5]thiadiazole) (**compound 7**), was purchased from Bide Pharmatech Ltd. Compound tributyl(4-(2-butyloctyl)thiophen-2-yl)stannane, tributyl(4-hexylthiophen-2-yl)stannane, (4,8-bis(5-(2-ethylhexyl)thiophen-2-yl)benzo[1,2-b:4,5-b']dithiophene-2,6-diyl)bis(trimethylstannane) (**BDT-DSn**), PNDI-F₃N, and BTP-eC9 were purchased from Solarmer Energy, Inc. Compound 4,7-bis(5-bromo-4-(2-ethylbutyl)thiophen-2-yl)benzo[d][1,2,3]thiadiazole (**BrThiBT**) and PiBT (M_n = 50.0kDa , M_w = 118.8 kDa) were synthesized as the reported literature.[1] Other chemicals and solvents were purchased from commercial sources (Sigma Aldrich, Acros, Strem, or Alfa Aesar) and used as received.

1.2 Synthetic Procedures

Syntheses of PiBT:
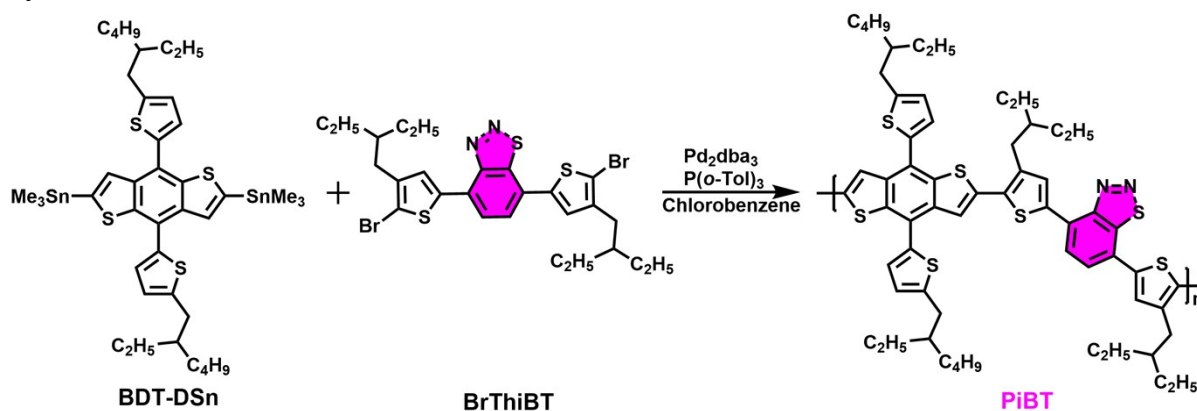
Scheme S1. Synthetic route of polymer PiBT.

Syntheses of Monomers for PiNT and PNT:

Scheme S2. Synthetic routes of monomer **M1**.

2,6-Dibromo-1,5-dinitronaphthalene (compound 2): Compound 1 (28.60g, 0.1mol) was added into a flask containing fuming nitric acid (200 mL) under ice bath. The mixture was stirred for 24 h at room temperature. Then, the reaction mixture was added into ice water and the precipitate was filtrated, washed with water and dichloromethane (DCM). **Compound 2** was obtained as light yellow solid (33.09 g, yield 88%). ^{1}H NMR (600 MHz, CDCl$_3$) δ 7.87 (d, J = 9.1 Hz, 2H), 7.68 (d, J = 9.1 Hz, 2H).
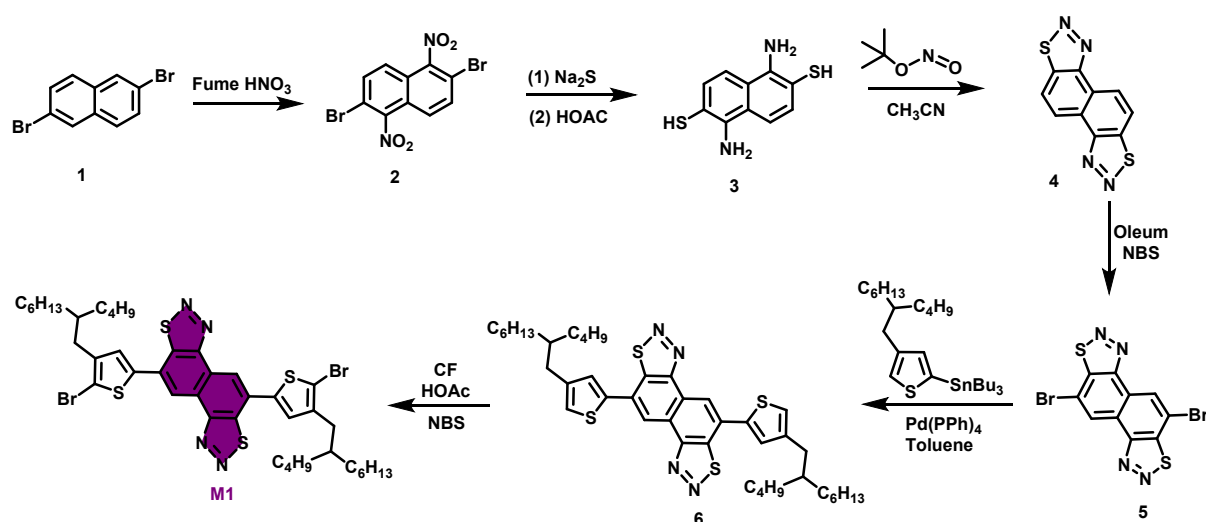
Naphtho[1,2-d:5,6-d']bis([1,2,3]thiadiazole) (compound 4): Compound 2 (15.04 g, 40 mmol) and sodium sulfide nonahydrate (240.2g, 1 mol) were added into a flask containing water (800 mL). The reaction was refluxed for 20 hours at air atmosphere. Then the reaction mixture was cooled to 50 °C and filtrated. The filter cake was washed with 200 mL water. The collected filtrate was neutralized with excess acetic acid and abundant precipitate was produced. The precipitate (**compound 3**) was filtrated quickly, washed with 500 mL water and immediately used for next step reaction. C**ompound 3** was added into a 500 mL flask containing acetonitrile (350 mL) at ice bath. Then the tert-butyl nitrite (15 mL) was added into the mixture dropwise. The reaction mixture was stirred at room temperature for another 1 hours and poured into methanol, the precipitate was collected to afford **compound 4** as white solid (6.70g, yield 69% for two step reactions). ^{1}H NMR (600 MHz, CDCl$_3$) δ 9.46 (d, J = 8.6 Hz, 2H), 8.46 (d, J = 8.6 Hz, 2H). ^{13}C NMR (151 MHz, CDCl$_3$) δ 154.72, 142.92, 142.56, 140.86, 139.63, 137.77, 129.84, 128.84, 126.84, 126.45, 124.90, 124.35, 113.54, 111.18, 40.02, 40.00,

33.97, 33.92, 32.54, 32.51, 28.84, 28.80, 25.72, 23.11, 14.18, 10.88. MS (m/z): calcd. for $C_{10}H_4N_4S_2$, 244.2900; found, 244.9947.

5,10-Dibromonaphtho[1,2-d:5,6-d']bis([1,2,3]thiadiazole) (compound 5): To a solution mixture of **compound 4** (2.44g, 10mmol) in oleum (20%) (30 mL), NBS (5.34 g, 30 mol) was added in three portion under ice bath. The mixture was then stirred at 50 °C for 3 hours. After cooled to room temperature, the resulting mixture was added into ice water and filtrated. The filter cake was washed with water and methanol and **compound 5** was collected as gray solid. **Compound 5** was hard for purification due to its poor solubility and thus immediately used for the next step reaction.

5,10-Bis(4-(2-butyloctyl)thiophen-2-yl)naphtho[1,2-d:5,6-d']bis([1,2,3]thiadiazole (compound 6)

Compound 5 (2.01g, 5 mmol) and tributyl(4-(2-butyloctyl)thiophen-2-yl)stannane (6.76g, 12.5 mmol) was added to 30 mL of toluene in a flask. The reaction mixture was purged with argon for 15 minutes. Then, the catalyst Pd(PPh$_3$)$_4$ (289 mg) was added and the solution was purged with argon for an additional 15 minutes. The reaction mixture was stirred at 120 °C for 24 hours. The organic solvent of reaction mixture was removed by vacuum evaporation and the residue was purified by column chromatography on silica gel using PE:DCM (3:1, *v/v*) as eluent to afford **compound 6** as light yellow solid (2.35 g, yield 63%). ^{1}H NMR (600 MHz, CDCl$_3$) δ 9.57 (s, 2H), 7.57 (d, *J* = 1.1 Hz, 2H), 7.14 (s, 2H), 2.68 (m, 4H), 1.38−1.32 (m, 20H), 1.29 (m, 12H), 0.92 (t, *J* = 7.0 Hz, 6H), 0.88 (t, *J* = 6.8 Hz, 6H). ^{13}C NMR (151 MHz, CDCl$_3$) δ 154.87, 143.87, 140.88, 140.61, 128.37, 127.11, 125.65, 123.21, 121.88, 38.99, 35.13, 33.41, 33.08, 31.95, 29.75, 29.71, 28.93, 26.67, 23.12, 22.71, 14.21, 14.14. MS (m/z): calcd. for $C_{42}H_{56}N_4S_4$, 745.1780; found, 745.3460.

5,10-Bis(5-bromo-4-(2-butyloctyl)thiophen-2-yl)naphtho[1,2-d:5,6-d']bis([1,2,3]thiadiazole) (M1)

To a solution mixture of **compound 6** (745 mg, 1 mmol) in 30 mL chloroform (CF) and 0.5mL acetic acid, NBS (427 mg, 2.4 mmol) was added in three portions in dark under air atmosphere.

The reaction mixture was then stirred at room temperature for 4 hour. After adding deionized water to the flask, the reaction mixture was extracted by DCM. The collected organic layer was removed by reduced pressure and the residue was purified by column chromatography on silica gel using PE:DCM (3:1, *v/v*) as eluent to afford **M1** as light yellow solid (795 mg, yield 88%). ^{1}H NMR (600 MHz, CDCl$_3$) δ 9.46 (s, 2H), 7.41 (s, 2H), 2.63 (d, *J* = 7.2 Hz, 4H), 1.86 – 1.72 (m, 2H), 1.40 – 1.33 (m, 20H), 1.32 – 1.30 (m, 12H), 0.92 (t, *J* = 7.0 Hz, 6H), 0.88 (t, *J* = 6.8 Hz, 6H). ^{13}C NMR (151 MHz, CDCl$_3$) δ 154.91, 143.36, 140.47, 140.34, 128.03, 126.47, 125.76, 121.87, 112.54, 38.69, 34.45, 33.44, 33.14, 31.93, 29.74, 28.84, 26.59, 23.13, 22.71, 14.19, 14.14. MS (m/z): calcd. for C$_{42}$H$_{54}$Br$_2$N$_4$S$_4$, 902.9700; found, 903.1653.
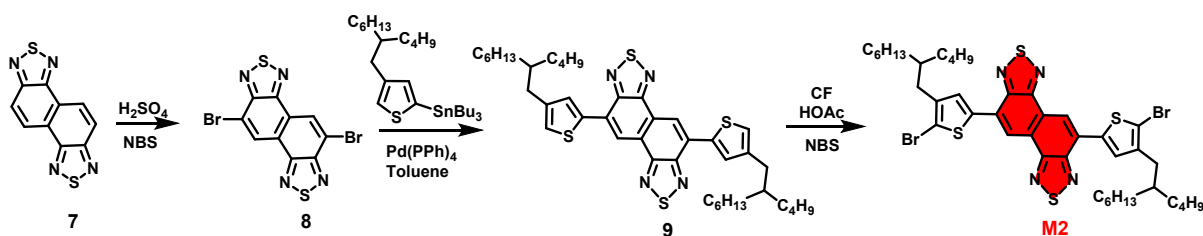
Scheme S3. Synthetic routes of monomer **M2**.

5,10-Bibromonaphtho[1,2-c:5,6-c']bis([1,2,5]thiadiazole) (compound 8)

To a solution mixture of naphtho[1,2-c:5,6-c']bis([1,2,5]thiadiazole) (**compound 7**) (2.44g, 10mmol) in oil of vitriol (50 mL), NBS (5.34 g, 30 mol) was added in three portion under air atmosphere. The mixture was then stirred at 80 ^{o}C for 24 hours. After cooled to room temperature, the resulting mixture was added into ice water and filtrated. The filter cake was washed with water and methanol and collected as yellow solid (compound **8**). Compound **8** was immediately used for the next step reaction due to its poor solubility for purification.

5,10-Bis(4-(2-butyloctyl)thiophen-2-yl)naphtho[1,2-c:5,6-c']bis([1,2,5]thiadiazole) (compound 9)

Compound 8 (2.01g, 5 mmol) and tributyl(4-(2-butyloctyl)thiophen-2-yl)stannane (6.76g, 12.5 mmol) was added to 50 mL of dry DMF in a flask. The reaction mixture was purged with argon for 15 minutes. Then, the catalyst Pd(PPh$_3$)$_4$ (289 mg, 5%) was added and the solution was purged with argon for an additional 15 minutes. The reaction mixture was heated to 120 ^{o}C with stirring for 24 hours. Then the reaction mixture was cooled to ambient temperature and poured into methanol to precipitate the crude product. After filtration, the residue was then

purified by chromatography using PE:(DCM as the eluent to obtain **compound 9** as a red solid (1.68 g, 45% yield). ^{1}H NMR (500 MHz, CDCl$_3$) δ 8.77 (s, 2H), 8.02 (d, J = 0.6 Hz, 2H), 7.07 (s, 2H), 2.65 (d, J = 6.9 Hz, 4H), 1.74 (m, 2H), 1.35 (m, 20H), 1.30 (m, 12H), 0.93 (t, J = 6.8 Hz, 6H), 0.88 (t, J = 6.6 Hz, 6H). ^{13}C NMR (126 MHz, CDCl$_3$) δ 153.18, 152.15, 143.07, 138.29, 130.24, 126.39, 124.39, 123.38, 121.78, 38.92, 35.09, 33.32, 33.01, 31.97, 29.80, 29.70, 28.87, 26.61, 23.15, 22.74, 14.25, 14.17. MS (m/z): calcd. for C$_{42}$H$_{56}$N$_4$S$_4$, 745.1780; found, 745.3462.

5,10-Bis(5-bromo-4-(2-butyloctyl)thiophen-2-yl)naphtho[1,2-c:5,6-c']bis([1,2,5]thiadiazole) (M2): To a solution mixture of **compound 9** (745 mg, 1mmol) in 30 mL chloroform (CF) and 0.5mL acetic acid, NBS (427 mg, 2.4 mmol) was added in three portions in dark under air atmosphere. The mixture was then stirred at room temperature for 2 hour. After adding deionized water to the flask, the reaction mixture was extracted by DCM. The collected organic layer was removed by reduced pressure and the residue was purified by column chromatography on silica gel using PE:DCM (2:1, v/v) as eluent to afford **M2** as purple solid (768 mg, yield 85%). ^{1}H NMR (500 MHz, CDCl$_3$) δ 8.17 (s, 2H), 7.58 (s, 2H), 2.50 (d, J = 7.2 Hz, 4H), 1.76 (m, 2H), 1.34 (m, 32H), 0.94 (t, J = 6.6 Hz, 6H), 0.89 (t, J = 6.7 Hz, 6H). ^{13}C NMR (126 MHz, CDCl$_3$) δ 152.39, 151.16, 142.15, 137.51, 129.07, 124.89, 123.70, 120.28, 113.32, 38.59, 34.21, 33.31, 33.00, 31.99, 29.85, 28.76, 26.52, 23.21, 22.77, 14.28, 14.21. MS (m/z): calcd. for C$_{42}$H$_{54}$Br$_2$N$_4$S$_4$, 902.9700; found, 903.1658.

**Syntheses of PiNT and PNT Polymers**
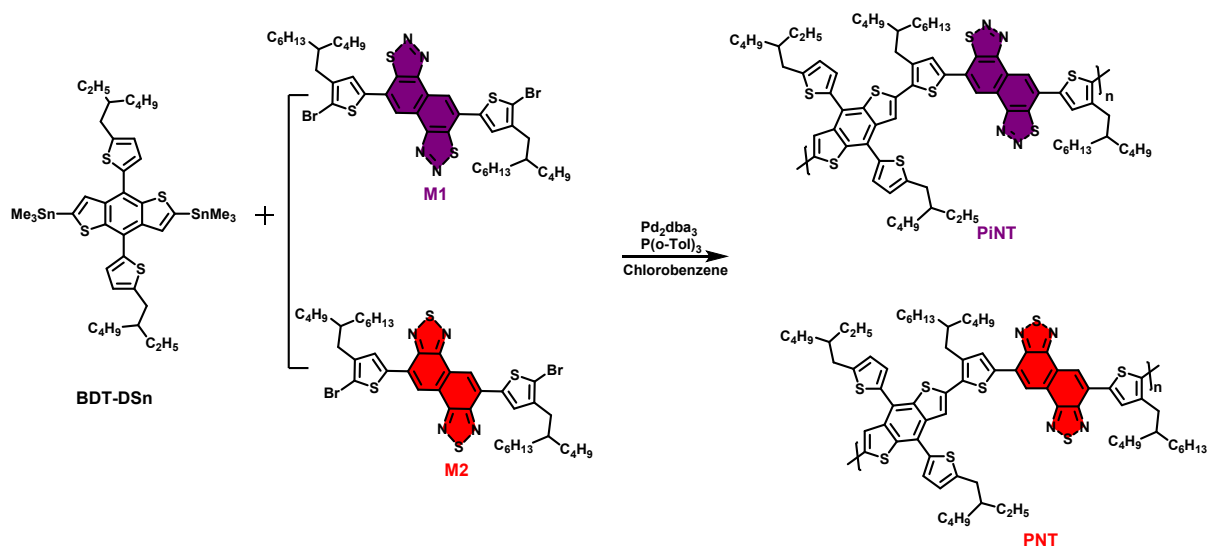
Scheme S4. Synthetic routes of polymers **PiNT** and **PNT**.

PiNT: Monomer **M1** (135.5 mg, 0.15 mmol), **BDT-DSn** (135.7 mg, 0.15 mmol), $Pd_2(dba)_3$ (3mg) and $P(o\text{-tol})_3$ (4.5 mg) were combined in a 15 mL sealed tube. Dry chlorobenzene (CB) (8 mL) was added under argon atmosphere. The mixture was reacted at 110 °C for 72 h. After cooled down to room temperature, the reactant mixture was poured into MeOH (300 mL). The precipitate was filtered and Soxhlet extracted with methanol, hexane, dichloromethane and chloroform. The ingredient extracted from chloroform was concentrated and precipitated into 500 mL methanol, filtered and dried under vacuum to give the black filament (171mg, yield 86 %, M_n = 55.2 kDa, M_w = 107.9 kDa); ^{1}H NMR (500 MHz, $C_2D_2Cl_4$,135 °C) δ 9.64 (s, 2H), 7.86 (s, 2H), 7.65 (s, 2H), 7.45 (d, J = 3.2 Hz, 2H), 7.01 (d, J = 3.0 Hz, 2H), 2.98 (d, J = 6.3 Hz, 8H), 1.98 – 1.89 (m, 2H), 1.81 (dt, J = 12.3, 6.1 Hz, 2H), 1.51 – 1.28 (m, 48H), 1.04 (t, J = 7.4 Hz, 6H), 0.97 (t, J = 6.9 Hz, 6H), 0.93 (t, J = 6.8 Hz, 6H), 0.87 (t, J = 6.9 Hz, 6H).

PNT: Monomer **M2** (135.5 mg, 0.15 mmol), **BDT-DSn** (135.7 mg, 0.15 mmol) $Pd_2(dba)_3$ (3mg) and $P(o\text{-tol})_3$ (4.5 mg) were combined in a 15 mL sealed tube. Dry chlorobenzene (CB) (8 mL) was added under argon atmosphere. The mixture was reacted at 110 °C for 72 h. After cooled down to room temperature, the reactant mixture was poured into MeOH (300 mL). The precipitate was filtered and Soxhlet extracted with methanol, hexane, dichloromethane and chloroform. The ingredient extracted from chloroform was concentrated and precipitated into 500 mL methanol, filtered and dried under vacuum to give the dark fiber (163mg, yield 82 %, M_n = 43.0 kDa, M_w = 93.6 kDa); ^{1}H NMR (500 MHz, $C_2D_2Cl_4$,135 °C) δ 9.14 (s, 2H), 8.23 (s,

2H), 7.84 (s, 2H), 7.45 (d, $J = 3.2$ Hz, 2H), 7.00 (d, $J = 2.8$ Hz, 2H), 2.98 (d, $J = 6.3$ Hz, 8H), 2.00 – 1.92 (m, 2H), 1.81 (dd, $J = 12.1$, 6.0 Hz, 2H), 1.54 – 1.28 (m, 48H), 1.05 (t, $J = 7.4$ Hz, 6H), 0.98 (t, $J = 6.8$ Hz, 6H), 0.92 (t, $J = 6.7$ Hz, 6H), 0.87 (d, $J = 6.9$ Hz, 6H).

Syntheses of model compounds DTiNT and DTNT
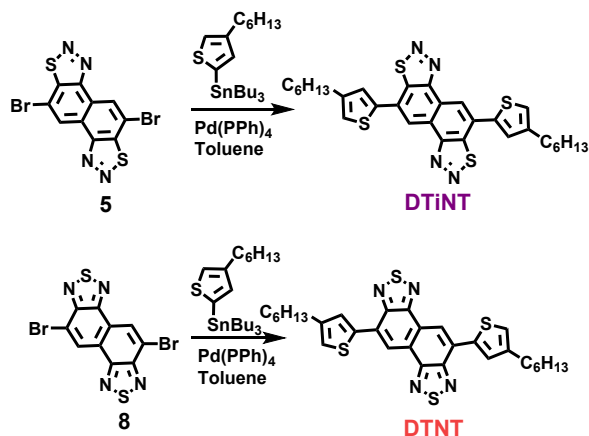
Scheme S5. The syntheses of **DTiNT and DTNT**.

DTiNT: **Compound 5** (201 mg, 0.5 mmol) and tributyl-(4-hexyl-2-thienyl)-stannane (685 mg, 1.5 mmol) was added to 20 mL of toluene in a flask. The reaction mixture was purged with argon for 15 minutes. Then, the catalyst Pd(PPh$_3$)$_4$ (30 mg) was added and the solution was purged with argon for an additional 15 minutes. The reaction mixture was stirred at 120 °C for 24 hours. The organic solvent of reaction mixture was removed by vacuum evaporation and the residue was purified by column chromatography on silica gel using PE:DCM (3:1, v/v) as eluent to afford **DTiNT** as yellow solid (237 mg, 82% yield). ^{1}H NMR (600 MHz, CDCl$_3$) δ 9.34 (s, 2H), 7.49 (s, 2H), 7.13 (s, 2H), 2.72 (t, $J = 7.7$ Hz, 4H), 1.77 – 1.70 (m, 4H), 1.48 – 1.41 (m, 4H), 1.41 – 1.33 (m, 8H), 0.93 (t, $J = 6.7$ Hz, 6H). ^{13}C NMR (151 MHz, CDCl$_3$) δ 154.92, 145.14, 141.10, 140.68, 127.89, 127.14, 125.71, 122.35, 121.97, 31.71, 30.65, 30.46, 29.05, 22.66, 14.13. MS (m/z): calcd. for C$_{30}$H$_{32}$N$_4$S$_4$, 576.8540; found, 577.1588.

DTNT: **Compound 8** (402 mg, 1 mmol) and tributyl-(4-hexyl-2-thienyl)-stannane (1.37g, 3 mmol) was added to 50 mL of toluene in a flask. The reaction mixture was purged with argon for 15 minutes. Then, the catalyst Pd(PPh$_3$)$_4$ (58 mg) was added and the solution was purged with argon for an additional 15 minutes. The reaction mixture was stirred at 120 °C for 24 hours. The organic solvent of reaction mixture was removed by vacuum evaporation and the

residue was purified by column chromatography on silica gel using PE:DCM (3:1, *v/v*) as eluent to afford **DTNT** as red solid (438 mg, 76% yield). ^{1}H NMR (600 MHz, CDCl$_3$) δ 9.00 (s, 2H), 8.13 (s, 2H), 7.13 (s, 2H), 2.73 (m, 4H), 1.74 (m, 4H), 1.57 – 1.31 (m, 16H), 0.92 (t, 6H).^{13}C NMR (151 MHz, CDCl$_3$) δ 153.50, 152.48, 144.47, 138.64, 129.83, 126.74, 124.76, 122.53, 122.27, 31.74, 30.69, 30.53, 29.10, 22.67, 14.14. MS (m/z): calcd. for C$_{30}$H$_{32}$N$_4$S$_4$, 576.8540; found, 577.1587.

1.3. OSCs Fabrication and Characterization

Device fabrication: The conventional structure of ITO/PEDOT:PSS/2-PACz/Polymer_Donor:BTP-eC9/PNDIT-F$_3$N/Ag was used to fabricate the OSCs. The indium tin oxide (ITO) substrates were cleaned sequentially by sonication with detergent, deionized water (DIW), and isopropanol. After being dried in an oven at 60 ^{o}C overnight, the substrates were treated with an oxygen plasma for 5 min and then coated with PEDOT:PSS (CLEVIOS P VP Al 4083) (diluted by DIW, $V_{PEDOT:PSS} : V_{DIW}$ = 1:2) at 3000 rpm for 30 s. The 2-PACz solution (0.27 mg mL^{-1} in anhydrous ethanol) was then spin-coated on PEDOT:PSS layer and the substrates was annealed at 70 ^{o}C for 4 min in glovebox to obtain a bistratal hole transport layer. The blend solutions, with a donor-to-acceptor ratio of 1:1.2 (*w/w*) for PiBT:BTP-eC9, 1.3:1 (*w/w*) for PiNT:BTP-eC9, and 1:1.5 (*w/w*) for PNT:BTP-eC9 were prepared by dissolving them in chloroform solvent containing 0.25% CN additive. The total concentration of the solution was adjusted to 12 mg mL^{-1} for PiBT:BTP-eC9, 16.1 mg mL^{-1} for PiNT:BTP-eC9 and 20 mg mL^{-1} for PNT:BTP-eC9. Subsequently, these solutions (PiNT:BTP-eC9 solution at room temperature, PiBT:BTP-eC9 and PNT:BTP-eC9 solutions at 50 ^{o}C) were spin-coated onto a 2-PACz layer. After removing the additive via vacuuming for 2 hours. A 5 nm PNDIT-F$_3$N (0.5 mg mL^{-1} in MeOH) was spin-coated onto the active layers as a cathode interface. Finally, 100 nm silver was thermally deposited on top of the interface through a shadow mask in a vacuum chamber at a pressure of 1×10^{-7} mbar. The effective area of the device was confined to 0.04 cm^2 by a non-refractive mask to improve the accuracy of measurements.

Device characterization: The current density-voltage (*J-V*) characteristics were measured under a computer-controlled Keithley 2400 source meter under 1 sun, AM 1.5G solar simulator

(Taiwan, Enlitech SS-F5). Prior to the test, the light intensity was calibrated by a standard silicon solar cell (certified by China General Certification Center) giving a value of 100 mW cm^{-2} during the test of *J-V* characteristics. The external quantum efficiency (EQE) spectra were recorded with a QE-R measurement system (Enlitech, QE-R3011, Taiwan).

2. Computational Analyses

Gaussian 16 (Revision C.02) code [2] was used to perform density functional theory (DFT) calculations at the non-empirically tuned B3LYP-D3(BJ)/TZVP [3-5] level of theory. The side chains of PNT and PiNT monomers were modeled as methyl groups to reduce the computational cost since it has only marginal influence on the intrinsic electronic and optical properties of the π-conjugated backbones. For the potential energy surface (PES) modeling (Fig. S5), the dihedral angle between the methylthiophene and core unit were scanned at an interval of 10° between the -180° and 180° conformations. In the calculation of highest occupied molecular orbital (HOMO) and lowest unoccupied molecular orbital (LUMO) energy levels, the single point energy was calculated under B3LYP-D3(BJ)/Def2TZVP [3-5] level for high precision calculations. We considered a total of 50 excited states from S_1 to S_{50} at the theoretical level of ωB97X-D /Def2tzvp and calculated the electron-hole distribution and transition dipole moment (TDM) from S_0 to S_1. The wavefunction software Multiwfn [6] and VMD [7] were used for analysing PES and electron-hole overlapping (Sr index). The larger the Sr index, the greater the overlap of holes and electrons; the smaller the value, the more significant is the separation of holes and electrons. The intensity corresponding to the jump from the ground state to the excited state i embodied in the UV-Vis spectrum (proportional to the integral area of the absorption peak) corresponds to the vibronic intensity. The square of the mode of the jump dipole moment is equal to the sum of the x, y, and z parts of the contribution. The x part of this, for example, is related to the interaction of the system with the electric field oscillating in the x direction.

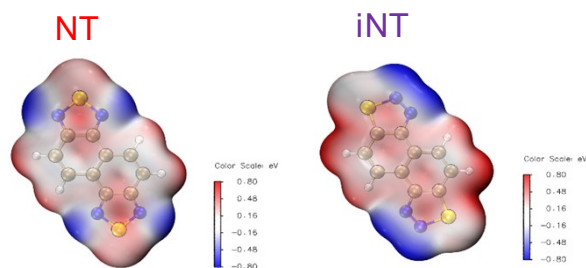## 2.1 DFT-Calculated Electrostatic Potential (ESP) Distribution

Fig. S1. Computed electrostatic potential (ESP) distribution of NT and iNT unit.

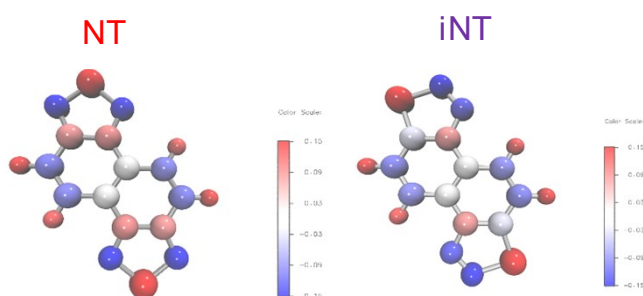## 2.2 DFT-Calculated Atomic Dipole Corrected Hirshfeld (ADCH) Charge Distribution

Fig. S2. Computed Atomic Dipole Corrected Hirshfeld (ADCH) charge distribution of NT and iNT unit.

2.3 DFT-Calculated UV－Vis Absorption Spectra and Excited State Characteristics

Table S1. Calculated excited state properties of PiBT, PNT, and PiNT monomers.

Structure	TDM_x [a.u.]	TDM_y [a.u.]	TDM_z [a.u.]	Sr [a.u.]	Osc. strength	E_{HOMO} [eV]	E_{LUMO} [eV]
PiBT	4.66	1.38	0.08	0.72	1.33	−5.16	−2.51
PNT	−4.24	0.15	0.07	0.76	1.08	−5.18	−3.17
PiNT	−4.52	1.05	0.04	0.81	1.57	−5.31	−2.77

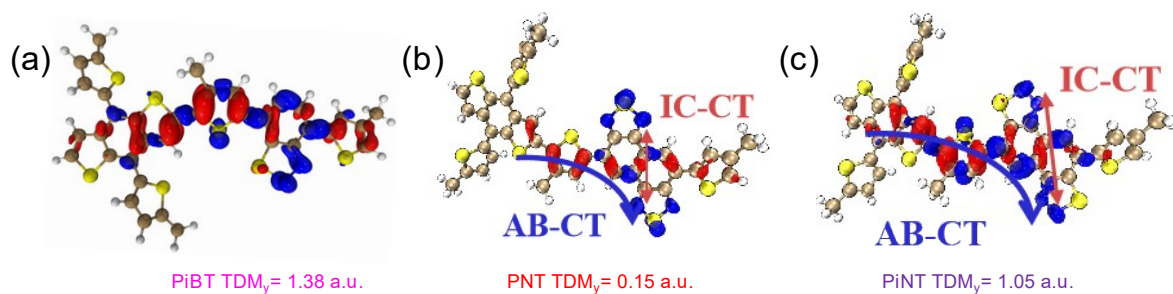## 2.4 DFT- Charge Density Differences.

Fig. S3. The charge density difference (CDD) of (**a**) PiBT, (**b**) PNT, and (**c**) PiNT monomers.

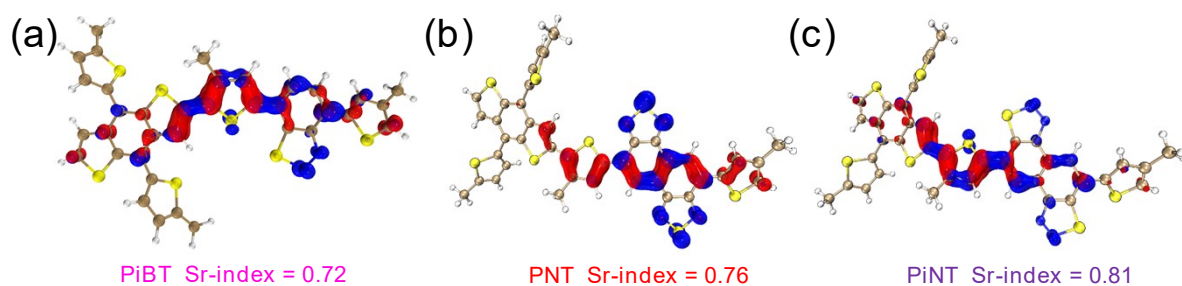## 2.5 DFT- Electron-hole Distributions

Fig. S4. The electron-hole distributions of (**a**) PiBT, (**b**) PNT, and (**c**) PiNT monomers.

2.6 DFT- Potential Energy Surface (PES) Scan Analyses

The core units of PNT and PiNT have highly symmetric structures, with the difference being the position of sulfur(S) atoms. This results in different bonding interactions affecting the torsion angle when the molecules are at the 0-degree plane. For PNT, the main interactions are N-S and H-H, while for PiNT, it is S-S and H-H. When attempting to cross the 0-degree plane, the molecules need to overcome the steric hindrance caused by the corresponding bonding interactions. To compare the differences in steric hindrance at the 0-degree plane, we scanned the dihedral angles formed by the core and the side thiophenes (MeThNT and MeThiNT models). As shown in Fig. S5, our DFT calculations showed that MeThNT only needs to overcome a negligible steric hindrance with an energy barrier of 0.004 eV. However, for MeThiNT, we found a significant energy barrier of 0.044 eV, which could lead to a larger dihedral angle compared to MeThNT. These results are consistent with the single-crystal
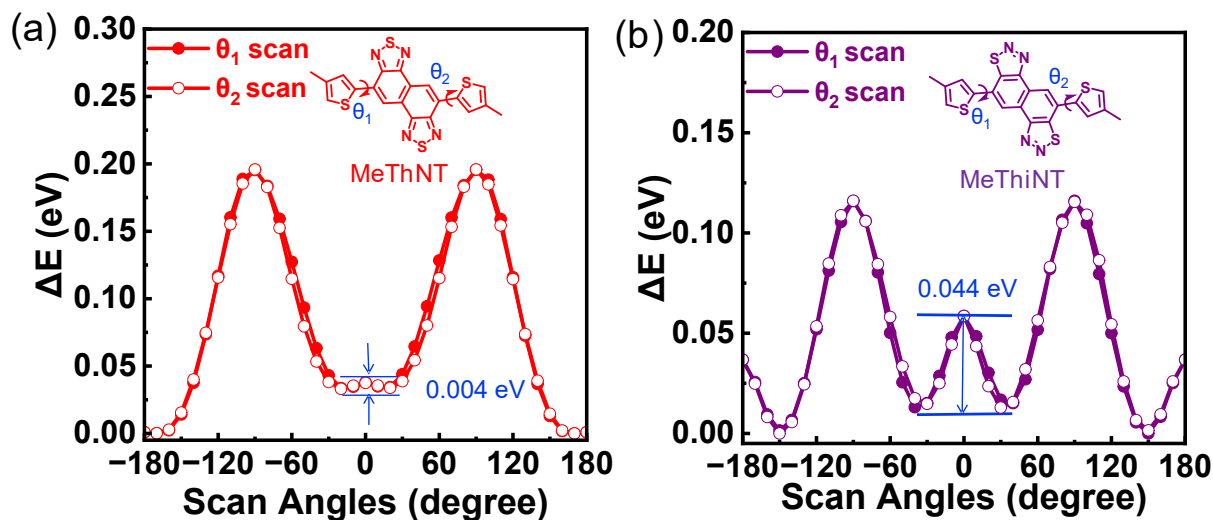
11

measurement.

Fig. S5. PES scans from $-180\,^{\circ}$ to $180\,^{\circ}$: (**a**) MeThNT, and (**b**) MeThiNT. (The alkyl chain was replaced by methyl group to save time.)

2.7 DFT- Electron Localization Function and Mayer Bond Order Analyses

To further investigate the origin of this large energy barrier, we calculated the Electron Localization Function (ELF) [8-11] and Mayer bond orders [12], which reflect the extent of atomic interactions by examining the electron density and bonding strength. The ELF was used for studying changes in electron density during molecule formation and investigating the nature of interatomic interactions (see Fig. S6). By constructing a density difference distribution $\Delta\rho(r)$, it is possible to directly isolate and study changes in the density distribution of the original atoms caused by the formation of interatomic interactions. This distribution is obtained by subtracting the density obtained by overlapping the densities of undistorted atoms. As demonstrated in Fig. S6, the ELF describes the efficiency of Pauli repulsion [12] at a given point of the molecular space; it has been widely utilized as a convenient descriptor of interatomic interactions in different systems. The Mayer bond orders reflect the number of electron pairs shared between the two atoms. A larger bond order implies a stronger covalent interaction. Our results showed that in MeThNT model, the Mayer bond orders for H-H and N-S were only 0.001 and 0.021, indicating weak interactions between the atoms. In contrast, for MeThiNT, the S-S Mayer bond order was 0.047, much stronger than the N-S interaction in MeThNT. This

may be the reason for the significant difference in torsion angles between the PNT and PiNT, as the strong repulsion between the outer electrons of the sulfur atoms in the side thiophene rings and the outer electrons of the S atom in the isomeric core results in a large energy barrier, preventing the thiophene units from crossing the 0-degree plane and causing a larger torsion angle.
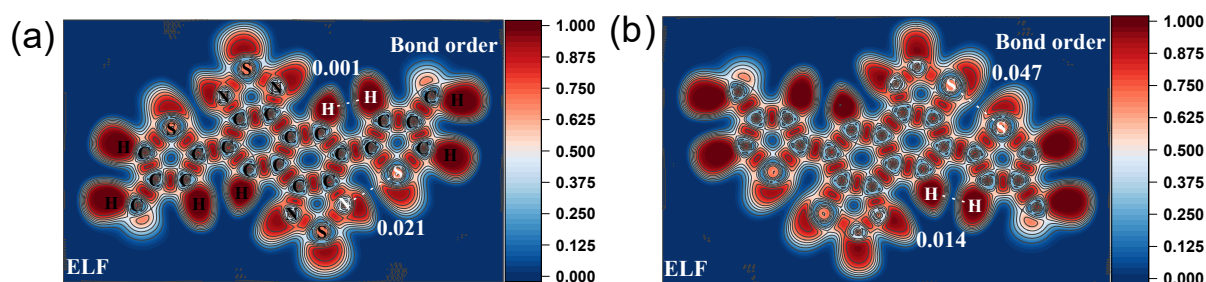

Fig. S6. Electron localization function and Mayer bond order analyses of (**a**) MeThNT and (**b**) MeThiNT models.

3. Crystal Growth and Single Crystal Determination

X-ray data collection, structure solution, and refinement: the single crystals of DTiNT, and DTNT were grown at room temperature using solvent diffusion or slow evaporation. On the Bruker D8 Venture instrument, the single-crystal X-ray diffraction (SXRD) data of DTiNT, and DTNT were collected with a Cu Kα X-ray source (λ = 1.54184 Å) at temperature in the table below. As shown in **Table S2**, the crystal information and experimental details of the structure determination are summarized, including bond length, bond angles, and dihedrals angles. The structure was solved by Olex2 and optimized by a full-matrix least-squares procedure based on F2 (SHELXL). The structure was first coarsely modified, and the non-hydrogen atoms were finely modified using various anisotropic thermal parameters. The positions of the atoms were then derived from geometric calculations and refined.

Table S2. The crystal information and experimental details of the structure determination for DTiNT and DTNT.

Compound	DTiNT	DTNT
Formula	$C_{30}H_{32}N_4S_4$	$C_{30}H_{32}N_4S_4$
Formula weight	576.83	576.83

Temperature/K	112(17)	149.99(10)
Radiation	Cu Kα (λ = 1.54184)	Cu Kα (λ = 1.54184)
$D_{calc.}$ / g cm^{-3}	1.410	1.400
μ/mm^{-1}	3.429	3.403
Space Group	I 2/a	P-1
a/Å	19.9590 (6)	4.6583(3)
b/Å	4.0485 (2)	16.9585(9)
c/Å	34.38950 (19)	18.5967(10)
α/°	90	108.812
β/°	102.127(3)	94.516
γ/°	90	97.138
V/Å^3	2716.8 (14)	1368.78(14)
Z	4	2
F_{000}	1216.0	608.0
$F_{000'}$	1223.85	611.93
M_r	328.46	576.83
h	24	5
k	4	20
l	42	22
Theta (max)	74.186	66.601
T_{min}	0.428	0.698
T_{max}	1.000	0.762
N_{ref}	2648	4763
wR_2 (all data)	0.129 (2648)	0.3394 (4763)
R_1 (all data)	0.0452 (2370)	0.1219 3629)

4. Gel Permeation Chromatography Measurements

The molecular weights of PNT and PiNT were obtained on an Acquity Advanced Polymer Chromatography (Waters) with a high-temperature chromatograph in 1,2,4-trichlorobenzene at 150 °C and using a calibration curve of polystyrene standards.
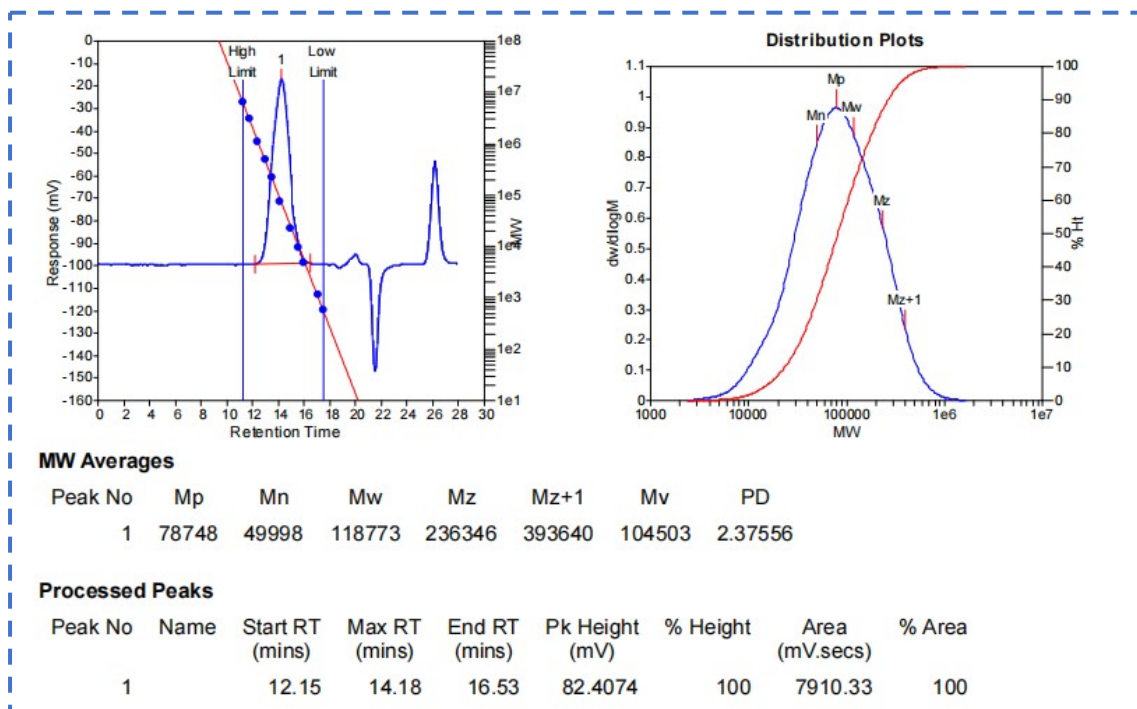
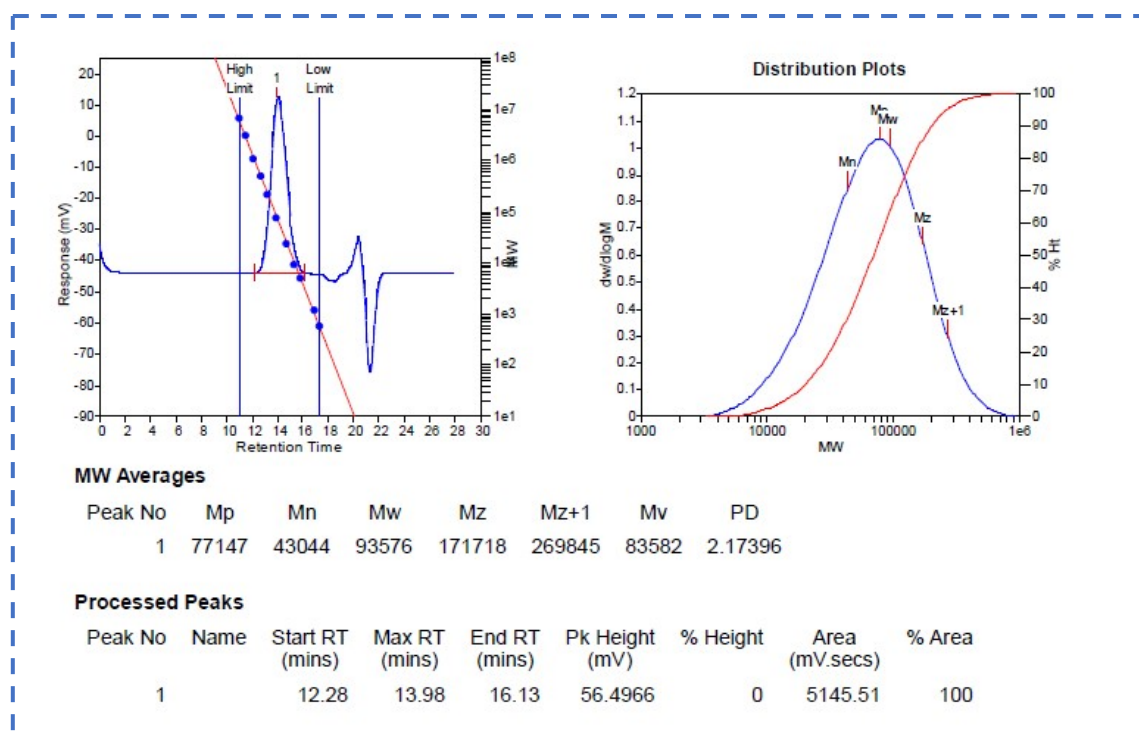**Fig. S7.** High-temperature GPC measurement of PiBT.

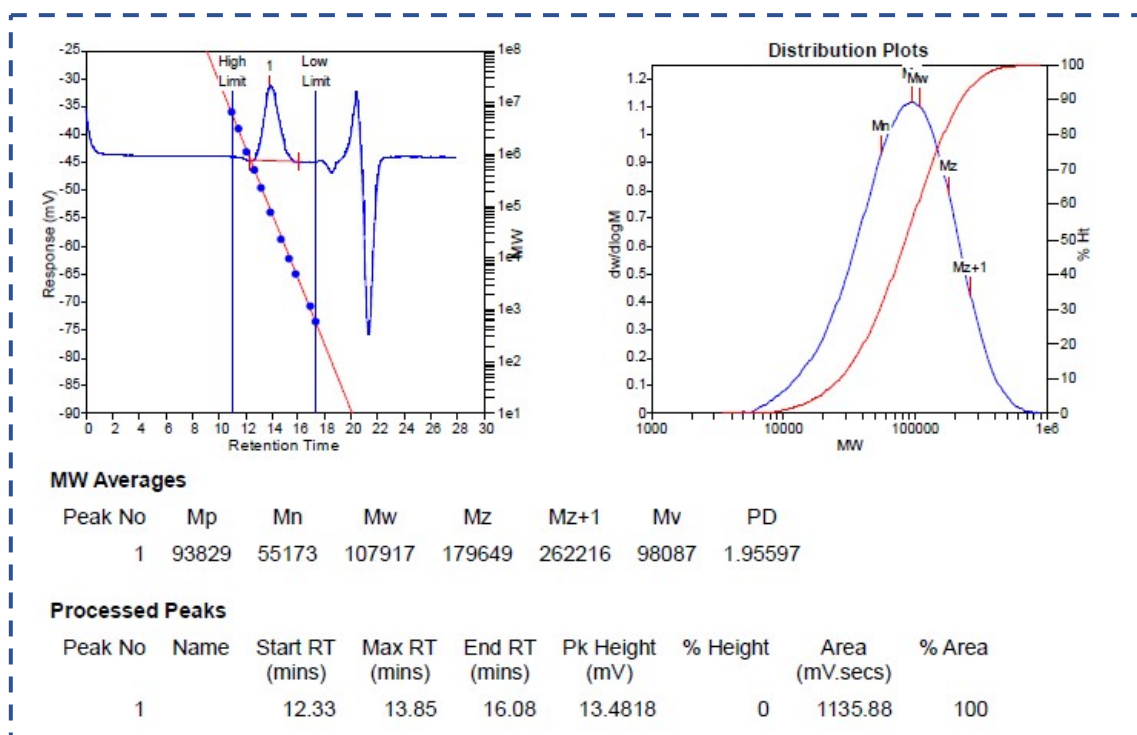**Fig. S8.** High-temperature GPC measurement of PNT.

MW Averages

Peak No	Mp	Mn	Mw	Mz	Mz+1	Mv	PD
1	93829	55173	107917	179649	262216	98087	1.95597

Processed Peaks

Peak No	Name	Start RT (mins)	Max RT (mins)	End RT (mins)	Pk Height (mV)	% Height	Area (mV.secs)	% Area
1		12.33	13.85	16.08	13.4818	0	1135.88	100

Fig. S9. High-temperature GPC measurement of PiNT.

5. UV−Vis Absorption Spectra

UV-Vis absorption spectra were recorded on a SHIMADZU UV-3600 spectrophotometer from 300 nm to 1000 nm, corrected for quartz absorption. For solution absorption test, polymer donors was dissolved in CF or CB with a concentration of ca. 10^{-5} mol L^{-1}. The solid films (ca. 100 nm) for spectrum test were prepared by spin-coating polymeric CF solution onto quartz plate.
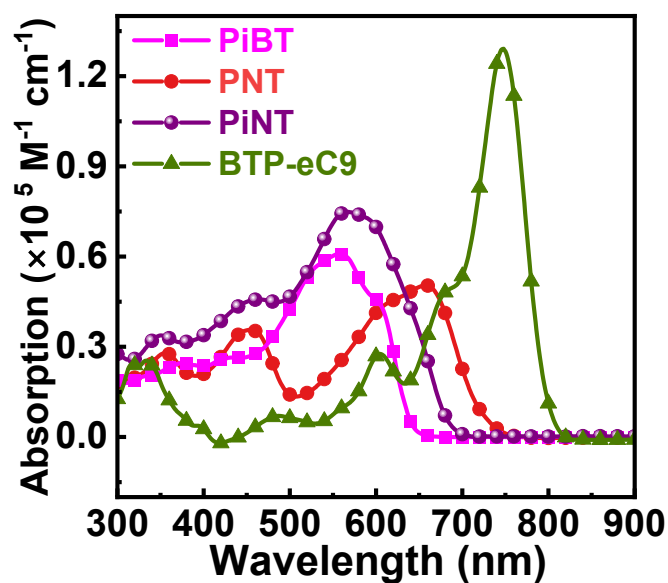
Fig. S10. Absorption spectra of PiBT, PNT, PiNT, and BTP-eC9 in dilute CF solutions. (repeat unit concentration of ca. 1×10^{-5} M).
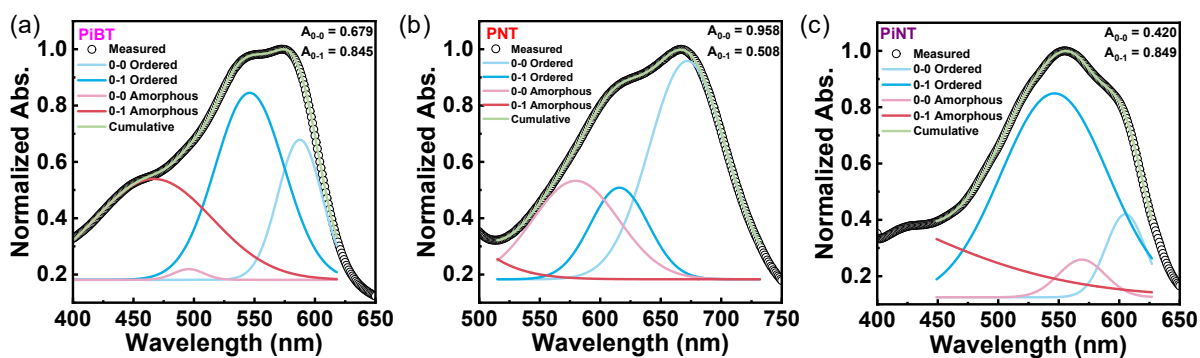
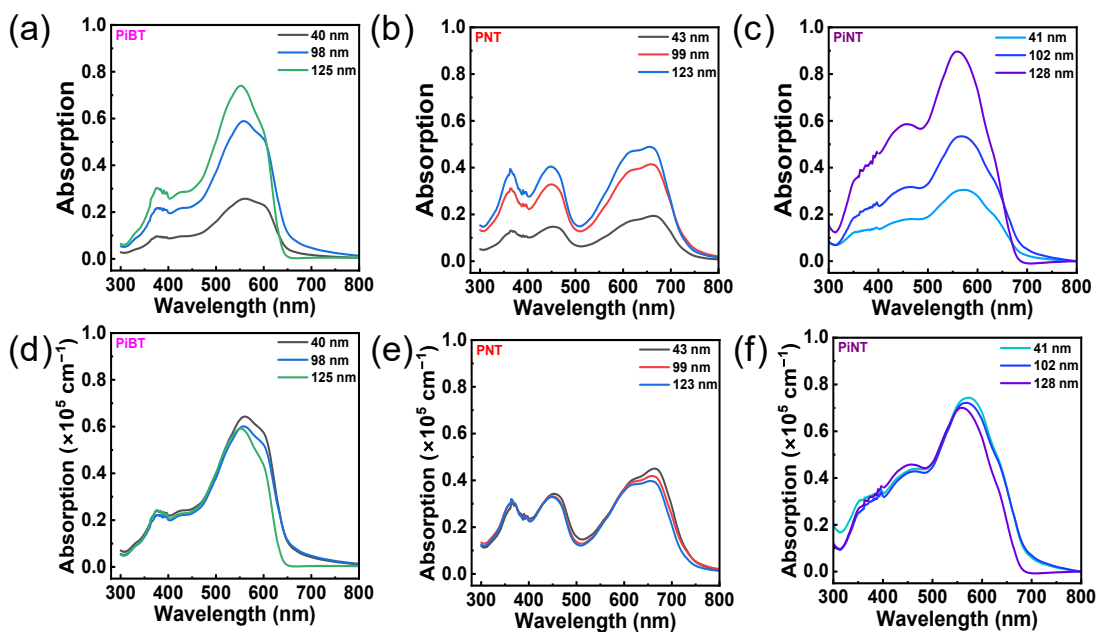**Fig. S11**. Absorption spectra of the polymer donor films, and corresponding fitting analyses.

Fig. S12. The film absorption spectra of (a) PiBT, (b) PNT, and (c) PiNT with different thicknesses; the calculated extinction coefficients of (d) PiBT, (e) PNT, and (f) PiNT with different film thicknesses.
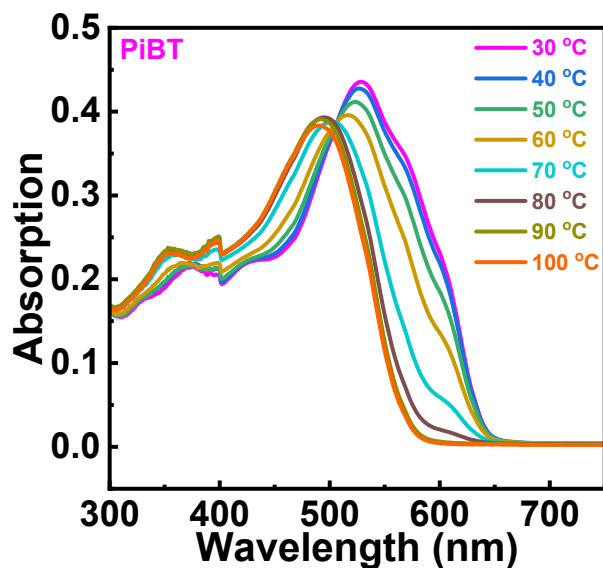

Fig. S13. The temperature-dependent UV–Vis absorption spectra of PiBT in dilute chlorobenzene solution.

6. Energy Levels Estimation Measurements

Cyclic voltammetry (CV) measurements were conducted on a CHI660e Electrochemical Workstation equipped with a glassy carbon working electrode, a platinum wire counter electrode, and a saturated calomel reference electrode. The 0.1 mol L^{-1} tetrabutylammonium hexafluorophosphate in anhydrous acetonitrile was used as the supporting electrolyte. The potential of saturated calomel electrodes (SCE) was internally calibrated using the ferrocene/ferrocenium redox couple (Fc/Fc$^+$) as 0.40 V, which has a known reduction potential of –4.80 eV. Energy levels were determined by CV measurements, $E_{HOMO} = -e(E_{ox} + 4.40)$V, $E_{LUMO} = -e(E_{re} + 4.40)$V;

Ultraviolet photoelectron spectroscopy (UPS) measurements were recorded using a RIKEN KEIKI spectrometer (Model AC-3) with a power setting of 30 nW and a power number of 0.5. Samples for UPS measurement were prepared on glass substrate.
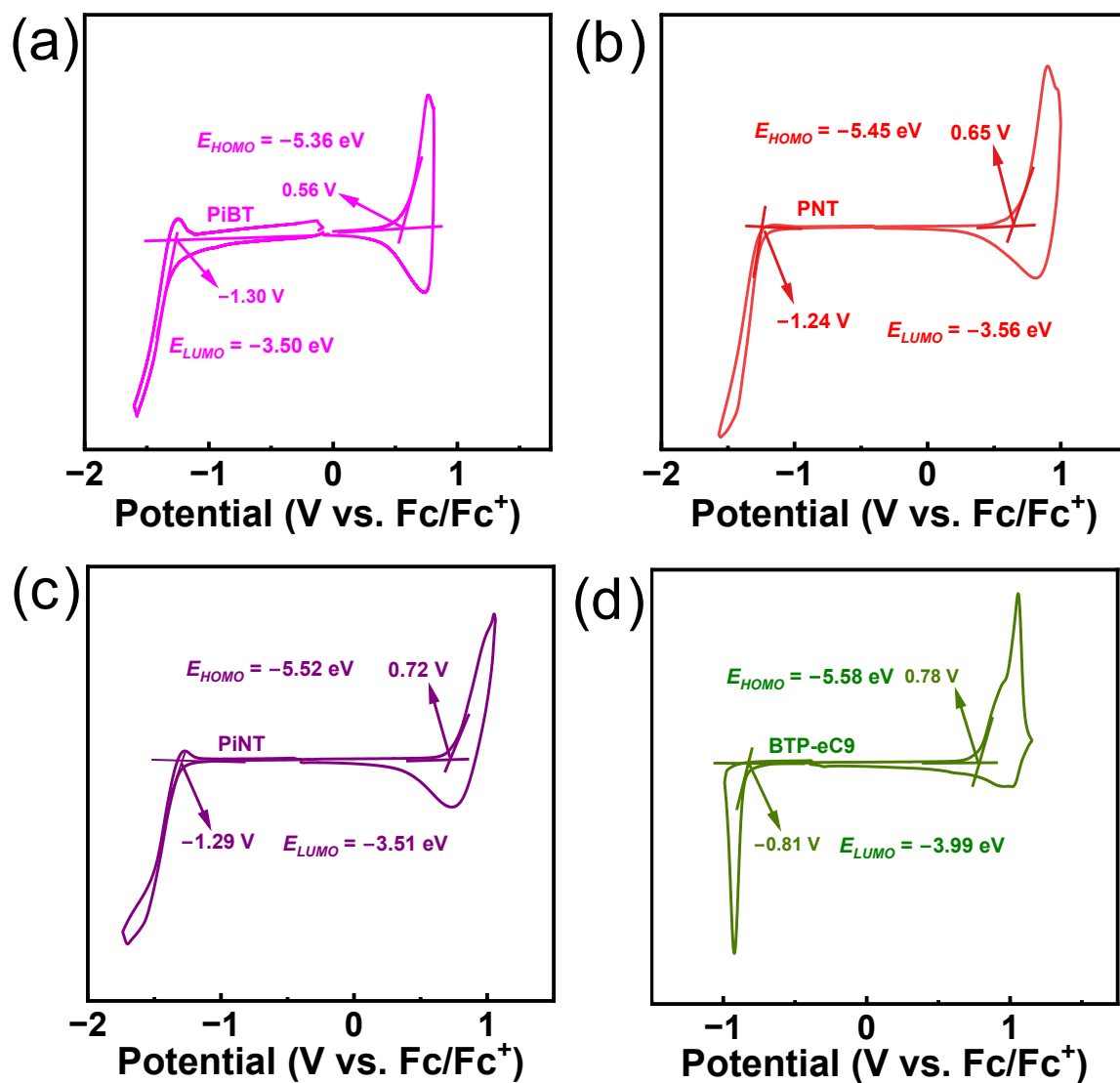
Fig. S14. CV curves of (**a**) PiBT, (**b**) PNT, (**c**) PiNT, and (**d**) BTP-eC9.
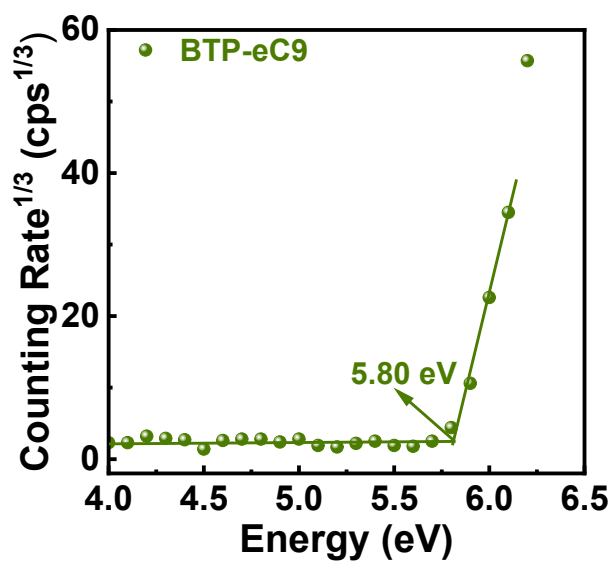

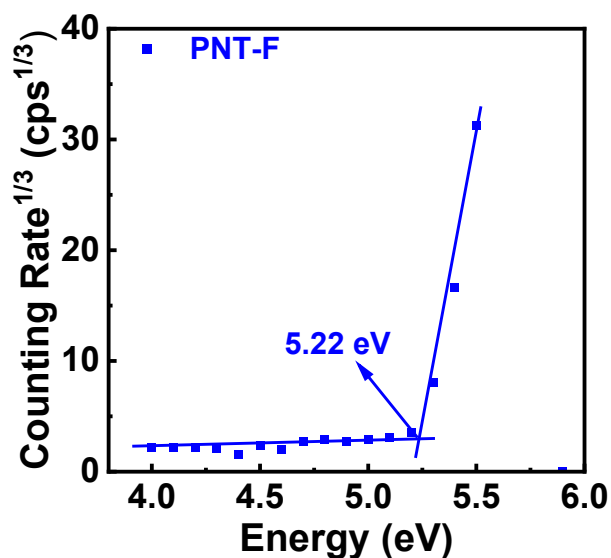**Fig. S15.** Ultraviolet photoelectron spectroscopy curve of BTP-eC9.

Fig. S16. Ultraviolet photoelectron spectroscopy curve of polymer PNT-F.

7. Additional Data of OSC optimization

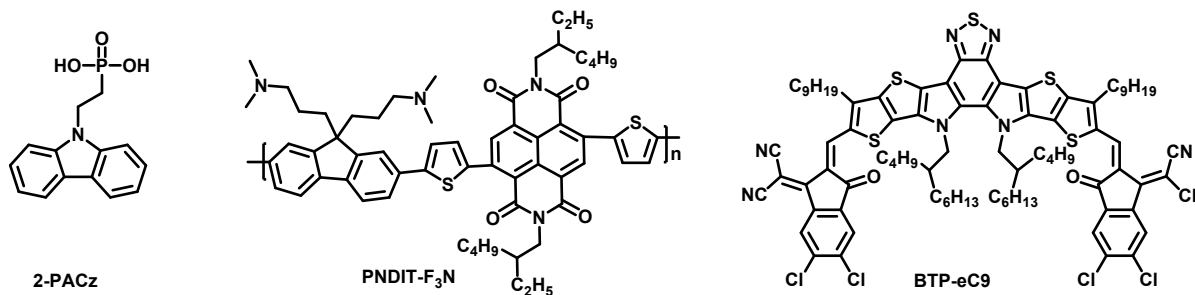## 7.1 Chemical Structures of Interface Layer and Acceptor Materials

Fig. S17. Chemical structures of 2-PACz, PNDIT-F$_3$N, and BTP-eC9.

7.2 Photovoltaic Performance as a function of Varied Donor:Acceptor Ratios

Table S3. Device performance of the PNT: BTP-eC9 solar cells with different D/A weight ratios under AM1.5G irradiation (100 mW cm^{-2}). The active layers were annealed at 100 °C for 10 minutes. The concentration of donor maintains as 8 mg mL^{-1} in CF containing 0.25% CN additive.

D/A ratio [wt/wt]	V_{OC} [V]	J_{SC} [mA cm^{-2}]	FF [%]	PCE [%]
1.3:1	0.79	23.6	61.5	11.5
1:1	0.79	23.9	64.1	12.1
1:1.3	0.79	24.4	71.9	13.8
1:1.5	0.79	24.9	72.4	14.2
1:1.7	0.79	24.7	68.4	13.4

Table S4 Device performance of the PiNT: BTP-eC9 solar cells with different D/A weight ratios under AM1.5G irradiation (100 mW cm^{-2}). The active layers were annealed at 100 °C for 10 minutes. The concentration of donor maintains as 7 mg mL^{-1} in CF containing 0.25% CN additive.

D/A ratio [wt/wt]	V_{OC} [V]	J_{SC} [mA cm^{-2}]	FF [%]	PCE [%]
1.5:1	0.88	27.6	73.5	17.9
1.3:1	0.88	27.8	77.6	19.1
1:1	0.88	27.8	74.3	18.2

7.3 Photovoltaic Performance as a Function of Varied Ratios of Solvent Additive

Table S5. Device performance of the PNT: BTP-eC9 solar cells with different solvent additive ratios under AM1.5G irradiation (100 mW cm^{-2}). The active layers were annealed at 100 °C for 10 minutes. The D/A weight ratio was 1:1.5. The concentration of donor maintains as 8 mg mL^{-1}.

CN [vol%]	V_{OC} [V]	J_{SC} [mA cm^{-2}]	FF [%]	PCE [%]
0	0.78	23.8	67.4	12.6
0.25	0.79	24.9	72.4	14.2
0.5	0.79	24.9	69.6	13.6

Table S6. Device performance of the PiNT: BTP-eC9 solar cells with different solvent additive ratios under AM1.5G irradiation (100 mW cm^{-2}). The active layers were annealed at 100 °C

for 10 minutes. The D/A weight ratio was 1.3:1. The concentration of donor maintains as 7 mg mL^{-1} in CF solvent.

CN [vol%]	V_{OC} [V]	J_{SC} [mA cm^{-2}]	FF [%]	PCE [%]
0	0.89	27.6	73.8	18.0
0.25	0.88	27.8	77.6	19.1
0.5	0.87	27.5	76.1	18.3

7.4 Photovoltaic Performance of PiNT with Different Acceptor

Table S7. Device performance of the PiNT:Y6, PiNT:L8-BO, and PiNT:DTY6 solar cells under AM1.5G irradiation (100 mW cm^{-2}). The active layers were annealed at 100 °C for 10 minutes. The D/A weight ratio was 1.3:1. The concentration of donor maintains as 7 mg mL^{-1} containing 0.25% CN additive.

Acceptors	V_{OC} [V]	J_{SC} [mA cm^{-2}]	FF [%]	PCE [%]
Y6	0.90	27.4	71.7	17.6
L8-BO	0.93	25.2	77.0	17.9
DTY6	0.90	24.8	67.1	15.0

7.5 Photovoltaic Performance of Different Batches of Polymer Donors

Table S8. Device performance of the PiNT:BTP-eC9 OSCs with different batches of PiNT polymers under AM1.5G irradiation (100 mW cm^{-2}). The active layers were annealed at 100 °C for 10 minutes. The D/A weight ratio was 1.3:1. The concentration of the donor maintains as 7 mg mL^{-1} containing 0.25% CN additive.

PiNT batches	V_{OC} [V]	J_{SC} [mA cm^{-2}]	FF [%]	PCE [%]
M_n =31.2 kDa, M_w = 62.1 kDa	0.89	27.8	74.1	18.1
M_n = 55.2 kDa, M_w = 107.9 kDa	0.88	27.8	77.6	19.1
M_n = 84.0 kDa, M_w = 193.6 kDa	0.88	28.5	72.8	18.3

Table S9. Device performance of the PNT:BTP-eC9 OSCs with different batches of PNT polymers under AM1.5G irradiation (100 mW cm^{-2}). The active layers were annealed at 100 °C for 10 minutes. The D/A weight ratio was 1:1.5. The concentration of donor maintains as 8 mg mL^{-1} containing 0.25% CN additive.

PNT batches	V_{OC} [V]	J_{SC} [mA cm^{-2}]	FF [%]	PCE [%]
M_n =26.8 kDa, M_w = 52.8 kDa	0.78	24.8	71.2	13.8
M_n =43.0 kDa, M_w = 93.6 kDa	0.79	24.9	72.4	14.2
M_n =73.6 kDa, M_w = 155.2 kDa	0.77	24.0	56.4	10.4

Table S10. Device performance of the PiBT:BTP-eC9 OSCs with different batches of PiBT polymers under AM1.5G irradiation (100 mW cm^{-2}). The active layers were annealed at 100 °C for 10 minutes. The D/A weight ratio was 1:1.2. The concentration of donor maintains as 6 mg mL^{-1} containing 0.25% CN additive.

PiBT batches	V_{OC} [V]	J_{SC} [mA cm^{-2}]	FF [%]	PCE [%]
M_n =34.7 kDa, M_w = 63.6 kDa	0.71	23.4	51.1	8.5
M_n =40.9 kDa, M_w = 74.7 kDa	0.71	24.7	50.7	8.9
M_n =50.0 kDa M_w = 118.8 kDa	0.72	24.7	52.0	9.2

Table S11. Device performance of the PNT-F:BTP-eC9 OSCs with different batches of PiBT polymers under AM1.5G irradiation (100 mW cm^{-2}). The active layers were annealed at 100 °C for 10 minutes. The D/A weight ratio was 1:1.5. The concentration of donor maintains as 8 mg mL^{-1} containing 0.25% CN additive.

PNT-F batches	V_{OC} [V]	J_{SC} [mA cm^{-2}]	FF [%]	PCE [%]
M_n =37.1 kDa, M_w = 84.0 kDa	0.79	25.9	69.0	14.1
M_n =75.3 kDa, M_w = 247.9 kDa	0.79	26.4	59.9	12.6

7.6 Chemical Structures of Fluoro-substituted Polymer PNT-F
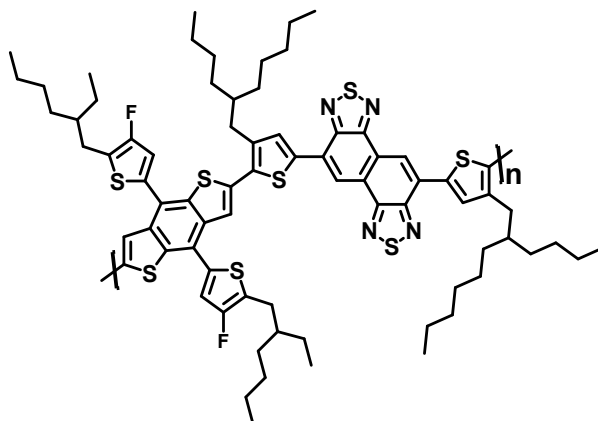

Fig. S18. Chemical structure of fluoro-substituted polymer **PNT-F** (PNT-F was synthesized as the procedure for polymer PNT).

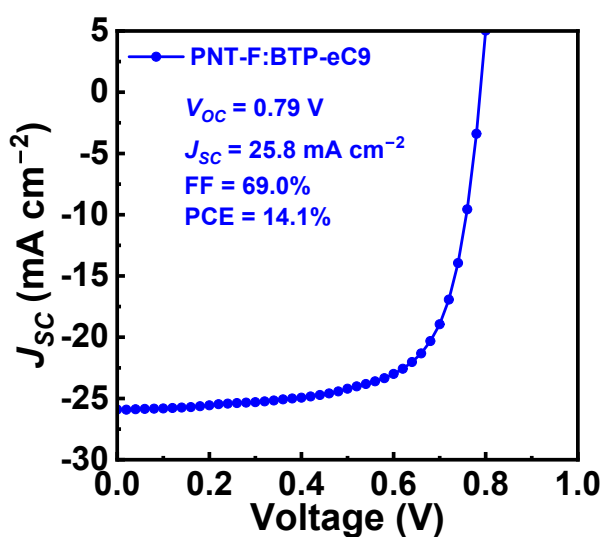## 7.7 Photovoltaic Performance of OSC based on PNT-F:BTP-eC9

Fig. S19. The $J-V$ curve measured from optimal PNT-F: BTP-eC9-based devices (The active layers were annealed at 100 °C for 10 minutes. The D/A weight ratio was 1:1.5. The concentration of donor maintains as 8 mg mL^{-1}. The fabrication process was identical to PNT: BTP-eC9 system).

7.8 Stability and Scalability of OSC based on PiNT:BTP-eC9
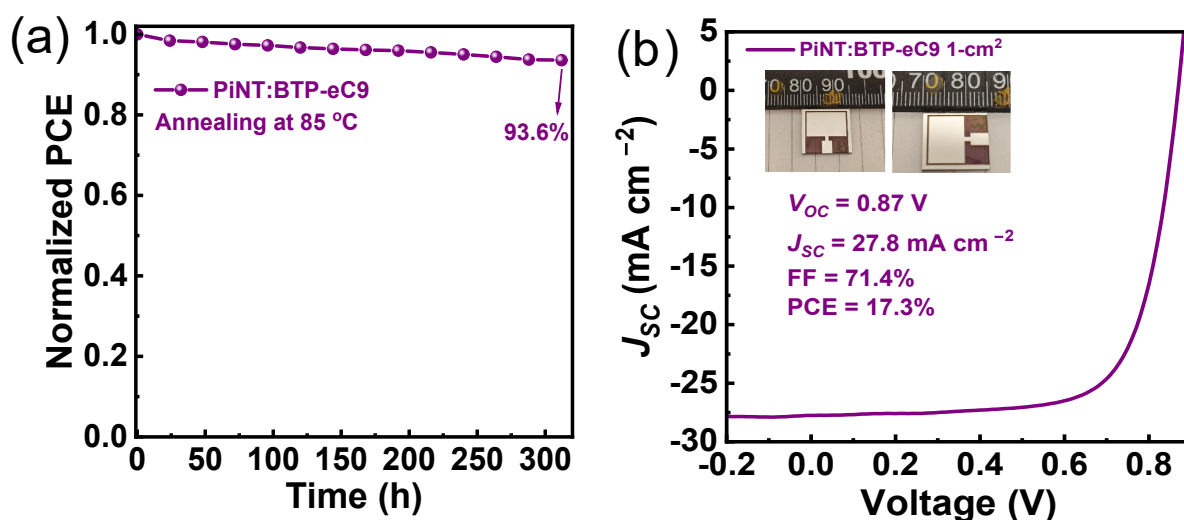
Fig. S20. (a) The normalized PCE of PiNT:BTP-eC9-based OSCs after annealing at 85°C for different durations; (b) the *J-V* curve of a 1-cm² OSC fabricated with the PiNT:BTP-eC9 blend.

7.9 Photovoltaic Performance of the Representative WBG Bipolymer Donors
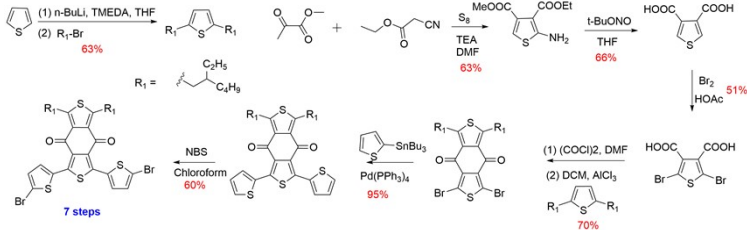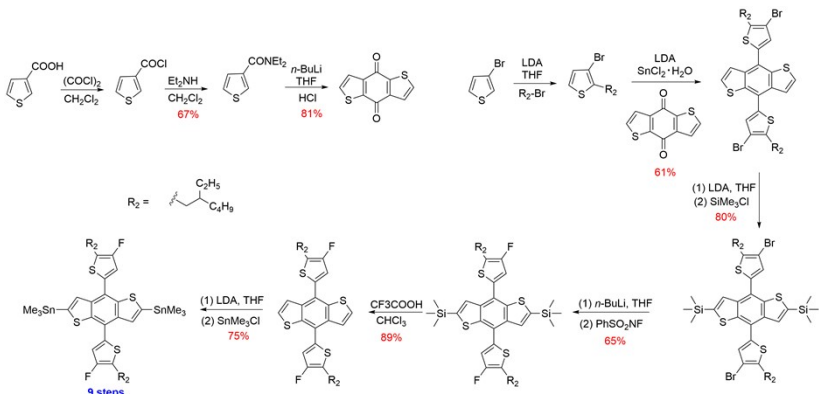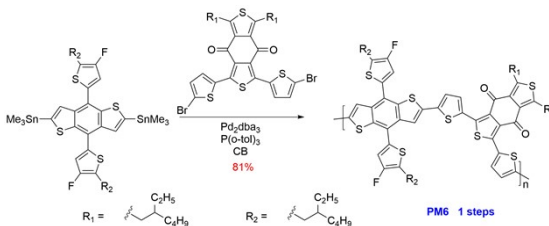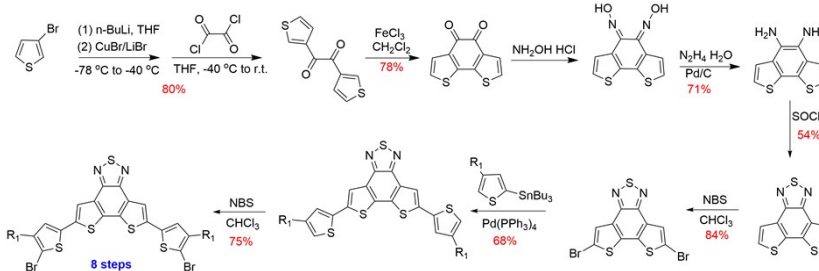
Table S12. Summary of photovoltaic parameters for the representative WBG bipolymer donor combined with Y-series acceptors.
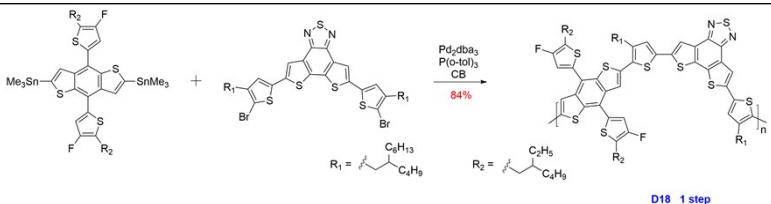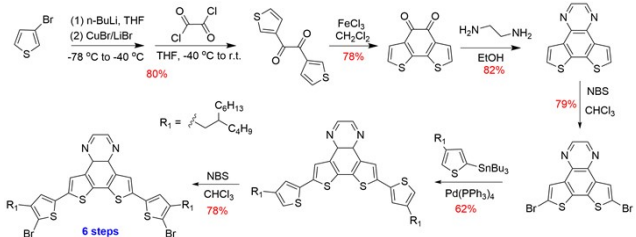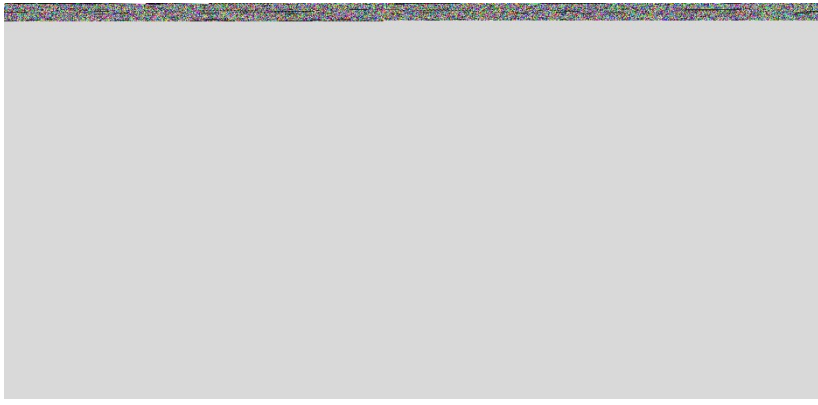
Donor	Acceptor	V_{OC} [V]	J_{SC} [mA cm^{-2}]	FF [%]	$J_{SC} \times V_{OC}$ [mW cm^{-2}]	PCE [%]	References
PM6	Y6	0.83	25.3	74.8	21.0	15.7	*Joule* **2019**, *3*, 1140–1151
P2F-EHp	Y6	0.81	26.7	74.1	21.6	16.2	*Sci. China Chem.* **2019**, *62*, 746
PTQ10	Y6	0.83	26.7	75.1	22.2	16.5	*Sci. China Chem.* **2020**, *63*, 265
PM6	BTP-eC9	0.84	26.2	78.3	22.0	17.3	*Adv. Mater.* **2020**, *32*, 1908205
D18	Y6	0.86	27.7	76.6	23.8	18.2	*Sci. Bull.* **2020**, *65*, 272.
D18	Y6Se	0.84	28.0	75.3	23.5	17.7	*J. Am. Chem. Soc.* **2020**, *142*, 18741
D18-Cl	Y6	0.86	27.1	73.3	23.3	17.1	*J. Semicond.* **2021**,*42*, 010501
PTQ10	m-BTP-PhC6	0.88	25.3	79.3	22.3	17.7	*Energy Environ. Sci.* **2021**, *14*, 3469.
PBQx-TF	eC9-2Cl	0.87	25.9	78.6	22.5	17.7	*Adv. Mater.* **2021**, *33*, 2102420
PM6	L8-BO	0.87	25.7	81.5	22.4	18.3	*Nat. Energy* **2021**, *6*,

605.

PM6	EH-HD-4F	0.84	27.5	79.3	23.1	18.4	*Sci. China Chem.* **2021**, *64*, 1192.
PM6	BTP-S9	0.85	26.5	78.4	22.5	17.6	*Nat. Commun.* **2021**, *12*, 4627
PB2	BTP-eC9	0.86	26.2	77.9	22.5	17.7	*Adv. Mater.* **2022**, *34*, 2105803.
PBCT-2F	Y6	0.85	27.2	74.0	23.1	17.1	*Energy Environ. Sci.* **2021**, *14*, 5530.
PM6	EHN6SEH-4F	0.81	28.8	74.6	23.3	17.5	*Mater. Horiz.* **2022**, *9*, 403.
PM6	Y-BO-FCl	0.85	26.5	77.9	22.5	17.5	*Energy Environ. Sci.* **2022**, *15*, 320.
PTQ10	BTP-FTh	0.85	26.3	76.7	22.4	17.2	*Adv. Mater.* **2022**, *34*, 2109516.
PW2	BTP-eC9-4F	0.87	27.3	72.7	23.8	17.2	*Adv. Energy Mater.* **2022**, *12*, 2104028.
D18-Cl	BTF	0.86	26.9	74.6	22.4	17.0	*Energy Environ. Sci.* **2022**, *15*, 645.
PBDT-Cl	A4	0.84	26.9	76.0	22.6	17.2	*Adv. Funct. Mater.* **2022**, *32*, 2201150.
PBQ6	m-TEH	0.88	26.6	79.0	23.4	18.5	*Energy Environ. Sci.* **2022**, *15*, 2011.
PM6	BTP-H2	0.93	25.3	78.5	23.5	18.5	*Energy Environ. Sci.* **2022**, *15*, 2537.
PM6	2BTP-2F-T	0.91	25.5	78.3	23.2	18.2	*Adv. Sci.* **2022**, *9*, 2202513.
PM6	CH6	0.88	26.6	78.4	23.4	18.3	*Angew. Chem. Int. Ed.* **2022**, *61*, 202209580
PBTz-F	L8-BO	0.90	26.7	77.6	24.0	18.6	*Adv. Mater.* 2023, *35*, 2300631
D18	BTP-Th	0.89	26.8	79.7	23.9	19.0	*Angew. Chem.* 2023, *135*, e202301958
PM6	BTP-eC9	0.86	27.9	80.4	24.0	19.3	*Nat. Commun.* 2023, *14*, 1760
PM6	CH-BBQ	0.88	26.2	78.9	23.1	18.2	*Angew. Chem. Int. Ed.* 2023, e202308832
PBQx-F	eC9-2Cl	0.88	27.2	80.4	23.9	19.2	*Adv. Mater.* 2023, *35*, 2301583.
PM6	CH22	0.88	26.7	80.6	23.5	19.1	*Nat. Commun.* **2023**, *14*, 4707

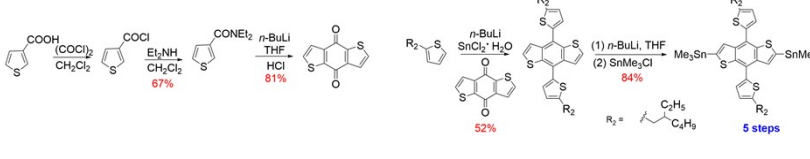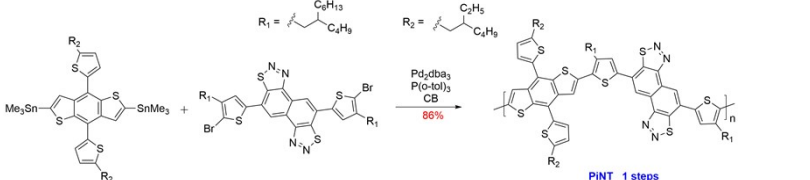| PiNT | BTP-eC9 | 0.88 | 27.8 | 77.6 | 24.6 | 19.1 | **This work** |

7.10 Comprehensive Comparison of the State-of-the-art Polymer Donors

Table S13. Comprehensive comparison of the state-of-the-art polymer donors PM6, D18, PBQx-F, PBTz-F, and PiNT in terms of synthetic procedures and total yield.

PM6: 17 steps Total yield: 0.50%	BDD acceptor: 7 steps Yield: 5.33%	References: *Org. Lett.*, 2011, **13**, 38-41; *J. Org. Chem.*, 2012, **77**, 8167-8173; *Angew. Chem. Int. Edit.*, 2016, **55**, 12996-13000.
	BDTF-DSn donor: 9 steps Yield: 11.49%	References: *Adv. Mater.*, 2015, **27**, 4655-4660. *Joule* 2021, **5**, 1209–1230.
	Polymer: 1 step Yield: 81%	Reference: *Adv. Mater.*, 2015, **27**, 4655-4660.
D18: 18 steps Total yield: 0.99%	fDTBT acceptor: 8 steps Yield: 10.25%	References: *Macromolecules* 2013, **46**, 7920-7931; *Org. Lett.*, 2012, **14**, 6138-6141; *Tetrahedron Lett.*, 2014, **55**, 4849-4852; *Macromolecules*

		2016, **49**, 9358-9370.
	BDTF-DSn donor: 9 steps Yield: 11.49%	References: *Adv. Mater.*, 2015, **27**, 4655-4660. *Joule* 2021, **5**, 1209–1230.
	Polymer: 1 step Yield: 84%	Reference: *Sci. Bull.,* 2020*,* **65**, 272–275.
PBQx-F: 16 steps Total yield: 1.44%	fDTBQ acceptor: 6steps Yield: 19.55%	References: *Macromolecules* 2013, **46**, 7920-7931; *Adv. Mater.,* 2021*,* **33***,* 2101090
	BDTF-DSn donor: 9 steps Yield: 11.49%	References: *Adv. Mater.*, 2015, **27**, 4655-4660. *Joule* 2021, **5**, 1209–1230.

	Polymer: 1 step Yield: 64%	$R_1 =$ (branched: C_6H_{13}, C_4H_9) $R_2 =$ (branched: C_2H_5, C_4H_9) Me$_3$Sn ... SnMe$_3$ + ... Br ... Br Pd$_2$dba$_3$ / P(o-tol)$_3$ / CB / 64% **PBQx-F 1 step** Reference: *Adv. Mater.*, 2021, 33, 2102420.
PBTz-F: 17 steps Total yield: 0.57%	BTz acceptor: 7 steps Yield: 6.58%	NH$_2$ + O=C–Cl → (Pyridine, 41%) → NH (P$_4$S$_{10}$, Toluene, 80%) → NH (NaH, Toluene, DMF, 80%) → S N (LDA, TMSCl, THF, –78 °C, 55%) → (Si ... Si) → (Br$_2$, Chloroform) → Br ... Br (S–SnBu$_3$, Pd(PPh$_3$)$_4$, 57%) → (NBS, THF, 80%) → Br ... Br $R_1 =$ (branched: C_6H_{13}, C_8H_{17}) **7 steps** Reference: *Adv. Mater.*, 2023, **35**, 2300631.
	BDTF-DSn donor: 9 steps Yield: 11.49%	References: *Adv. Mater.*, 2015, **27**, 4655-4660. *Joule* 2021, **5**, 1209–1230.
	Polymer 1 step Yield: 75%	$R_1 =$ (branched: C_6H_{13}, C_8H_{17}) $R_2 =$ (branched: C_2H_5, C_4H_9) Me$_3$Sn ... SnMe$_3$ + Br ... Br Pd$_2$dba$_3$ / P(o-tol)$_3$ / CB / 75% **PBTz-F 1 step** Reference: *Adv. Mater.*, 2023, **35**, 2300631.
PiNT 12 steps Total yield: 6.86%	iNT acceptor: 6 steps Yield: 33.66%	Br ... Br (Fume HNO$_3$, 88%) → NO$_2$ ... NO$_2$ (1) Na$_2$S (2) HOAC → NH$_2$ ... SH ... SH ... NH$_2$ (tBu–O–N=O, CH$_3$CN, 69%) → (Oleum, NBS) → Br ... Br (S–SnBu$_3$, Pd(PPh$_3$)$_4$, Toluene, 63%) → R$_1$ ... (NBS, Chloroform, 88%) → R$_1$ ... Br $R_1 =$ (branched: C_6H_{13}, C_4H_9) **6 steps** **This work**

	BDT-DSn donor: 5 steps Yield: 23.71%	
		Reference: *Angew. Chem. Int. Ed.,* 2011, **50**, 9697-9702.
	Polymer: 1 step Yield: 86%	
		This work

8. Atom Force Microscopy (AFM) Measurement

The atom force microscopies of blended films were tested on a Digital Instrumental DI Multimode Nanoscope III in a taping mode. The samples for the AFM measurements were prepared as the same conditions for OSC devices.
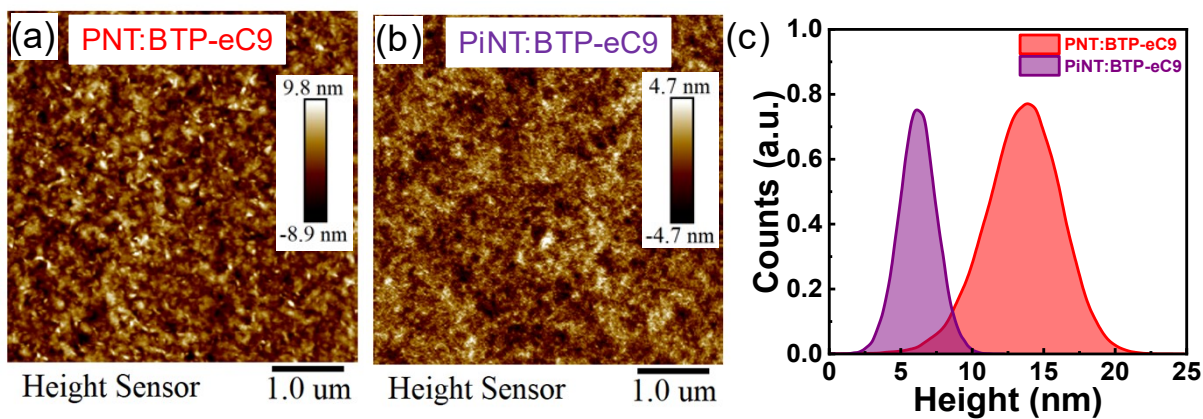
Fig. S21. AFM topography for BHJ active layers films composed of polymer donor and BTP-eC9 : (**a**) PNT:BTP-eC9 , Root mean square (RMS) roughness: 2.64 nm; (**b**) PiNT:BTP-eC9, RMS: 1.32 nm; (**c**) the surface height distributions of PNT:BTP-eC9 and PiNT:BTP-eC9 films.

9. 2D Grazing Incidence Small-Angle/Wide Angle X-ray Scattering (GISAXS/GIWAXS)

2D GISAXS/GIWAXS/measurement was performed on an XEUSS 3.0 UHR SAXS/WAXS system (XENOCS, France). A Eiger2 R 1M 2-dimensional detector with 0.075 mm × 0.075 mm active pixels was utilized in integration mode. The detector was positioned about 100/2000 mm downstream from the sample location. The precise sample-to-detector distance was determined with a silver behenate standard. The Cu incident X-ray (8 KeV) with a 0.9 mm×0.9 mm/0.5 mm×0.5 mm spot provided large enough q space. 1D GIWAXS patterns was corrected to represent real q_r and q_{xy} axes with the consideration of missing wedge. The critical incident angle was determined by the maximised scattering intensity from sample scattering with negligible contribution from underneath layer scattering. The shallow incident angle scattering was collected at 0.2°, which renders the incident X-ray as an evanescent wave along the top surface of thin films. The samples for GISAXS/GIWAXS test were prepared by casting solution onto silicon wafer substrates (ca. 15 mm×15 mm), and the active layers were prepared using exactly the same concentration and same procedures as those for device processing. For the polar plots, we extract the variety of scattering intensity within the changing of polar angle ω. Here the polar angle "ω" is the angle between the q vector and the q_z component in q-space. ω is out-of-plane near 0° and in-plane near plus or minus 90° .
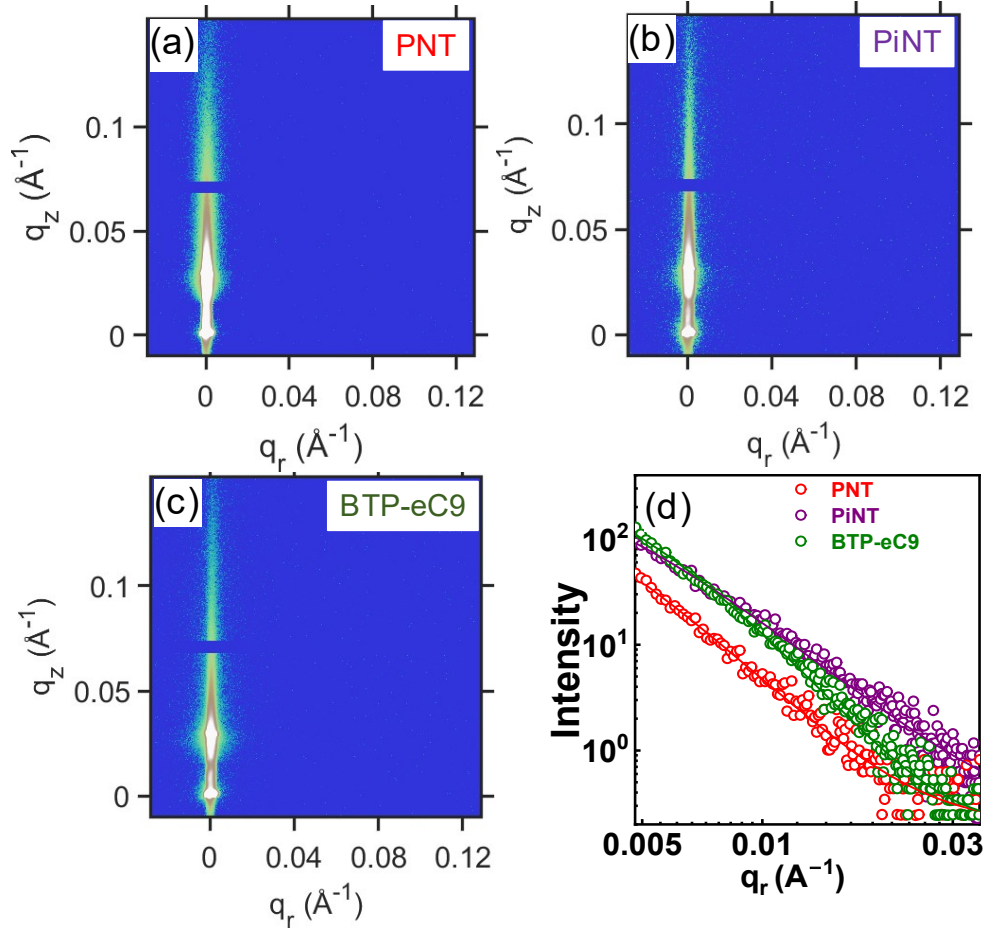
Fig. S22. The 2D-GISAXS patterns of (**a**) PNT, (**b**) PiNT, and (**c**) BTP-eC9 films; (**d**) the 1D-GISAXS line-cut profiles of PNT, PiNT, and BTP-eC9 films (the dash line were fitted curves).

Table S14. The domain properties of PNT, PiNT, and BTP-eC9 films from the fitted 1D-GISAXS line-cut curves.

Sample	η [nm]	D	2Rg [nm]
PNT	18.1	3.3	96.4
PiNT	19.2	2.85	89.9
BTP-eC9	19.3	3.10	97.3

Table S15. The domain properties of PNT:BTP-eC9, and PiNT:BTP-eC9 blend films from the fitted 1D-GISAXS line-cut curves.

Sample	ξ [nm]	η [nm]	D	2Rg [nm]

PNT:BTP-eC9	32.0	11	3	53.8
PiNT:BTP-eC9	18.2	6.8	3	33.3
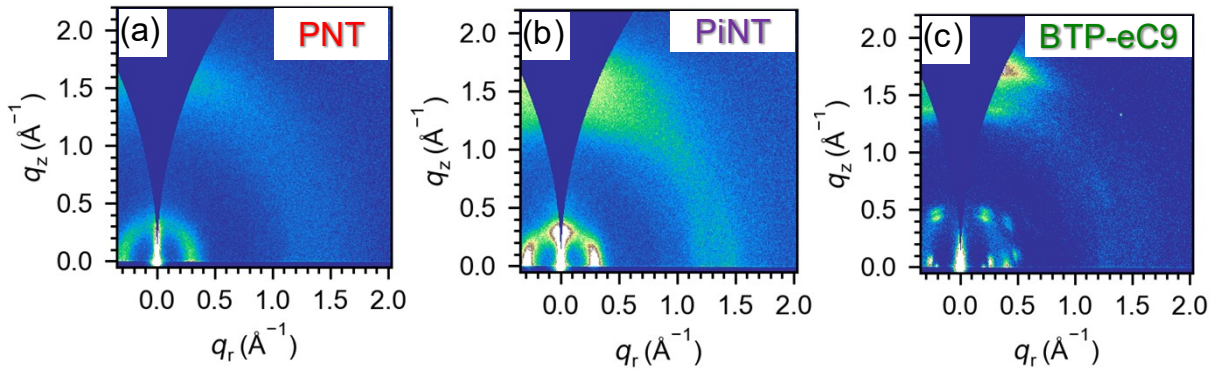
Fig. S23. 2D-GIWAXS patterns of (**a**) PNT, (**b**) PiNT, and (**c**) BTP-eC9 pure films.
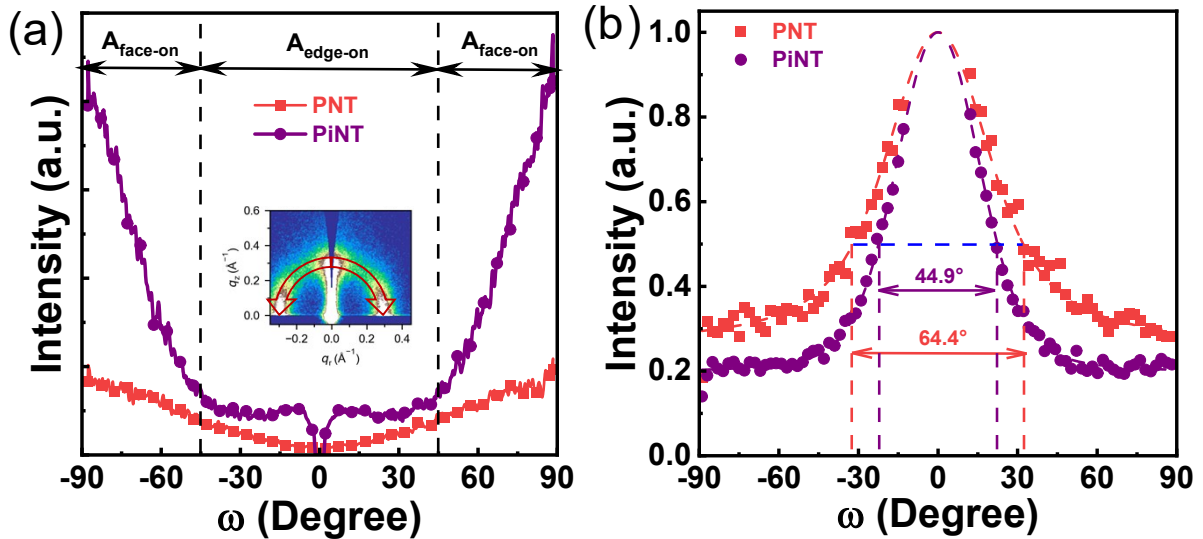
Fig. S24. (**a**) The pole plot with sin(ω) correlation extracted from the (100) diffraction of PNT, and PiNT pure films; (**b**) the azimuthal intensity plot of (010) peak of PNT, and PiNT films.

Table S16. GIWAXS parameters of the related PNT, and PiNT neat films in IP direction.

Sample	IP (100)			
	q [Å^{-1}]	d-spacing [Å]	FWHM [Å^{-1}]	CCL [Å]
PNT	0.298	21.074	0.127	44.504
PiNT	0.293	21.433	0.077	73.404

Table S17. GIWAXS parameters of the related PNT:BTP-eC9, and PiNT:BTP-eC9 blend films in IP direction.

Sample	IP (100)			
	q [Å^{-1}]	d-spacing [Å]	FWHM [Å^{-1}]	CCL [Å]
PNT:BTP-eC9	0.312	20.128	0.180	31.400
PiNT:BTP-eC9	0.296	21.216	0.090	62.870

Table S18. GIWAXS parameters of PNT, PiNT, and BTP-eC9 neat films in OOP direction

Sample	OOP (010)			
	q [Å^{-1}]	d-spacing [Å]	FWHM [Å^{-1}]	CCL [Å]
PNT	1.571	3.997	0.329	17.179
PiNT	1.596	3.935	0.280	20.186
BTP-eC9	1.730	3.630	—	—

Table S19. GIWAXS parameters of PNT:BTP-eC9, and PiNT:BTP-eC9 blend films in OOP direction

Sample	OOP (010)			
	q [Å^{-1}]	d-spacing [Å]	FWHM [Å^{-1}]	CCL [Å]
PNT:BTP-eC9	1.681	3.736	0.498	11.349
PiNT:BTP-eC9	1.702	3.690	0.466	12.129

Table S20. The calculative face-on/edge-on ratios of PNT, PiNT, PNT:BTP-eC9 and PiNT::BTP-eC9 films.

Sample	PNT	PiNT	PNT:BTP-eC9	PiNT:BTP-eC9
A_Z/A_r	3.17	4.59	3.22	5.24

10. Photoluminescent (PL) Spectra and Photoluminescence Quantum Yield

Photoluminescence (PL) quenching experiments were conducted to investigate photoinduced charge transfer processes at the donor/acceptor interfaces. Data were collected using the HORiBA FLUOROMAX-4 fluorimeter. The PL excitation wavelengths were set to 600 nm for PNT and PNT:BTP-eC9 films and 550 nm for PiNT and PiNT:BTP-eC9 films for exciting donor and 780 nm for BTP-eC9, PNT:BTP-eC9, and PiNT:BTP-eC9 films for exciting acceptor. The absolute photoluminescence quantum yields (PLQYs) of PNT, PiNT, and other polymer pure films were measured using a Hamamatsu C11347 Quantaurus-QY spectrometer. The thin films were prepared by spin-coating polymeric CF solution onto 0.5 cm × 0.5 cm quartz substrates.
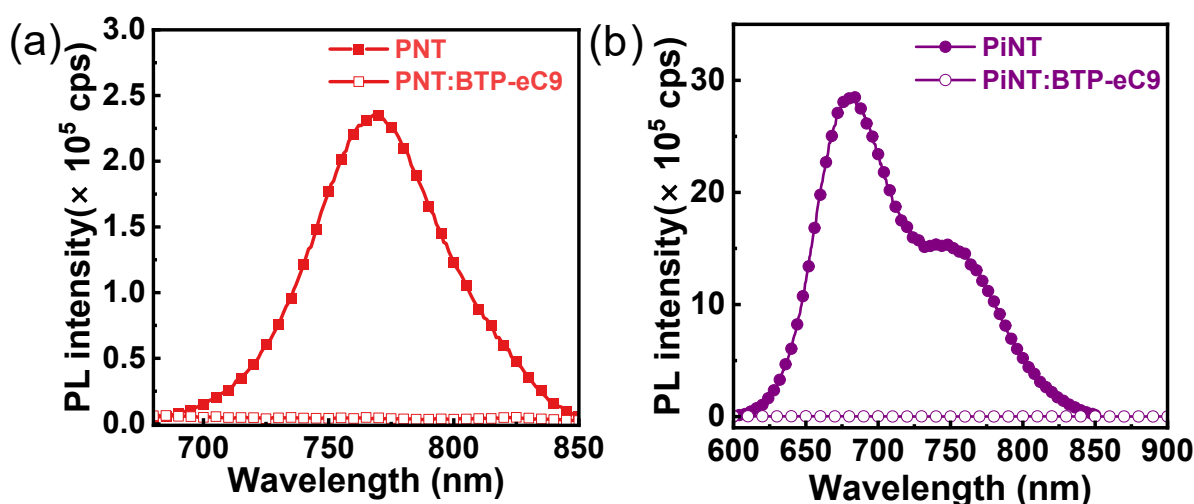
Fig. S25. PL spectra of (**a**) PNT, and PNT:BTP-eC9 films and (**b**) PiNT, and PiNT:BTP-eC9 films.
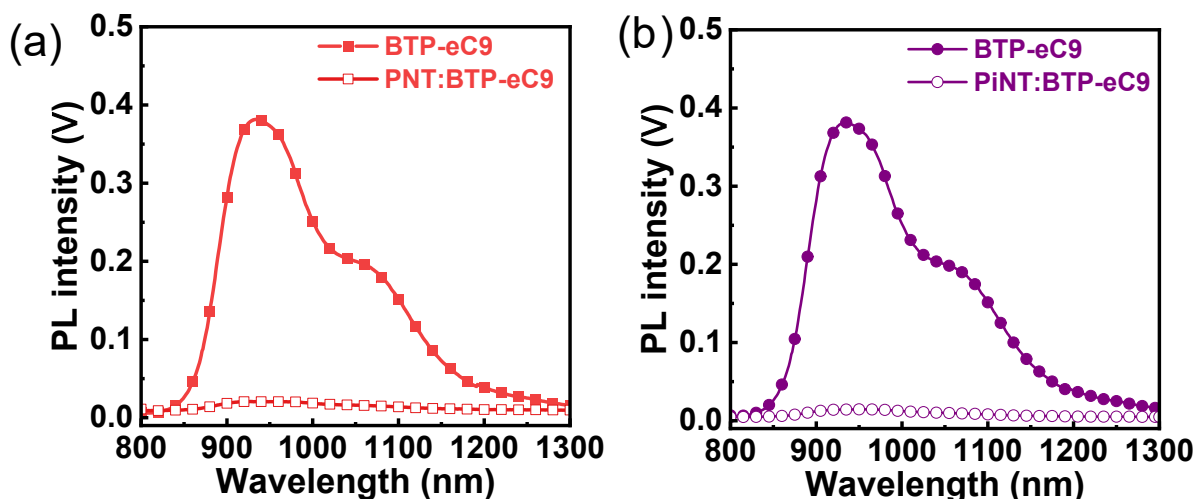
Fig. S26. PL spectra of (**a**) BTP-eC9, and PNT:BTP-eC9 films and (**b**) BTP-eC9, and PiNT:BTP-eC9 films.
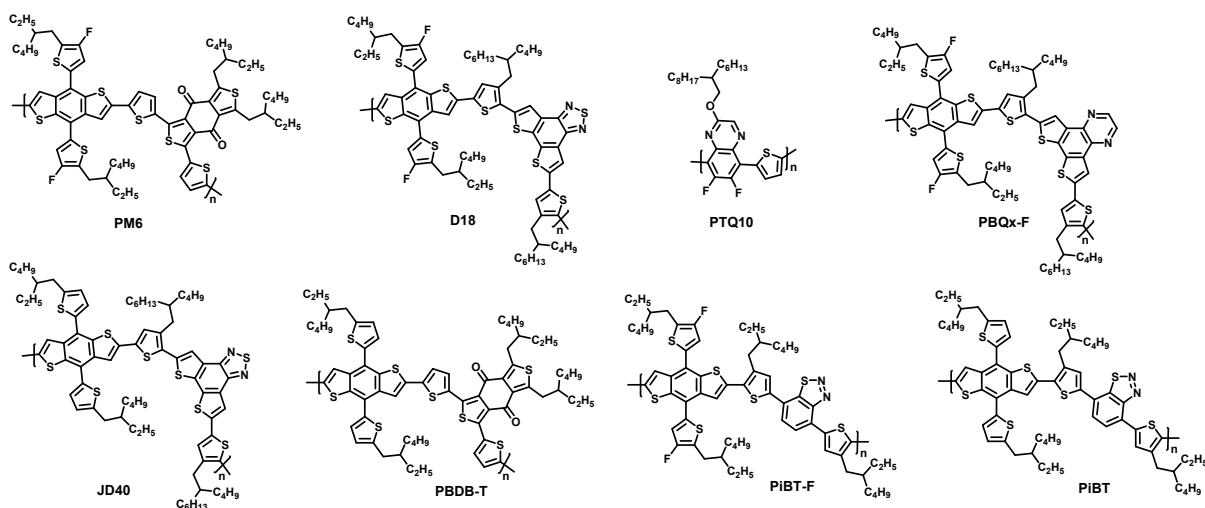
Fig. S27. The chemical structures of donor polymers for PLQY tests.
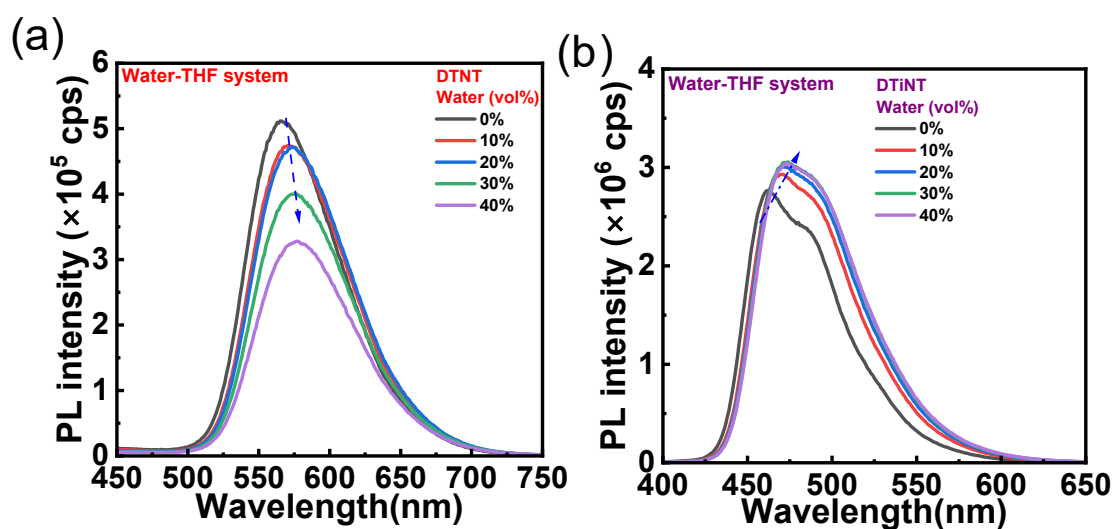
11. Fabrication and Characterization of SCLC Devices

The charge carrier mobilities of pristine and blend films are estimated from space-charge-limited current (SCLC) method. The hole-only and electron-only devices were fabricated with the architectures of ITO/PEDOT:PSS/Active layer/MoO$_3$/Ag and ITO/ZnO/Active layer/PFNDIT-F3N/Ag. Hole-only and electron-only devices were recorded with a Keithley 236 source meter under dark. The hole and electron mobilities were determined by fitting the dark current to the model of single-carrier SCLC, which is described by the equation,

$$J = \frac{9}{8}\varepsilon_0 \varepsilon_\gamma \mu \frac{V^2}{d^3}$$

where J is the current density, μ is the zero-field mobility, ε_0 is the permittivity of free space, ε_r is the relative permittivity of the material, d is the thickness of the active layers, and V is the effective voltage. The effective voltage was obtained by subtracting the built-in voltage (V_{bi}) and the voltage drop (V_s) from the series resistance of the whole device except for the active layers from the applied voltage (V_{appl}), $V = V_{appl} - V_{bi} - V_s$. ($V_{bi} = 0$ and $V_s = 10 \times I$, where the value 10 is the resistance of MoO$_3$ and I is the current of the devices in this work). The hole and electron mobilities can be calculated from the slope of the $J^{1/2}$-V curves.
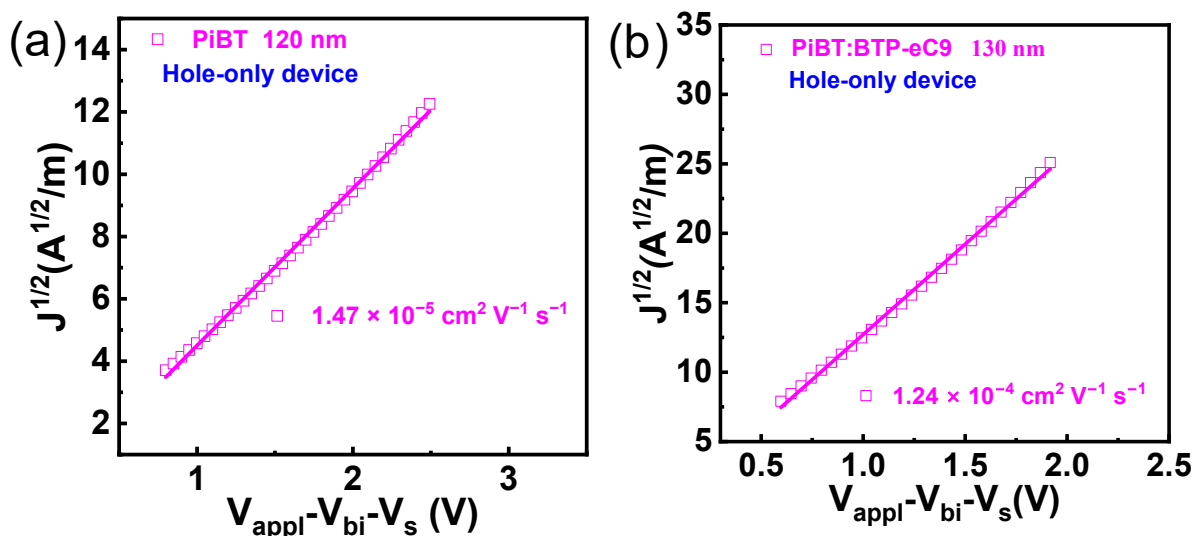
Fig. S29. SCLC plots of the hole-only devices: (**a**) pristine PiBT film, (**b**) PiBT:BTP-eC9 blend film. The experimental data are fitted using the SCLC model (solid lines).
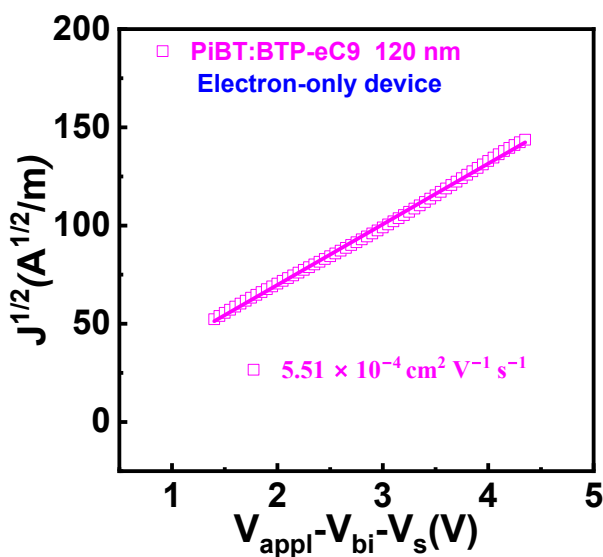
Fig. S30. SCLC plots of the electron-only devices of PiBT:BTP-eC9 blend film. The experimental data are fitted using the SCLC model (solid lines).
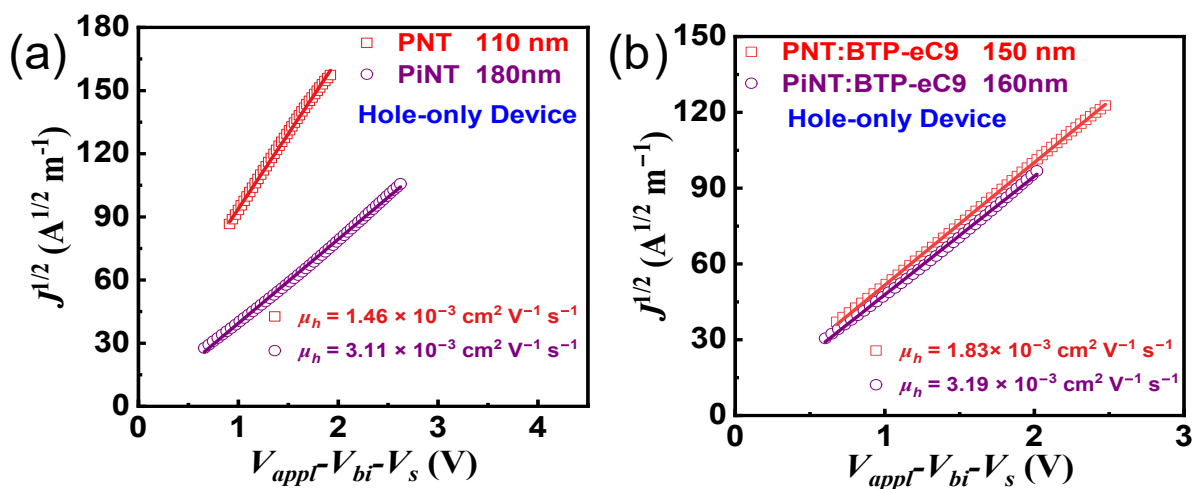
Fig. S31. SCLC plots of the hole-only devices: (**a**) pristine PNT and PiNT films, (**b**) PNT:BTP-eC9 and PiNT:BTP-eC9 blend films. The experimental data are fitted using the SCLC model (solid lines).
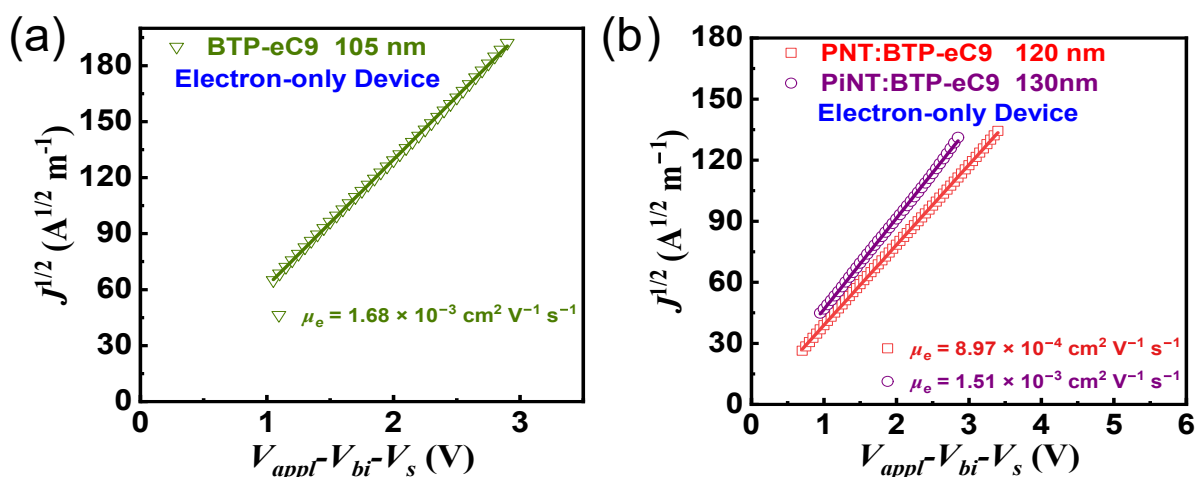
Fig. S32. SCLC plots of the electron-only devices of (**a**) BTP-eC9, (**b**) PNT:BTP-eC9, and PiNT:BTP-eC9 films. The experimental data are fitted using the SCLC model (solid lines).

12. Energy Loss Measurements

The energy loss data were obtained by measuring the optimal OSC devices after encapsulation. The electroluminescence spectra were acquired by a high-sensitivity spectrometer (QE Pro, Ocean Optics), while the external quantum efficiency of EL was determined by measuring the emitted photons in all directions through an integrated sphere by using a calibrated spectrometer (QE Pro, Ocean Optics), with the device injected by an external current/voltage source with constant current density.
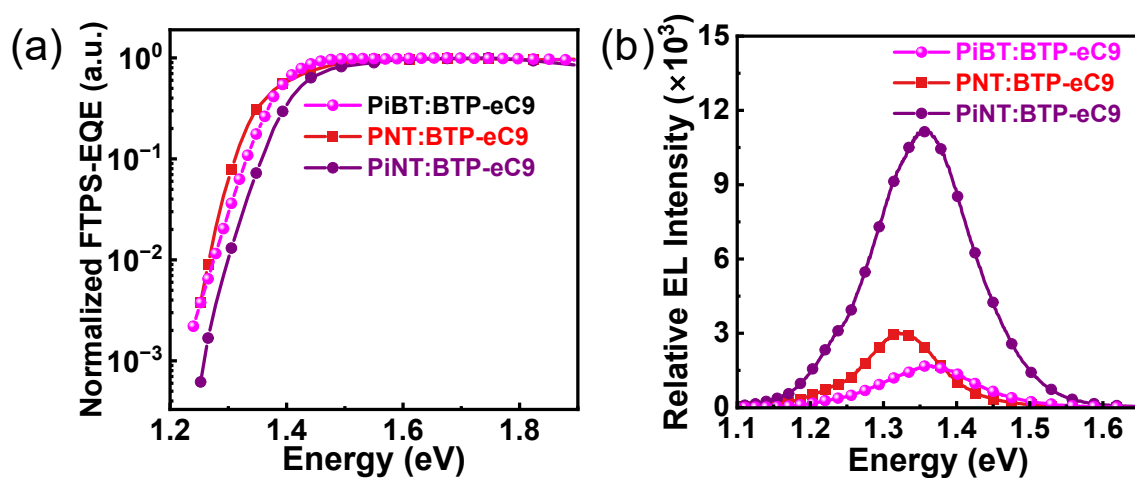
Fig. S33. (**a**) FTPS-EQE spectra and (**b**) EQE_{EL} spectra.

Table S21. Detailed energy losses of the related OSCs.

Devices	E_g [eV]	qVoc^{SQ} [eV]	qV_{OC}^{rad} [eV]	E_{loss} [eV]	ΔE_1 [eV]	ΔE_2 [eV]	ΔE_3 [eV]	q$V_{OC}^{Cal.}$ [eV]
PiBT:BTP-eC9	1.42	1.15	1.07	0.70	0.27	0.09	0.34	0.72
PNT:BTP-eC9	1.41	1.14	1.06	0.62	0.27	0.08	0.27	0.79
PiNT:BTP-eC9	1.42	1.16	1.08	0.54	0.26	0.08	0.20	0.88

13. Ultra-fast Transient Absorption Spectroscopy (TAS) Measurements

TAS measurement (VIS, 800 nm excitation) was discussed elsewhere. A 50% of the output of a 1 kHz, 1W, 100 fs Ti:sapphire laser system with a 827 nm fundamental (Tsunami oscillator/Spitfire amplifier, Spectra-Physics LLC) was used to pump a commercial collinear optical parametric amplifier (TOPAS-Prime, Light-Conversion LLC) tuned to 800 nm. The pump was depolarized to suppress effects due to polarization-dependent dynamics and attenuated to the specific energy density. The pump was focused to a 1 mm diameter spot at the sample position. The probe was generated using 10% of the remaining output to drive continuum generation in a proprietary crystal and detected on a commercial spectrometer (customized Helios, Ultrafast Systems LLC). Data processing was performed using commercial software (Surface Xplorer, Ultrafast Systems LLC). The pump beam size was larger than the probe beam to ensure uniform excitation and detection. A fluence of 2.6 μJ/cm² was used to excite the samples and to discourage higher-order exciton and polaron annihilation processes (such as exciton-exciton annihilation and Auger recombination), which might introduce unexpected recombination features.

TAS measurement (NIR and VIS, 400 nm excitation) was conducted via a home-built pump probe setup. A Ti:Sapphire regenerative amplifier (Coherent Legend Elite, 1000 Hz) is seeded by a Ti:Sapphire femtosecond oscillator (Coherent Mira 900; <120 fs pulse width, 76 MHz repetition rate, 800 nm central wavelength). The output of the amplifier is split into an optical parametric amplifier (Coherent Opera Solo) which provides the pump beam with

tunable photon energy, while the other beam is directed onto a retroflector mounted on mechanical delay stage and subsequently focused on an yttrium aluminium garnet (YAG) plate to generate a supercontinuum probe. The pump beam is chopped at 500 Hz and incident at a small angle on the sample with a spot diameter of ~ 1.5 mm. The probe beam at a 1000 Hz repetition rate is focused onto the sample and aligned to ensure good overlap with the pump beam. Shot-by-shot transmission of the probe beam in the range of 400 – 900 nm is collected by achromatic lenses analyzed in a spectrometer (Acton Spectrapro 275) equipped with a 150 ln/mm grating and a line CCD triggered by the chopper. The near-infrared range (800 ~ 1600 nm) of probe beam is analyzed via a spectrometer (Acton SpectraPro 300i) equipped with a 50 ln/mm grating. $\Delta T/T$ is determined by calculating the full spectrum difference in transmission of the probe pulse between pump-on and -off. The chirp of the system is corrected in software. The incident power is measured with a calibrated laser power meter. The pump beam size was larger than the probe beam to ensure uniform excitation and detection. A fluence of 3.1 µJ/cm² was used to excite the sample and to discourage higher-order exciton and polaron annihilation processes (such as exciton-exciton annihilation and Auger recombination), which might introduce unexpected recombination features.

Additional discussion: The 400 nm wavelength laser was chosen for exciting the donor in both the neat donor film and the blend film to monitor the dynamic of donor.. Additionally, in the blend film, the 400 nm excitation allowed probing the photoinduced electron transfer from the donor to the acceptor, and potentially, the occurrence of back-hole transfer from the acceptor to the donor. The 800 nm wavelength laser was used to excite the acceptor (BTP-eC9) in both neat acceptor film and blend films for probing the transition of photoinduced hole transfer dynamic from acceptor to donor. The visible- and NIR-TAS plots at various selected time ranges revealed distinct photoinduced features (see Fig. 7a-b and S34-S41). Within the visible detection range, the peaks observed at 520 ~ 660 nm in the PiNT film (see Fig. S34b) and 560 ~ 720 nm in the PNT film (see Fig. S35b) are ascribed to the GSB signal of photoinduced singlet excitons originating from the donor. The peaks spanning from 600 nm to 780 nm and from 825 nm to 890 nm are attributed to the combinations of GSB and stimulated emission (SE) signals generating from singlet exciton of the acceptor.(see Fig. S36 and S37b-c). Besides, in NIR detection range, the signal observed in the range from 900 nm to 1150 nm

was attributed to the contribution of PIA signal of acceptor (see Fig. S37c), whereas the signal across nearly the entire NIR range corresponds to the PIA of the donor (see Fig. S34c and S35c). Notably, the acceptor triplet PIA may lie in the range from 1400 nm to 1600 nm.

In blend films, when exciting the acceptor with an 800 nm laser, the signals from both photogenerated singlet excitons and the GSB signals of electron polarons overlap with each other (see Fig. 7a and S39b). This overlapping makes it challenging to analyze the kinetics of pure electron polarons in this range. Therefore, the hole polaron, as counterpart of electron polaron, are utilized to understand the polaron feature. The signal in the 600 ~ 615 nm range was extracted to track the dynamic of hole polarons (see Fig. 7c) because this specific range was less interfered by both the GSB and PIA signals of acceptor that ranged from 450 nm to 600 nm TAS spectra (see Fig. S37c). Empirically, the rising process in kinetic of hole polarons intuitively reflects the polaron generation, while the subsequently decay process represents the polaron (or charge) recombination process. The upward trend of singlet excitons indicates the generation of excitons, while the subsequent decline reflects the dissociation of excitons (see Fig. S42a). The concordance between the decay process of exciton dissociation and the polaron generation in both PNT:BTP-eC9 and PiNT:BTP-eC9 films suggests that the hole polarons generated from exciton dissociation undergo transfer to the donor materials. In the NIR region, the detection range from 1100 nm to 1150 nm can be primarily ascribed to the prevalence of donor hole polarons since the absence of exciton signal at the range. As a result, the hole polaron kinetic in the 1100 ~ 1150 nm range, corresponding to the PIA signal of the donor, has been extracted (see Fig. S37c, S38c, and S41b). The results exhibit a similar trend (see Fig. 8d) to the earlier studies on hole polaron kinetics. The congruent evolution observed in both hole polaron kinetics validates that the charge (polaron) transfer followed by charge recombination indeed occurred after exciton formation. Moreover, when the donors were excited with a 400 nm laser in both neat and blend films, the wavelength in the range of 600 nm to 615 nm was extracted to isolate the pure donor features (see Fig. S42b). For analyses, the 400 nm laser was also employed to excite the acceptor at the same time scale of exciting the donor (see Fig. S36, S39, and S40). Our results revealed the occurrences of both electron transfer and hole transfer at the interface, from donor to acceptor and vice versa.Notably, here 600~615 nm can be used to track both exciton and polaron since the excited acceptor can initiate hole transfer to the

donor, subsequently causing the rise in the polaron signal during 400 nm excitation. (see Fig. S42b, S43a, and S43b). As discussed in the main text, the energy transfer is more pronounced in PiNT:BTP-eC9 system. So we fitted the lifetime of the ultrafast decay, and obtained the values of 215 fs for PIA signal and 226 fs for GSB signal (see Fig. S43a). We observed that the rising of acceptor GSB signal for PiNT:BTP-eC9 is faster than that of PNT:BTP-eC9. This observation aligns with the ultrafast energy transfer from donor to acceptor in the PiNT:BTP-eC9 system. Furthermore, the analysis of acceptor GSB signal reveals that the decay lifetime in the PNT:BTP-eC9 blend is longer than that in PiNT:BTP-eC9 (see Fig. 43c). This difference suggests that the generation of electron polarons is more pronounced in the PNT system, supporting our hypothesis that in the PNT system, electron transfer dominates, while in the PiNT system, FRET is more evident. The PIA signal of PNT under 400 nm excitation did not correlate with the GSB signal observed under 800 nm excitation. This result suggests that the hole transfer process in PNT:BTP-eC9 is not evident. Moreover, it implies that the energy transfer process in PNT:BTP-eC9 may be weaker compared with PiNT:BTP-eC9 (see Fig. 44a-b).
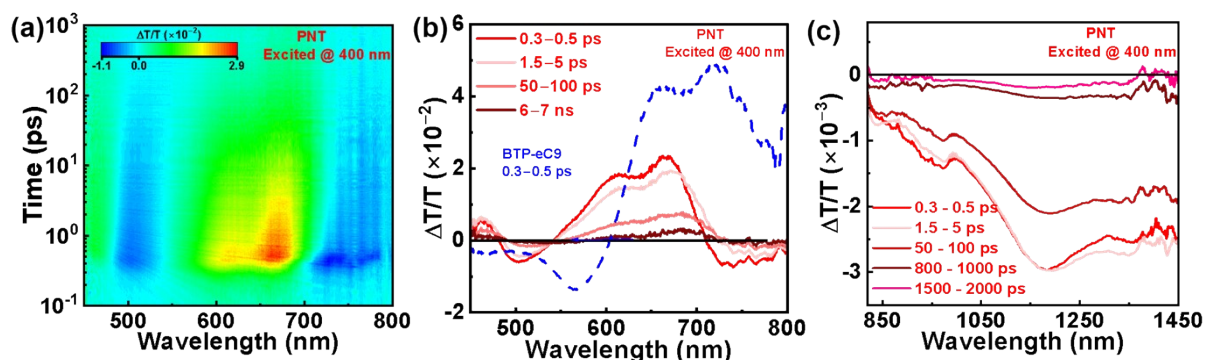
Fig. S34. (**a**) Femtosecond-resolved TA signals recorded from PNT pure film; (**b**) the femtosecond-resolved TA spectra from PNT pure film at different delay times; (**c**) the NIR-femtosecond-resolved TA dynamic curves recorded from the neat PNT film.
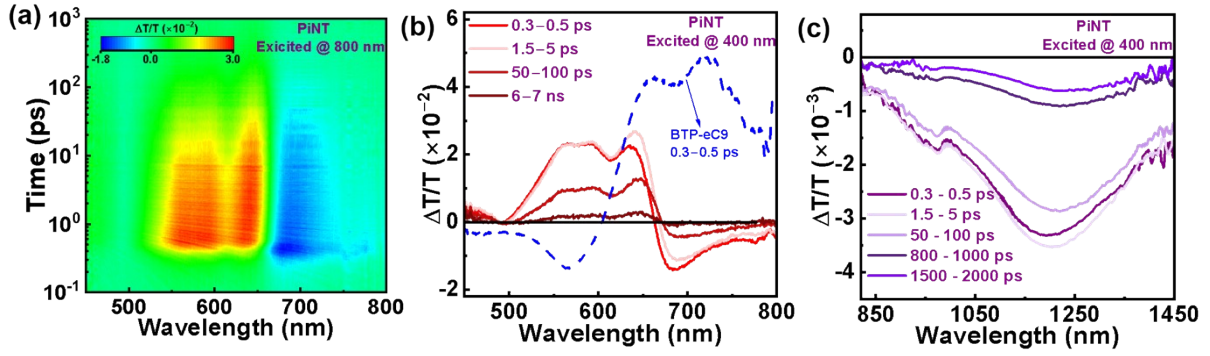
Fig. S35. (**a**) Femtosecond-resolved TA signals recorded from PiNT pure film; (**b**) the femtosecond-resolved TA spectra from PiNT pure film at different delay times; (**c**) the NIR-femtosecond-resolved TA dynamic curves recorded from the neat PiNT film.
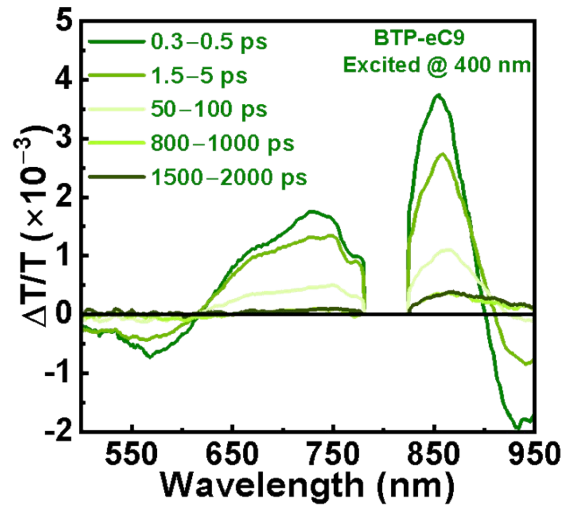
Fig. S36. Femtosecond-resolved TA spectra from BTP-eC9 pure films at different delay times.
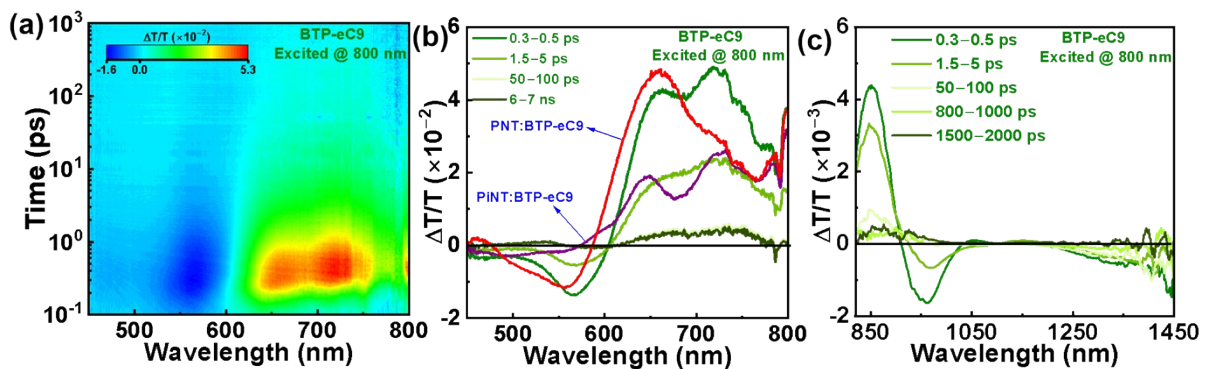
Fig. S37. (**a**) Femtosecond-resolved TA signals recorded from BTP-eC9 pure film; (**b**) the femtosecond-resolved TA spectra from BTP-eC9 pure film at different delay times; (**c**) the NIR-femtosecond-resolved TA dynamic curves recorded from the neat BTP-eC9 film.
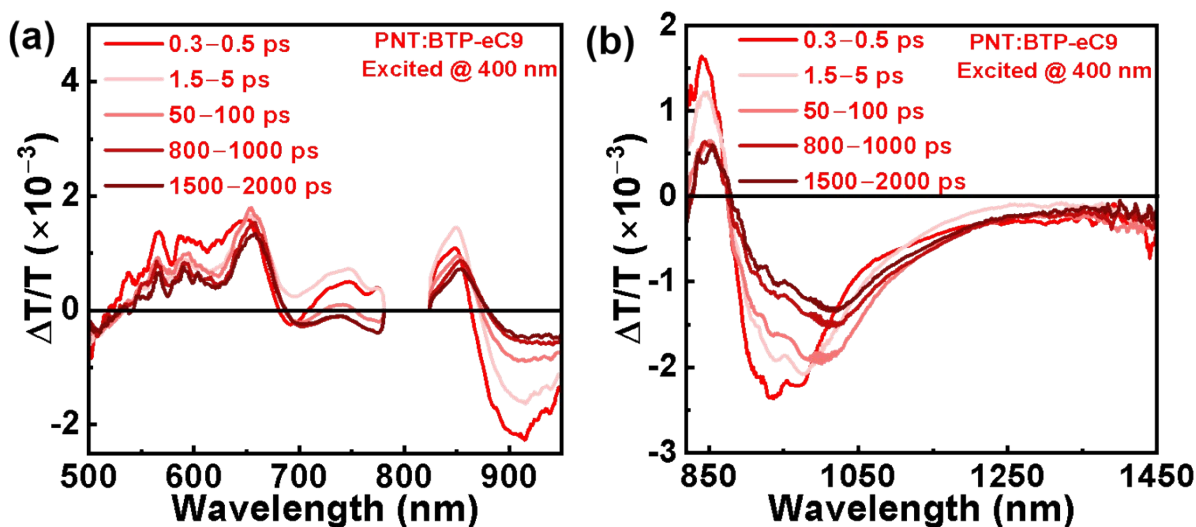
Fig. S38. (**a**) Femtosecond-resolved TA spectra from PNT:BTP-eC9 blend film at different delay times; (**b**) the NIR-femtosecond-resolved TA dynamic curves recorded from PNT:BTP-eC9 blend film.
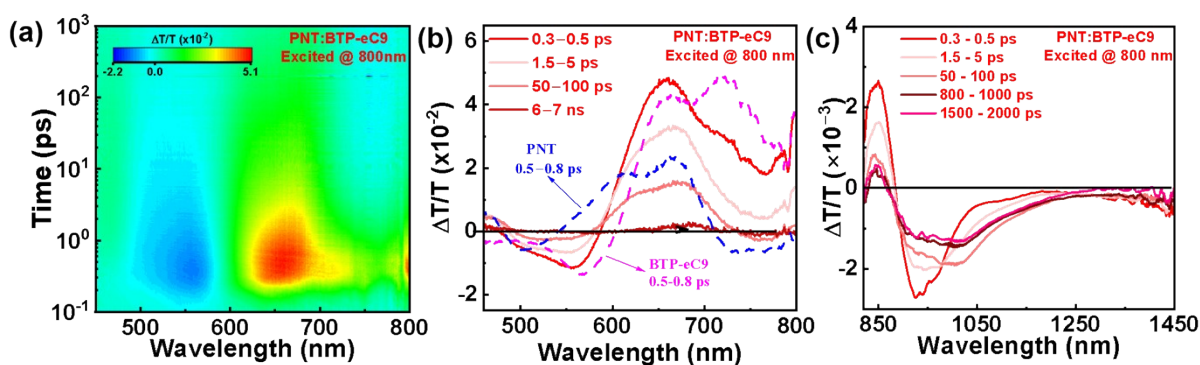
Fig. S39. (**a**) Femtosecond-resolved TA signals recorded from PNT:BTP-eC9 blend film; (**b**) the femtosecond-resolved TA spectra from PNT:BTP-eC9 blend film at different delay times; (**c**) the NIR-femtosecond-resolved TA dynamic curves recorded from PNT:BTP-eC9 blend film.
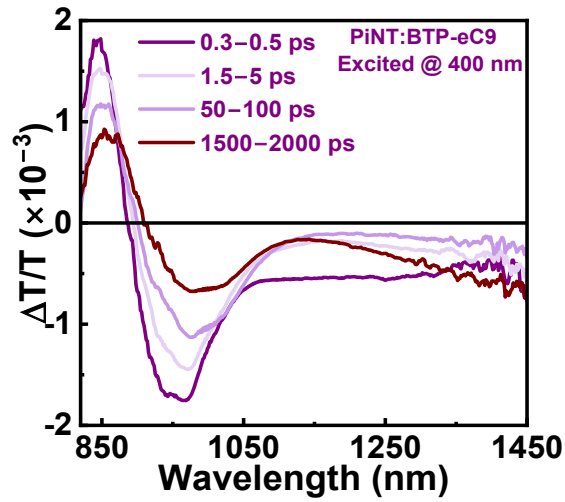
Fig. S40. NIR-femtosecond-resolved TA dynamic curves recorded from PiNT:BTP-eC9 blend film.
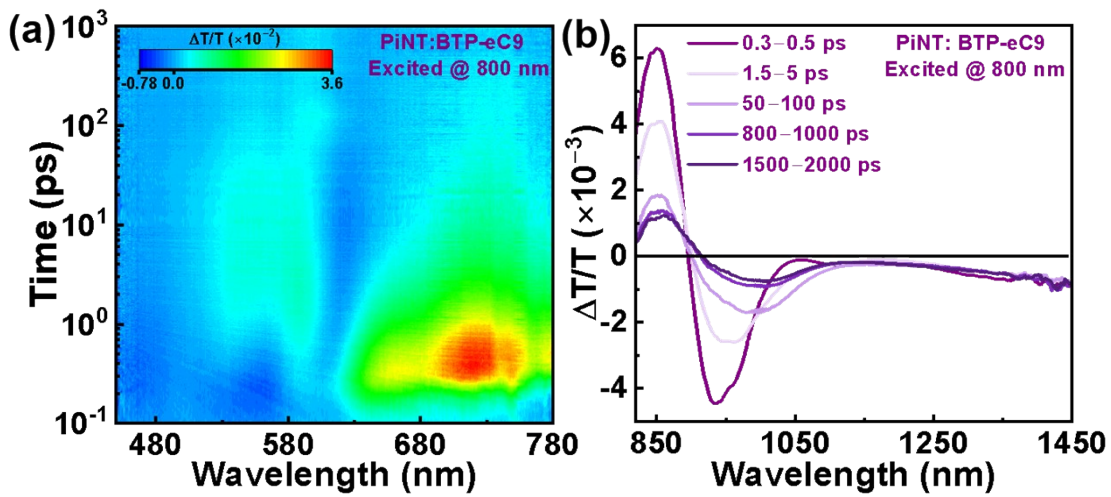
Fig. S41. (**a**) Femtosecond-resolved TA signals recorded from PiNT:BTP-eC9 blend film ; (**c**) the NIR-femtosecond-resolved TA dynamic curves recorded from PiNT:BTP-eC9 blend film.
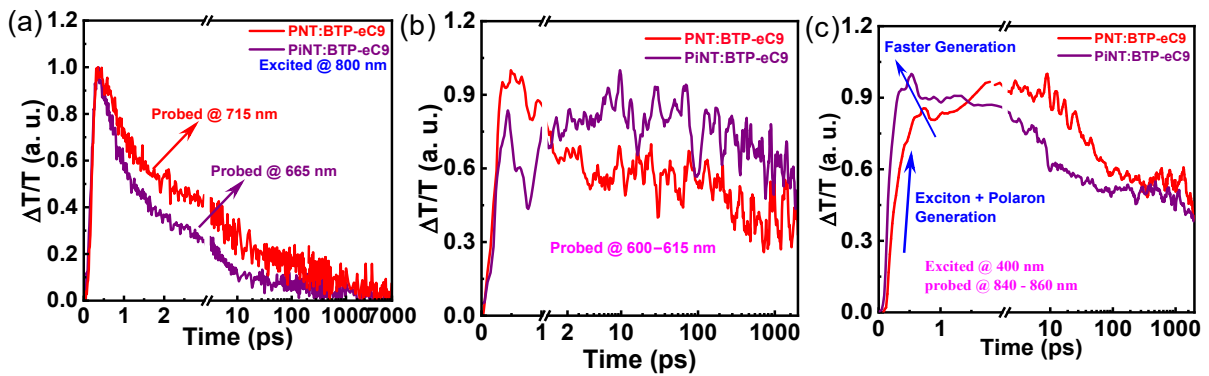
Fig. S42. (**a**) Femtosecond-resolved TAS kinetic dynamic curves probed at 715 nm for PNT:BTP-eC9 and 665 nm for PiNT:BTP-eC9; (**b**) the femtosecond-resolved TA dynamic curves probed at 600-615 nm recorded from PNT:BTP-eC9 and PiNT:BTP-eC9 blend films excited at 400 nm; (**c**) the femtosecond-resolved TA dynamic curves probed at 840-860 nm recorded from PNT:BTP-eC9 and PiNT:BTP-eC9 blend films.
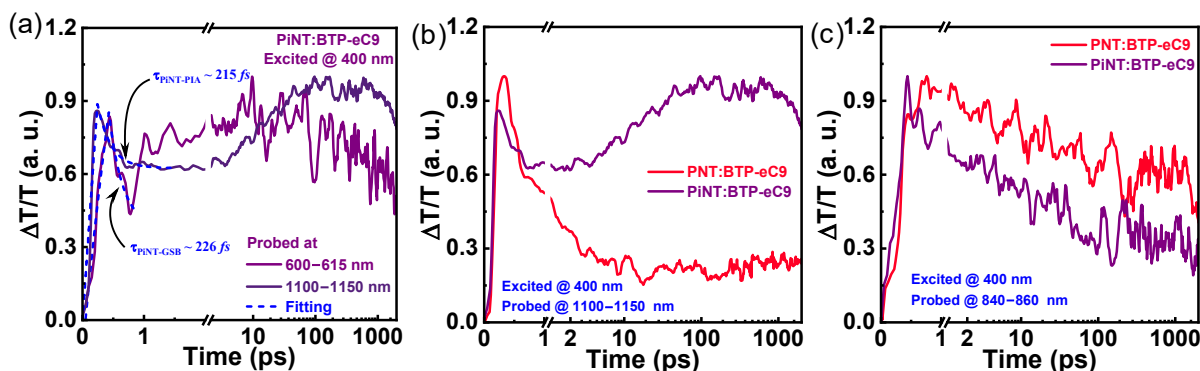
Fig. S43. (**a**) The TAS kinetic curves comparisons of GSB (600~615 nm) and PIA (1100~1150 nm) signals for donor in PiNT:BTP-eC9 films; (**b**) the comparison of PIA signals (1100-1150 nm) for donor in PNT:BTP-eC9 and PiNT:BTP-eC9 films; (**c**) the comparison of GSB (840 - 860 nm) signals for acceptor in PNT:BTP-eC9 and PiNT:BTP-eC9 films.
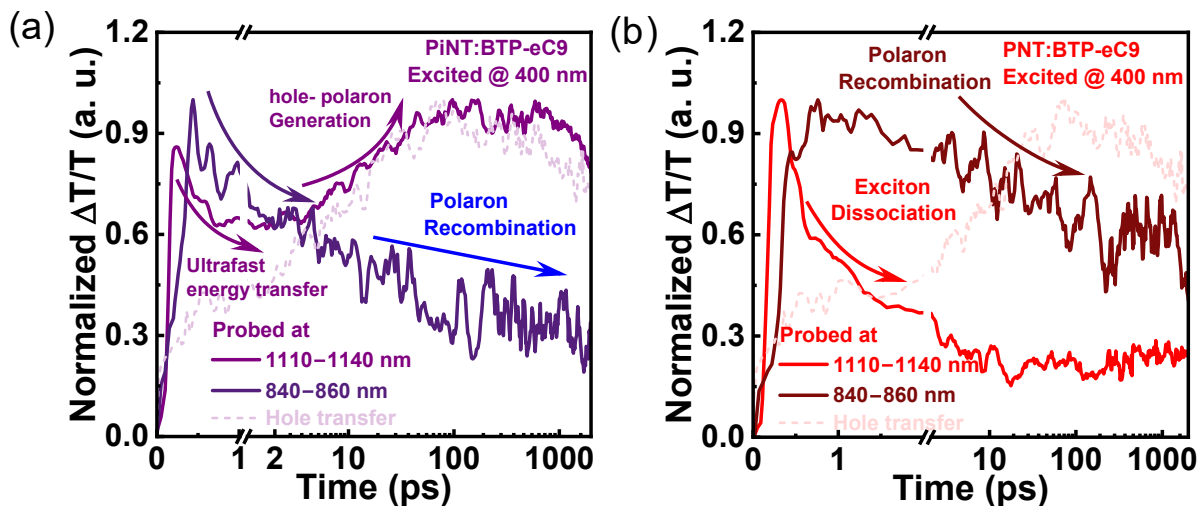
Fig. S44. The TAS kinetic curves of normalized GSB of acceptor, PIA of donor, and hole transfer polaron (GSB of donor) under 800 nm excitation for (**a**) PiNT:BTP-eC9 and (**b**) PNT:BTP-eC9 films.

48
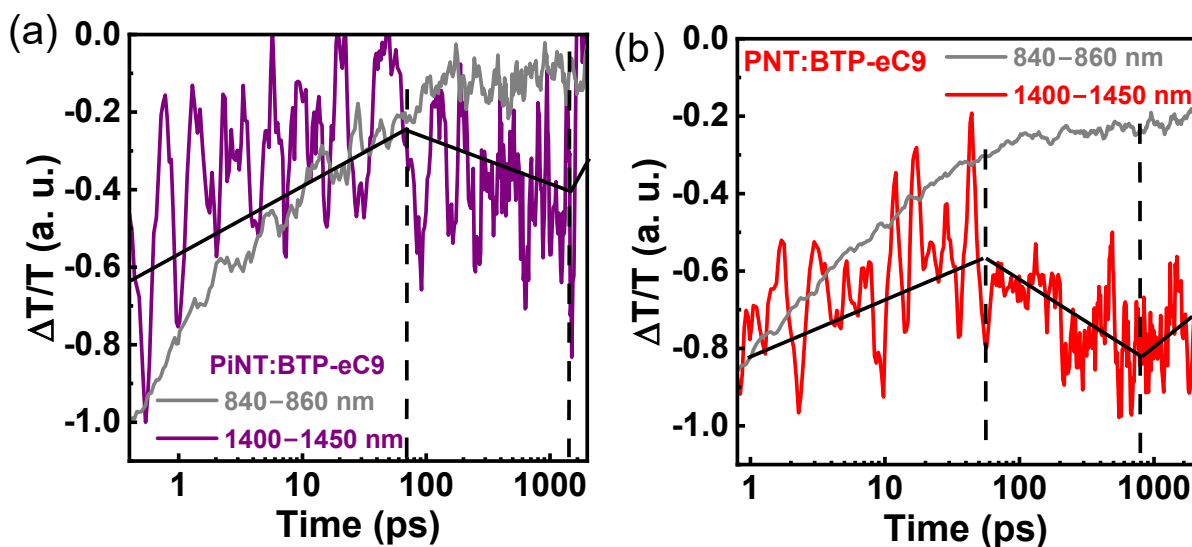
Fig. S45. The triplet formation or inter-CT generation in NIR range (1400~1450 nm) for (**a**) PiNT:BTP-eC9, and (**b**) PNT:BTP-eC9 films (The gray line is the GSB signal of BTP-eC9 acceptor).

14. Time-resolved Photoluminescence (TRPL) Measurements

Photoluminescence measurement was carried out on a home-built setup. Output light from a pulse diode (Edinburg Instrument; ~ 50 ps pulse width, 10 MHz repetition rate, 640 nm central wavelength) was focused on the sample with a 150-mm lens (spot size ~ 200 μm). PL signals are collected with a two-lens system and detected using an optical fiber positioned at the focus of lens. The visible spectra (400 ~ 800 nm) are recorded by an Acton instruments SR-500i spectrometer equipped with a 150 line/mm grating and a cooled charge-coupled device (CCD, Andor Newton EM), while the NIR spectra (800 ~ 1600 nm) are recorded via Acton SpectraPro 275 spectrometer with a 150 line/mm grating cooled electcally by InGaAs detector (Hamamatsu C8061-01). The time-resolved PL in the visible range was measured by a single photon counter (Becker and Hickl PMC-100) equipped on the spectrometer (Acton SpectraPro 275).
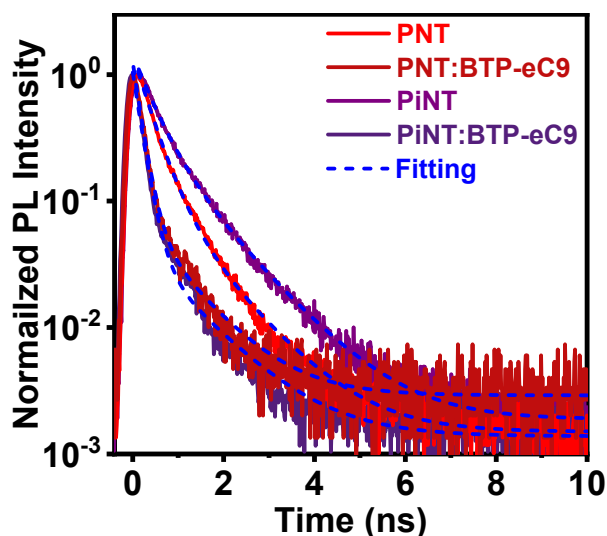
Fig. S46. Time-resolved photoluminescence (TRPL) curves of PNT (probed at 730 nm), PiNT (probed at 685 nm), PNT:BTP-eC9 (probed at 730 nm), and PiNT:BTP-eC9 (probed at 685 nm) films.

Table S22. Detailed exciton lifetime of the PNT, PiNT, PNT:BTP-eC9, and PiNT:BTP-eC9 films.

Materials	τ_1 [ns]	τ_2 [ns]	τ_{avg} [ns]
PNT	0.344	1.051	0.538
PiNT	0.401	1.092	0.812
PNT:BTP-eC9	0.181	1.128	0.387
PiNT:BTP-eC9	0.173	0.971	0.381

15. Energy Transfer Calculations

To elucidate the role of energy transfer, we calculated the FRET efficiency using the following equation (1) [14]:

$$\eta_{FRET} = 1 - \frac{\tau_{DA}}{\tau_D} \tag{1}$$

Where τ_D and τ_{DA} represent the lifetime values of the neat donor and the corresponding blend films in TRPL measurement (see Table S22), respectively. Moreover, the FRET radius (R_0)

and FRET rate (K_{FRET}) can be also calculated. The former one (R_0) is normally determined by the spectra overlap between donor emission, and the acceptor absorption, and can be approximately calculated using the following equation (2) [15] when statistical orientation factor (k^2) was set to $\frac{2}{3}$:

$$R_0 = 0.0211(0.667\varphi_{PL}J)^{\frac{1}{6}}$$ (2)

Where here φ_{PL} is the fluorescence quantum yield of neat donor, and J can be calculated by following equation (3) [14]:

$$J = \frac{\int_0^\infty F_D(\lambda)\varepsilon_A(\lambda)\lambda^4 d\lambda}{n(\lambda)^4}$$ (3)

Where $F_D(\lambda)$ is the normalized fluorescence intensity of donor, $\varepsilon_A(\lambda)$ is the molar extinction coefficient of acceptor, and $n(\lambda)$ is the refractive index showed in Fig. S47.

Furthermore, the FRET rate (K_{FRET}) can be calculated by the following equation (4) [15]:

$$K_{FRET} = \frac{1}{\tau}(\frac{R_0}{R_{DA}})^6$$ (4)

The η_{ET} was calculated according to the approximate formula: $\eta_{FRET} + \eta_{ET} = 1$, as LUMO offsets for both PNT:BTP-eC9 and PiNT:BTP-eC9 were larger than $0.3\ eV$ and can provide sufficient RT driving force.
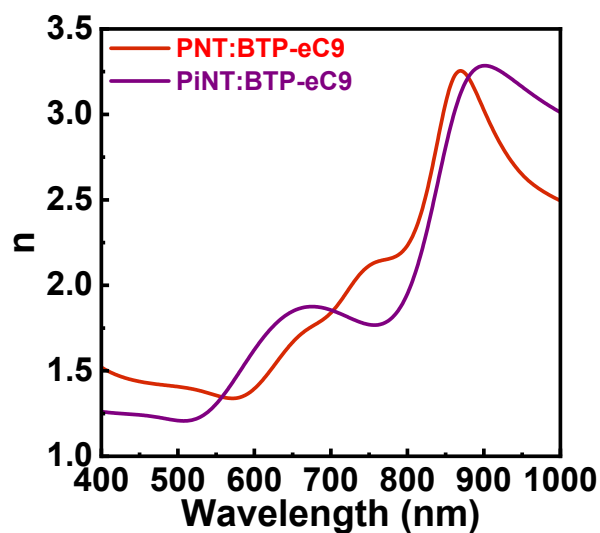
Fig. S47. Refractive index curves of PNT:BTP-eC9 and PiNT:BTP-eC9 films.

16. Solution NMR and Mass Spectra

The ^{1}H NMR and ^{13}C NMR spectra were measured on a Bruker AVANCE NEO (600 MHz) or Bruker AvanceIII HD (500MHz) spectrometer with tetramethylsilane (TMS) as the internal reference at room temperature or 135 ^{o}C (high temperature NMR test). Mass spectra were measured on Bruker ultrafleXtreme or Bruker tims-TOF instrument.
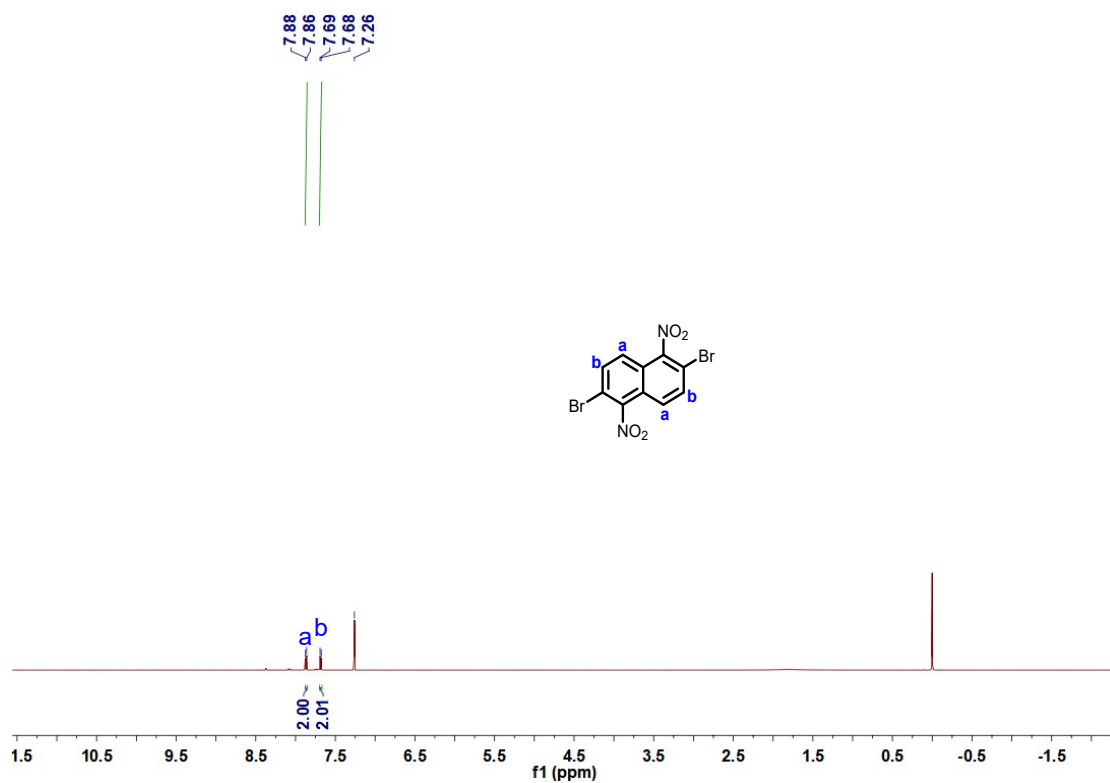
Fig. S48. The ^{1}H NMR spectrum of compound **2** in CDCl$_3$ at room temperature.
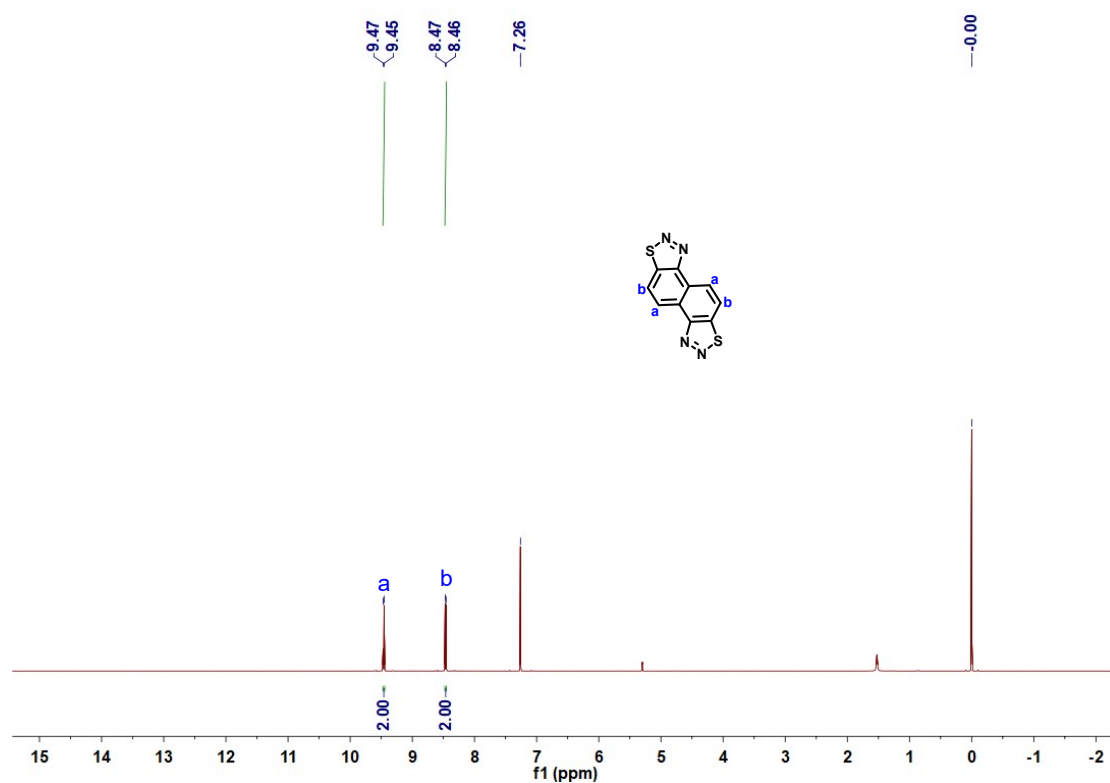
Fig. S49. The ^{1}H NMR spectrum of compound **4** in CDCl$_3$ at room temperature.
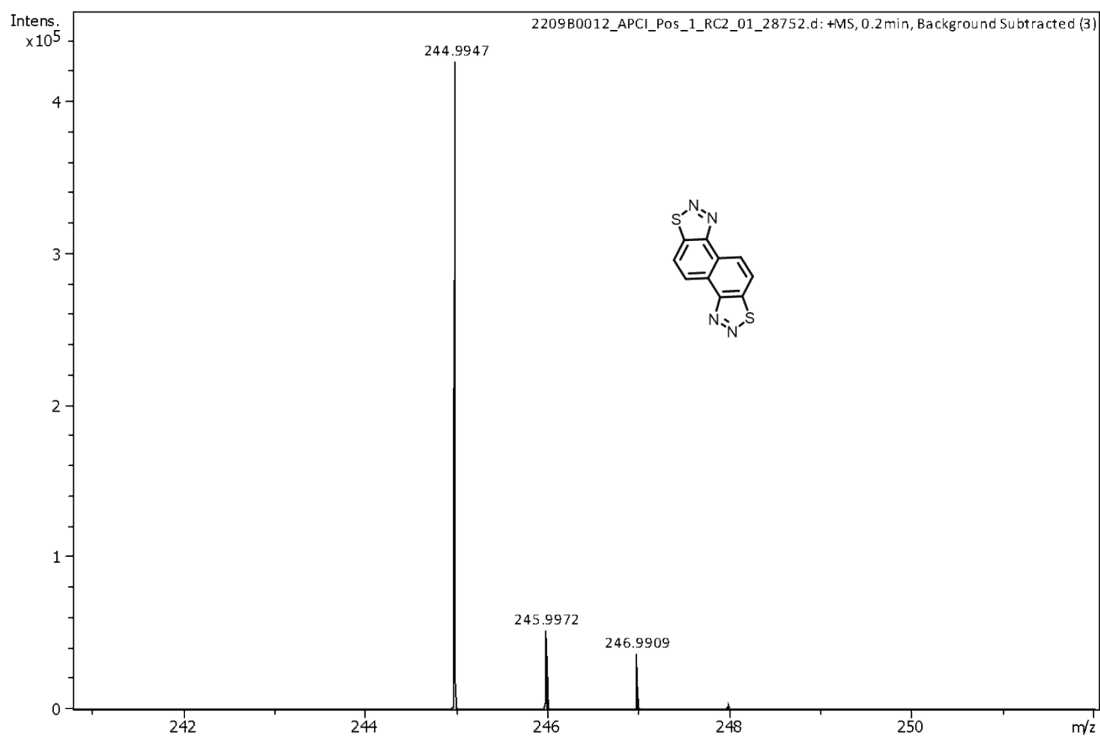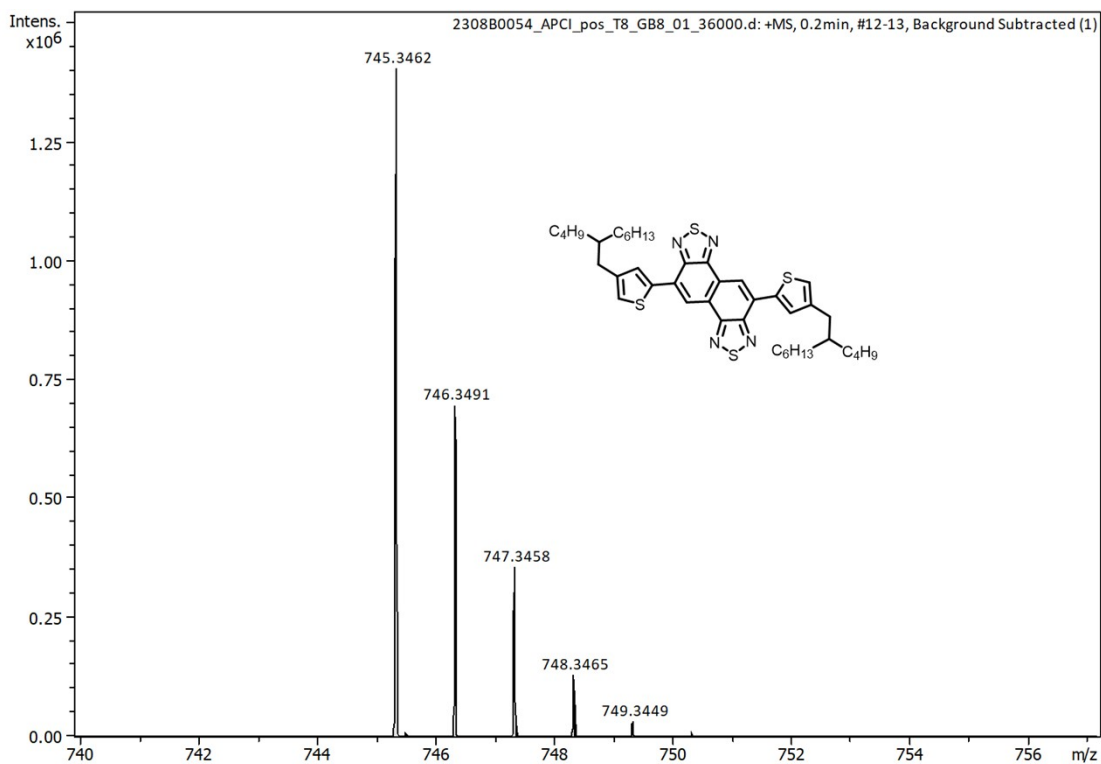
Fig. S50. The mass spectrum of compound **4**.
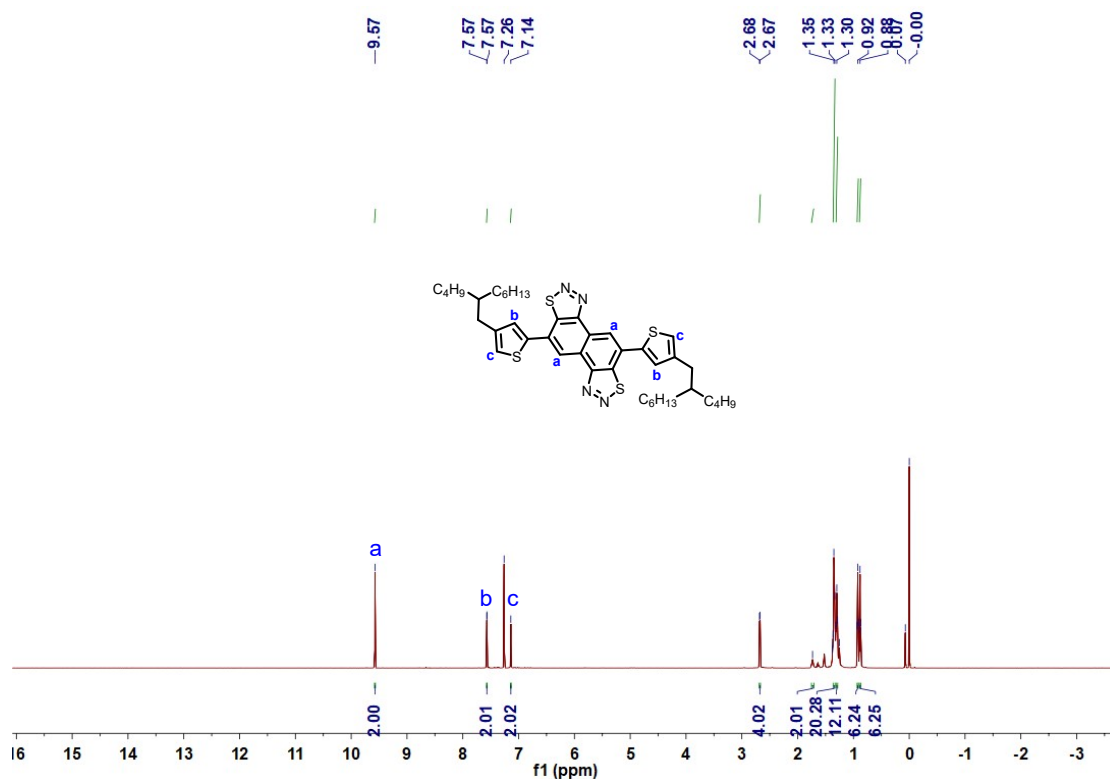
Fig. S51. The ^{1}H NMR spectrum of compound **6** in CDCl$_3$ at room temperature.
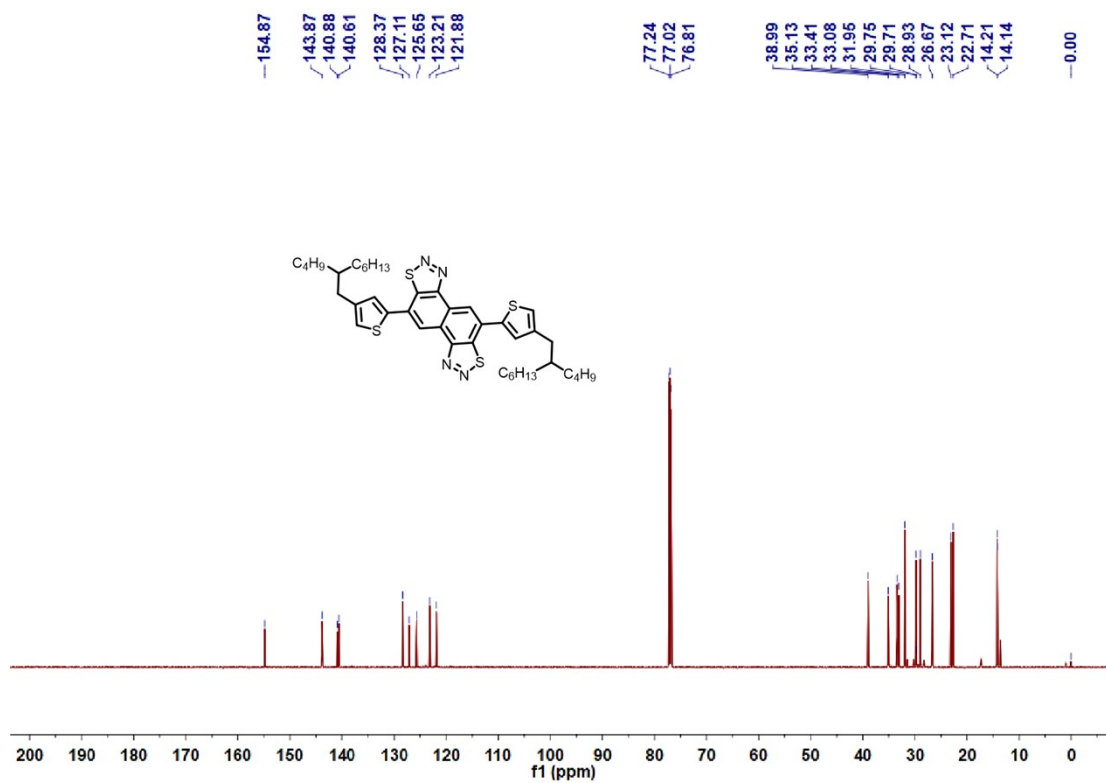
Fig. S52. The ^{13}C NMR spectrum of compound **6** in CDCl$_3$ at room temperature.
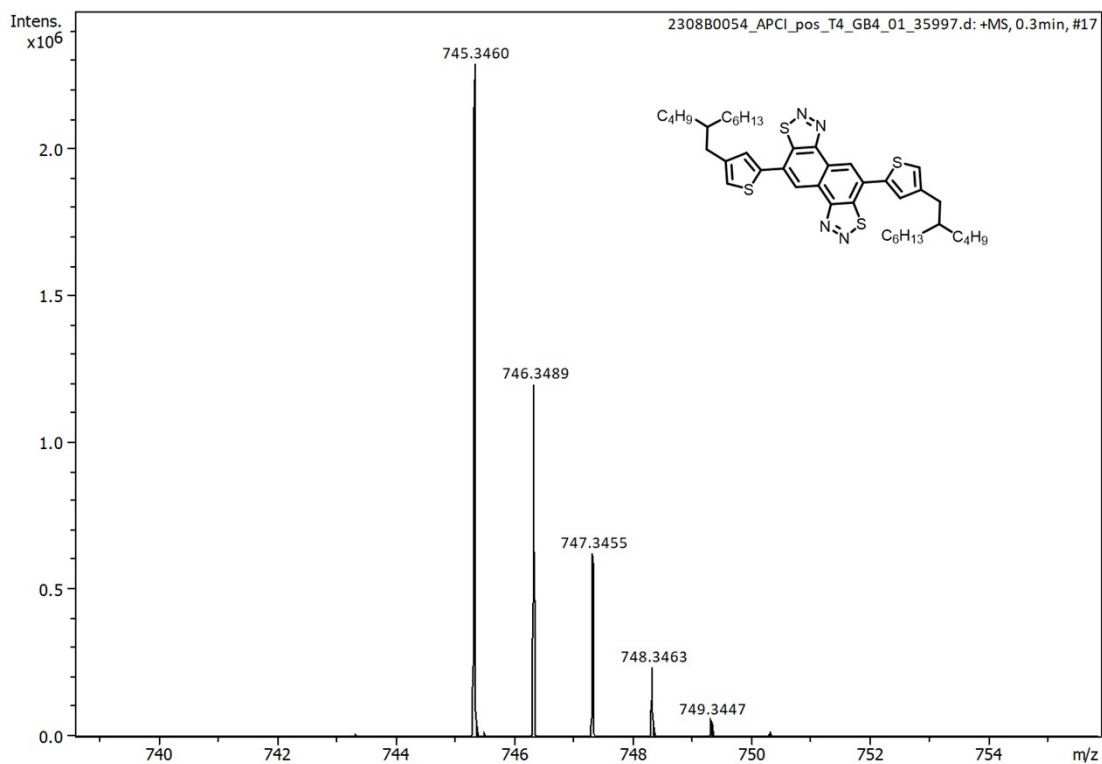
Fig. S53. The mass spectrum of compound **6**.
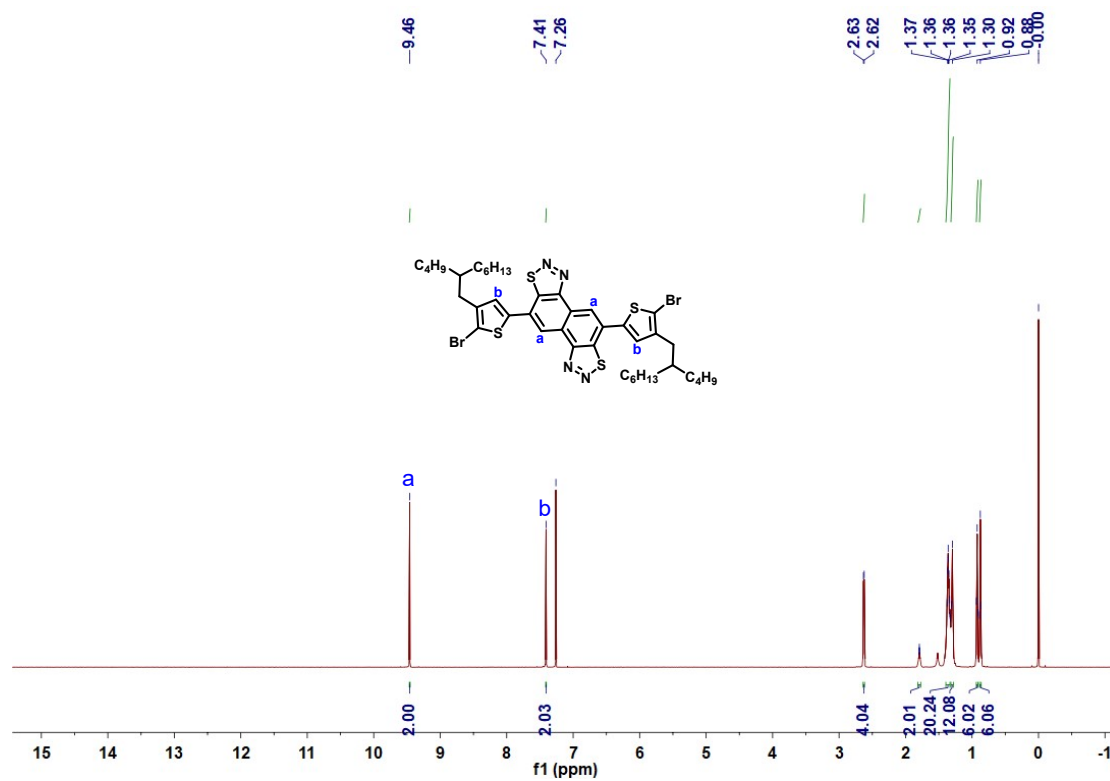
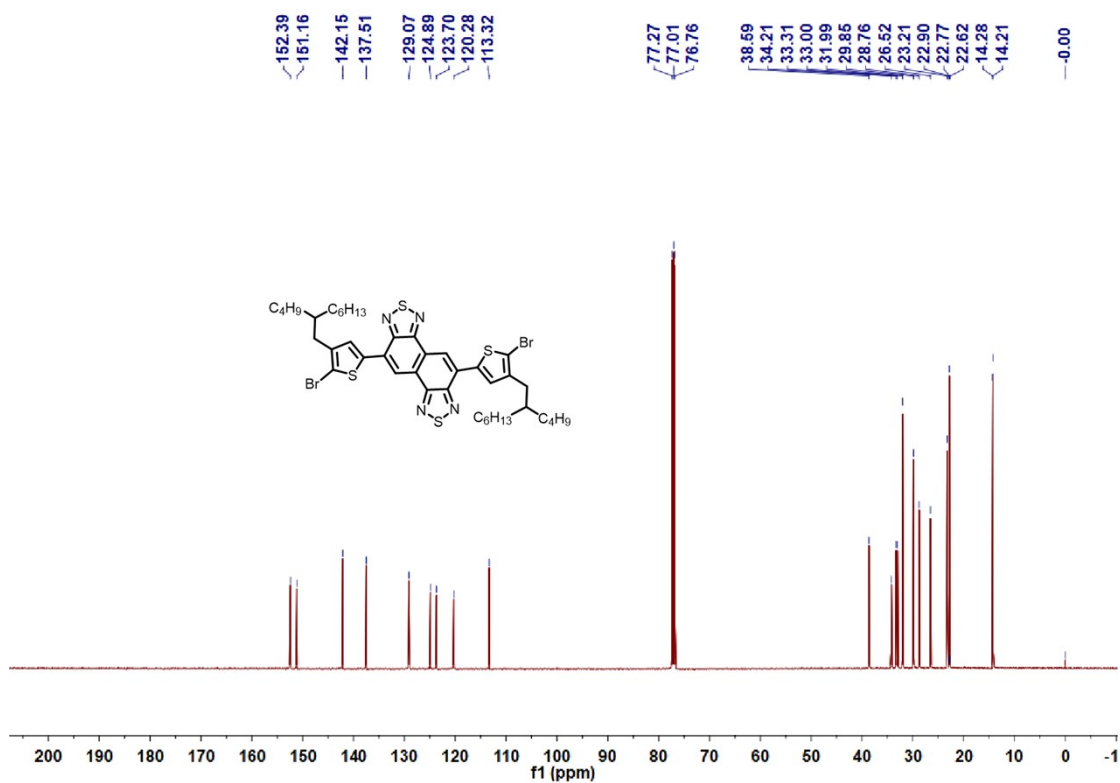**Fig. S54**. The ^1H NMR spectrum of **M1** in CDCl$_3$ at room temperature.
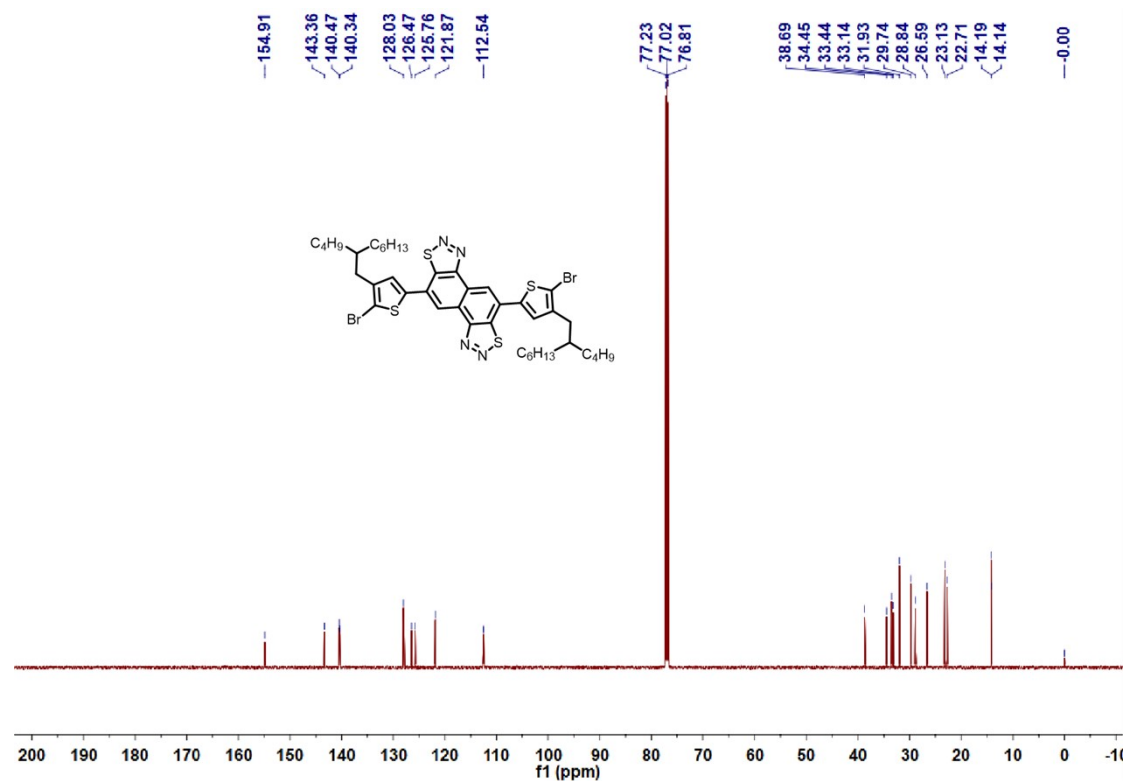
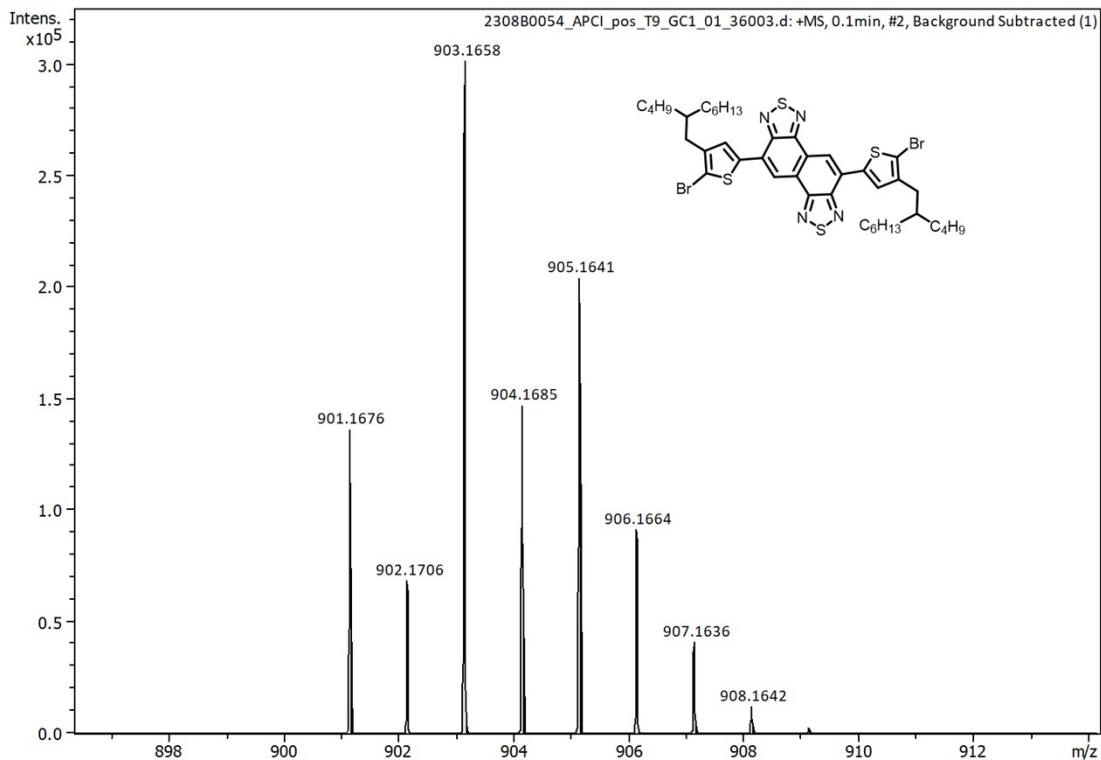**Fig. S55**. The ^{13}C NMR spectrum of **M1** in CDCl$_3$ at room temperature.
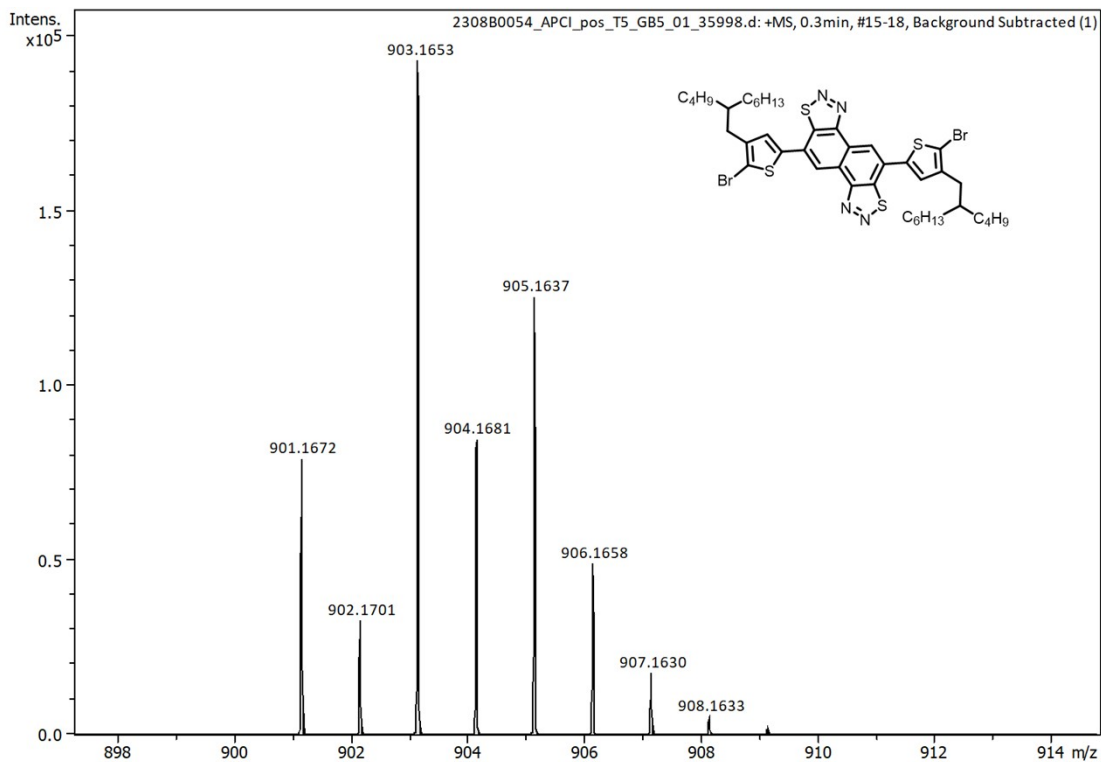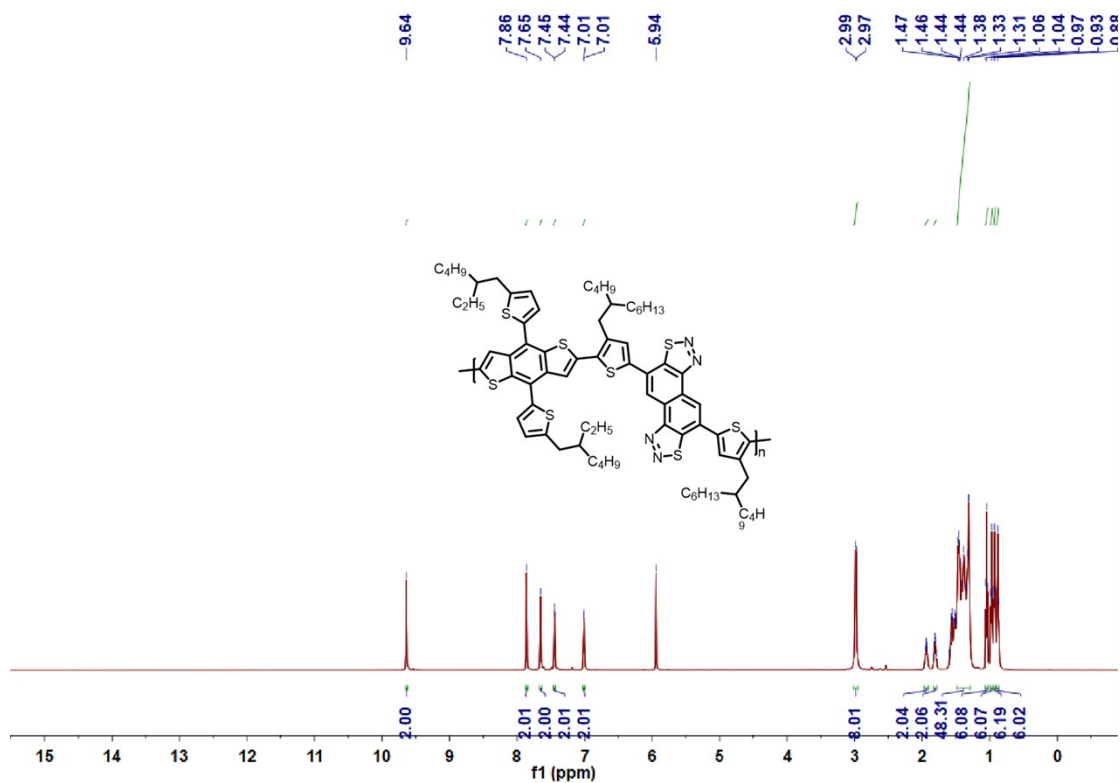
Fig. S56. The mass spectrum of **M1**.
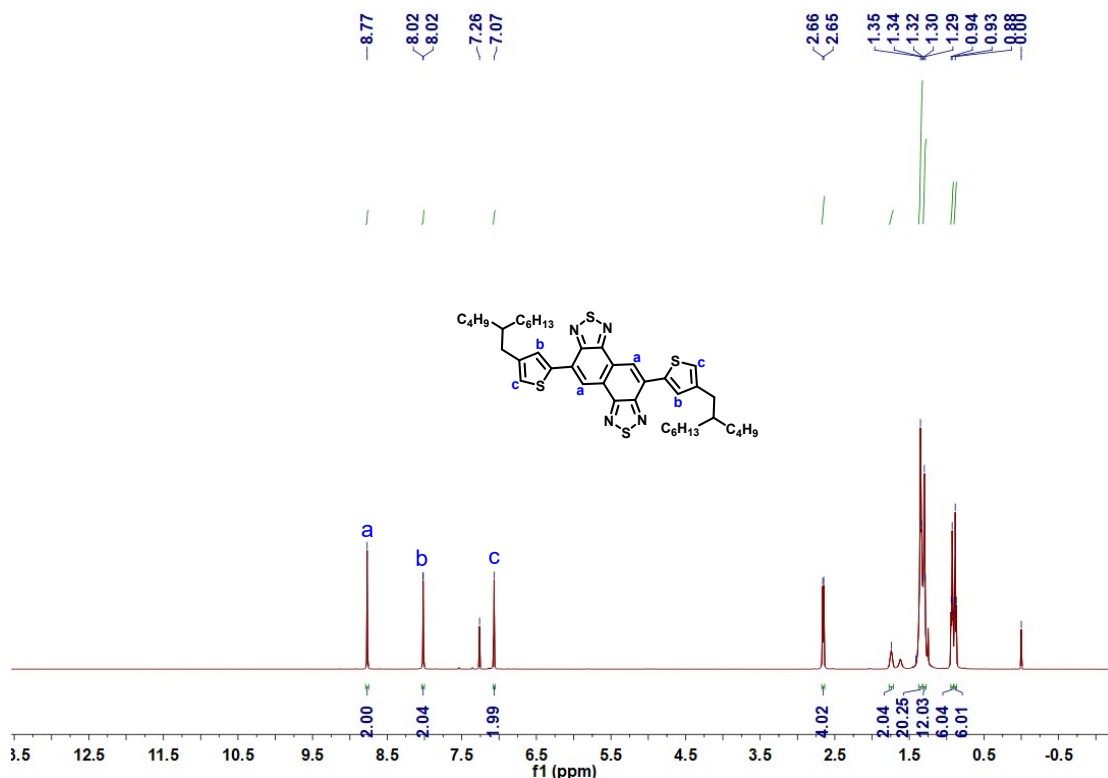
Fig. 57. The ^{1}H NMR spectrum of compound **9** in CDCl$_3$ at room temperature.
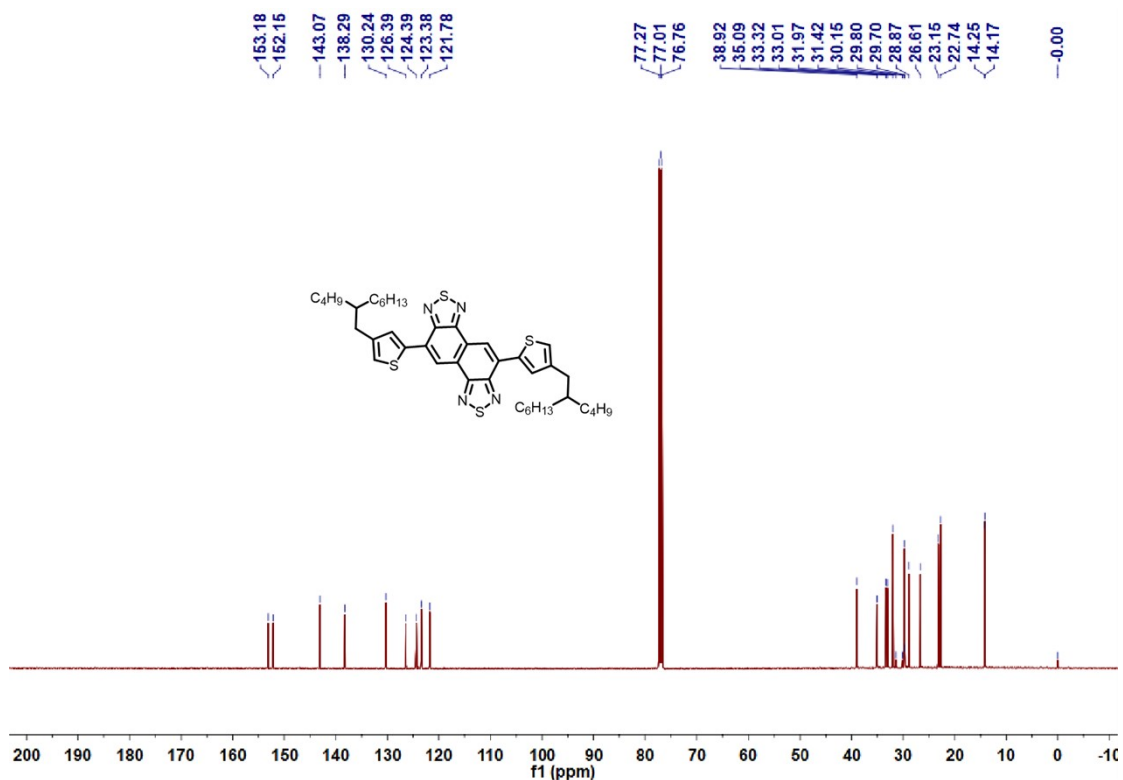
Fig. S58. The ^{13}C NMR spectrum of compound **9** in CDCl$_3$ at room temperature.

Fig. S59. The mass spectrum of compound **9**.
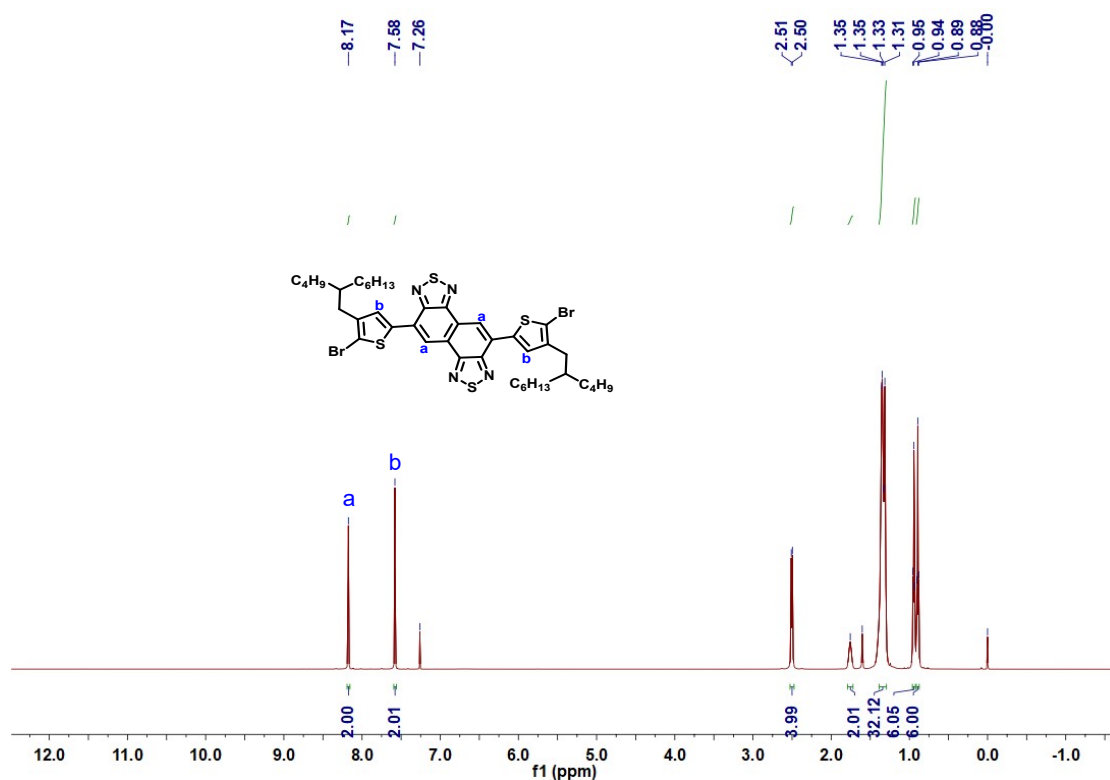
Fig. S60. The ^{1}H NMR spectrum of **M2** in CDCl$_3$ at room temperature.

Fig. S61. The ^{13}C NMR spectrum of **M2** in CDCl$_3$ at room temperature.

Fig. S62. The mass spectrum of **M2**.
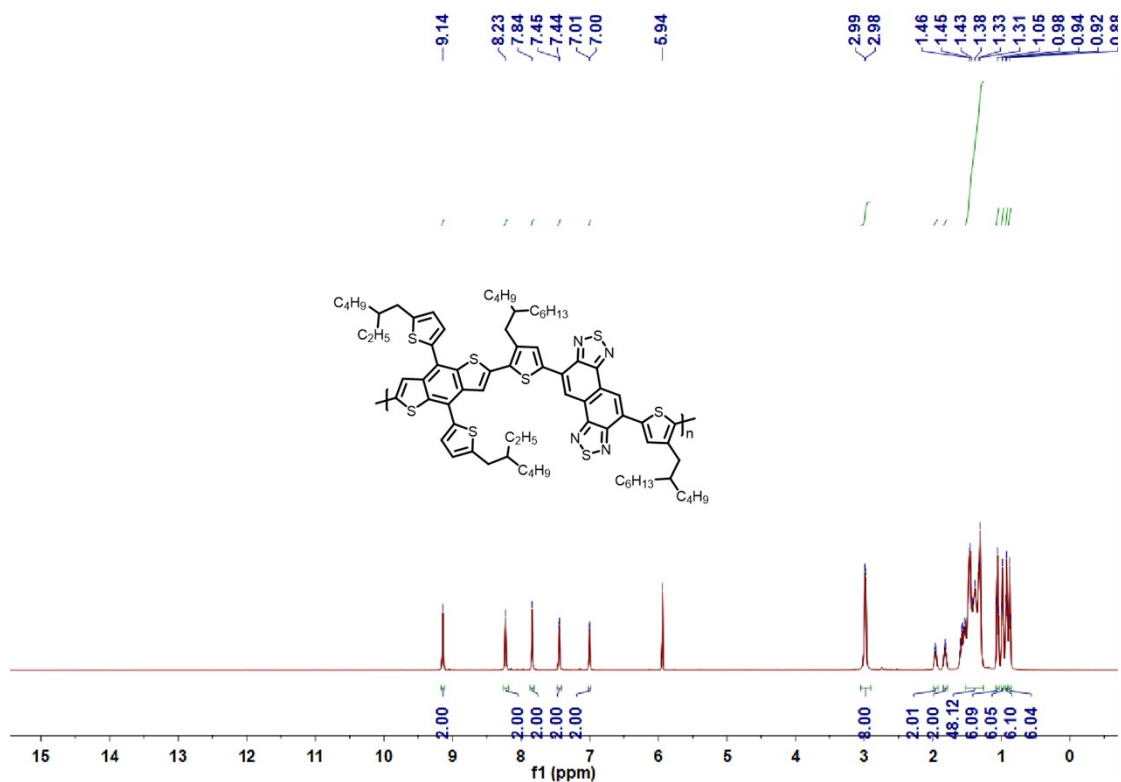

Fig. S63. The ^{1}H NMR spectrum of polymer **PiNT** in $C_2D_2Cl_4$ at 135 ^{o}C.

Fig. S64. The ^{1}H NMR spectrum of polymer **PNT** in $C_2D_2Cl_4$ at 135 ^{o}C.
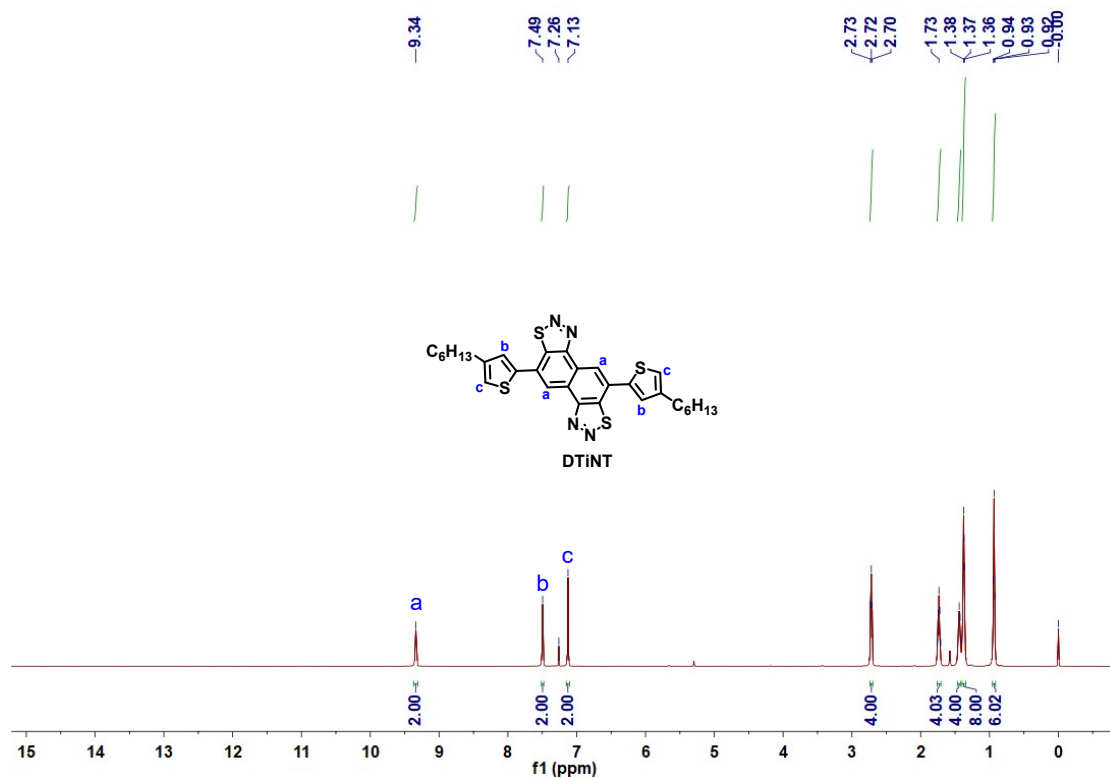
Fig. S65. The ^{1}H NMR spectrum of **DTiNT** in $CDCl_3$ at room temperature.
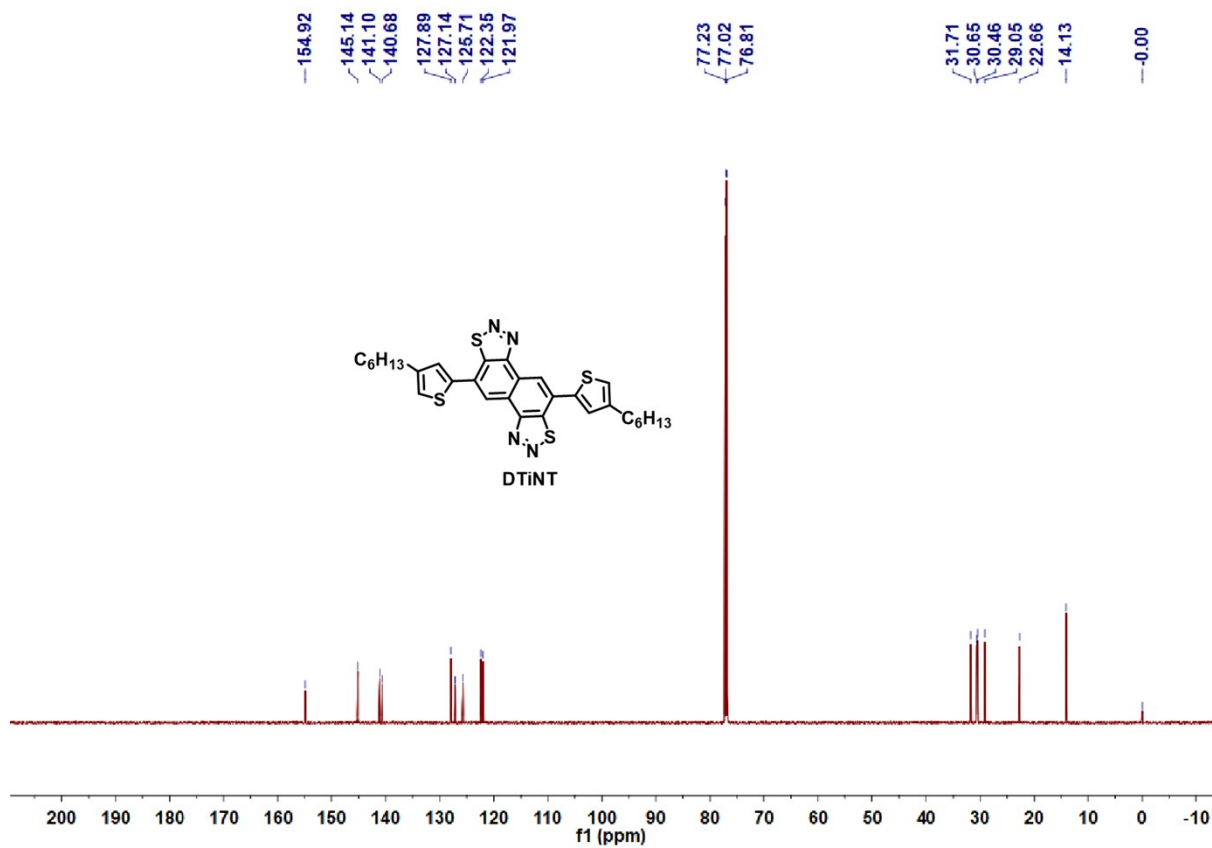
Fig. S66. The ^{13}C NMR spectrum of **DTiNT** in $CDCl_3$ at room temperature.
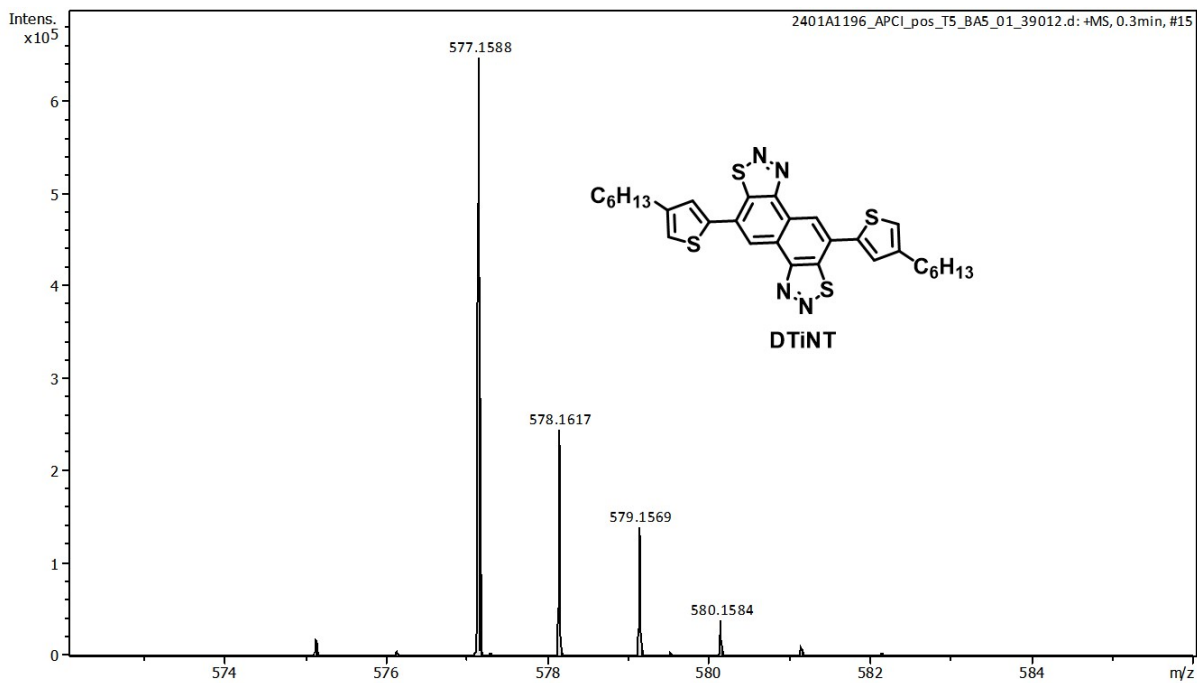

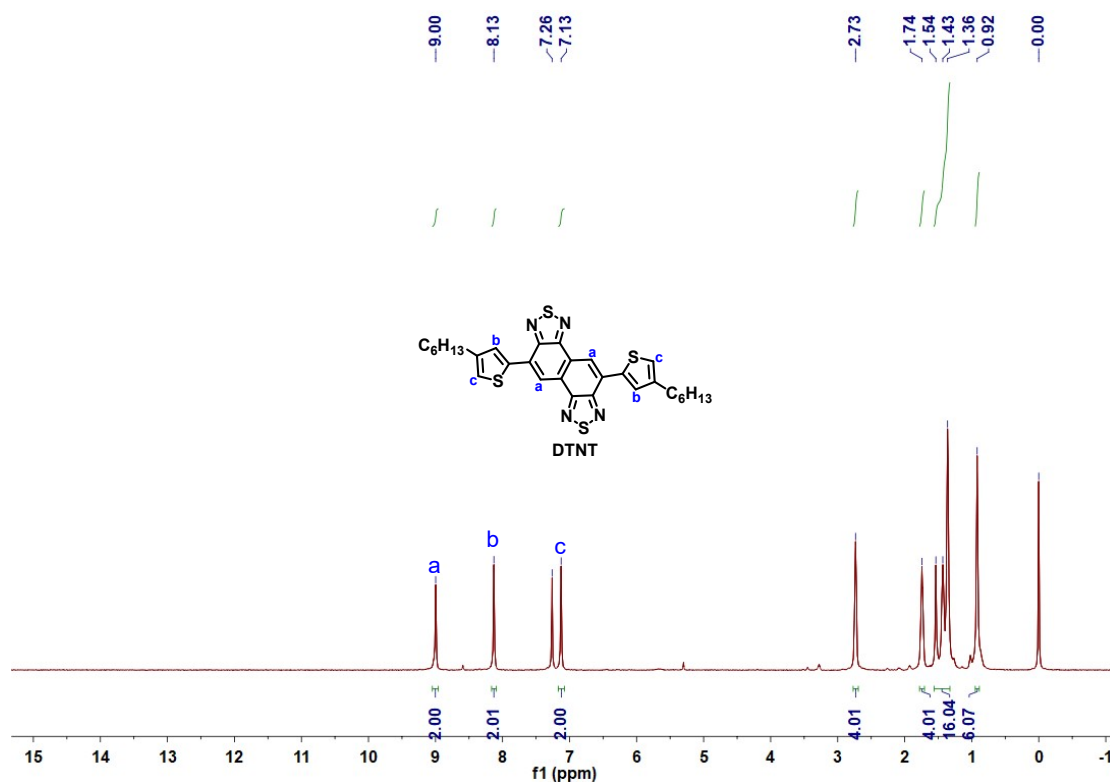**Fig. S67**. The mass spectrum of **DTiNT**.

Fig. S68. The ^1H NMR spectrum of **DTNT** in CDCl$_3$ at room temperature.
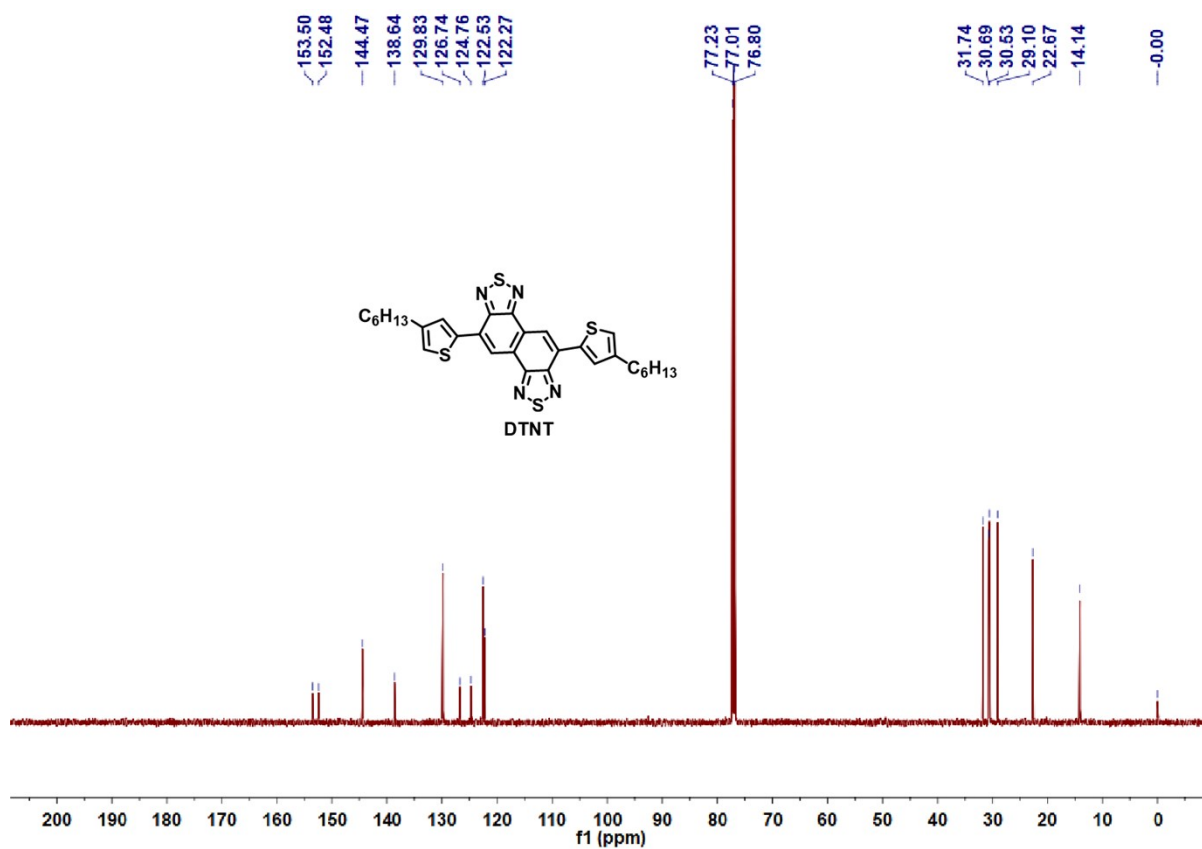

Fig. S69. The ^{13}C NMR spectrum of **DTNT** in CDCl$_3$ at room temperature.
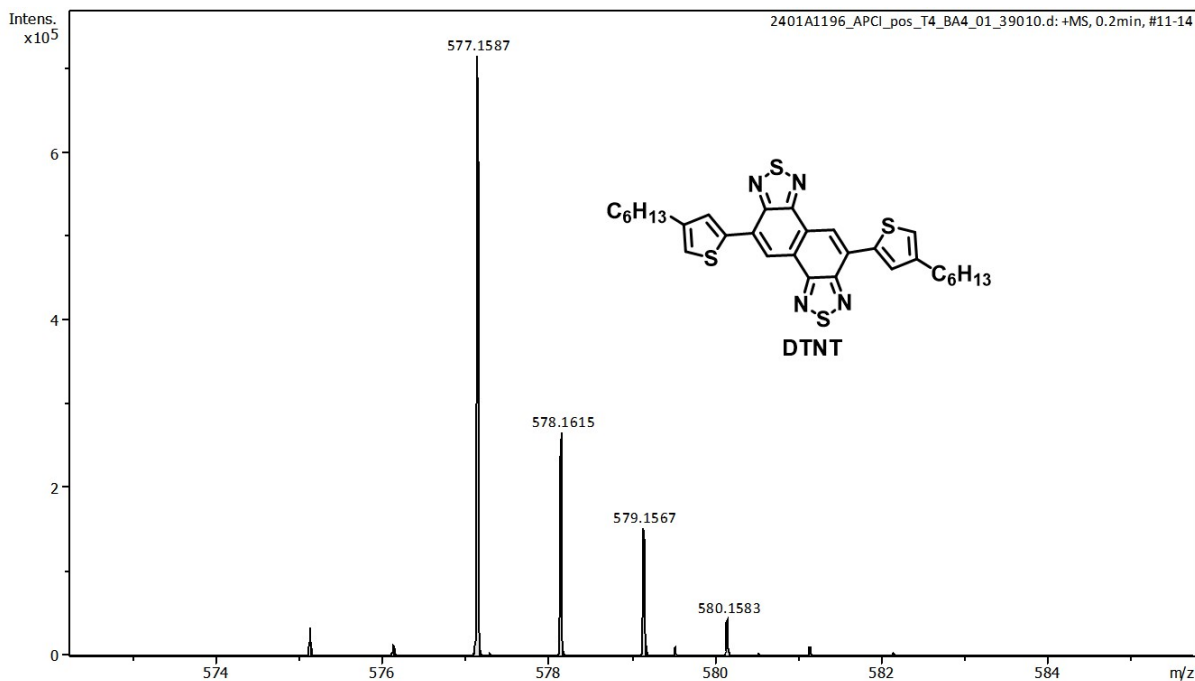
Fig. S70. The mass spectrum of **DTNT**.

17. References

1 T. Lin, Y. Hai, Y. Luo, L. Feng, T. Jia, J. Wu, R. Ma, T. A. Dela Peña, Y. Li, Z. Xing, M. Li, M. Wang, B. Xiao, K. S. Wong, S. Liu, G. Li, *Adv. Mater.,* 2024, **36**, 2312311.

2 Gaussian 16, Revision C.02, M. J. Frisch, G. W. Trucks, H. B. Schlegel, G. E. Scuseria, M. A. Robb, J. R. Cheeseman, G. Scalmani, V. Barone, G. A. Petersson, H. Nakatsuji, X. Li, M. Caricato, A. V. Marenich, J. Bloino, B. G. Janesko, R. Gomperts, B. Mennucci, H. P. Hratchian, J. V. Ortiz, A. F. Izmaylov, J. L. Sonnenberg, D. Williams-Young, F. Ding, F. Lipparini, F. Egidi, J. Goings, B. Peng, A. Petrone, T. Henderson, D. Ranasinghe, V. G. Zakrzewski, J. Gao, N. Rega, G. Zheng, W. Liang, M. Hada, M. Ehara, K. Toyota, R. Fukuda, J. Hasegawa, M. Ishida, T. Nakajima, Y. Honda, O. Kitao, H. Nakai, T. Vreven, K. Throssell, J. A. Montgomery, Jr., J. E. Peralta, F. Ogliaro, M. J. Bearpark, J. J. Heyd, E. N. Brothers, K. N. Kudin, V. N. Staroverov, T. A. Keith, R. Kobayashi, J. Normand, K. Raghavachari, A. P. Rendell, J. C. Burant, S. S. Iyengar, J. Tomasi, M. Cossi, J. M. Millam, M. Klene, C. Adamo, R. Cammi,   J. W. Ochterski, R. L. Martin, K. Morokuma, O. Farkas, J. B. Foresman, and D. J. Fox, Gaussian, Inc., Wallingford CT, 2019. D. J. Fox,

Gaussian 16, Revision C.02, Gaussian, Inc., Wallingford CT, (2019).

3 A. D. Becke, *J.Chem. Phys.,* 1993, **98**, 1372-1377.

4 S. Grimme, J. Antony, S. Ehrlich, H. Krieg, *J. Chem. Phys.,* 2010, **132***, 154104.

5 B. P. Pritchard, D. Altarawy, B. Didier, T. D. Gibson, T. L. Windus, *J. Chem. Inf. Model.,* 2019, **59**, 4814-4820.

6 T. Lu, F. Chen, *J. Comput. Chem.,* 2012, **33**, 580-592.

7 W. Humphrey, A. Dalke, K. Schulten, *J. Mol. Graph.,* 1996, **14**, 33-38.

8 L. Belpassi, I. Infante, F. Tarantelli, L. Visscher, *J. Am. Chem. Soc.,* 2008, **130**, 1048-1060.

9 A. D. Becke, K. E. Edgecombe, *J. Chem. Phys.,* 1990, **92**, 5397-5403.

10 B. Silvi, A. Savin,. *Nature* 1994, **371**, 683-686.

11 Y.-L. Wang, X.-B. Wang, X.-P. Xing, F. Wei, J. Li, L.-S. Wang, *J. Phys. Chem. A* 2010, 114 , 11244-11251.

12 A. J. Bridgeman, G. Cavigliasso, L. R. Ireland, J. Rothery, *J. Chem. Soc., Dalton Trans.,* 2001, **14**, 2095-2108.

13 Pauling, L. The Nature of the Chemical Bond (Cornell Univ. Press, 1960).

14 P. Bi, F. Zheng, X. Yang, M. Niu, L. Feng, W. Qin, X. Hao, *J. Mater. Chem. A* 2017, **5**, 12120-12130.

15 W. S. Jeon, T. J. Park, S. Y. Kim, R. Pode, J. Jang, J. H. Kwon, *Org. Electron.,* 2009, **10**, 240-246.